CEBAF Program Advisory Committee Six (PAC6) Proposal Cover Sheet

This proposal must be received by close of business on April 5, 1993 at:

CEBAF
User Liaison Office
12000 Jefferson Avenue
Newport News, VA 23606

Proposal Title

The Electric Form Factor of the Neutron
From the $d(\vec{e}, e'\vec{n})p$ Reaction

Contact Person

Name: R. Madey
Institution: Kent State University/Hampton University
Address: Physics Department
Address:
City, State ZIP/Country: Kent, Ohio 44242-0001 / Hampton, VA 23668
Phone: (216)-672-2596 / (804)-727-5277 **FAX:** (216)-672-2959 / (804)-727-5188
E-Mail → BITnet: **Internet:** IN%"MADEY@KSUVXA.KENT.EDU"
IN%"MADEY@CEBAF.GOV"

If this proposal is based on a previously submitted proposal or letter-of-intent, give the number, title and date:

PR-89-005 - The Electric Form Factor of the Neutron
From the $d(\vec{e}, e'\vec{n})p$ Reaction 10/30/89

CEBAF Use Only

Receipt Date: 4/5/93 Log Number Assigned: PR 93-038

By: SP

April 1, 1993

Revision of Proposal for CEBAF E89-05

THE ELECTRIC FORM FACTOR OF THE NEUTRON FROM THE $d(\vec{e}, e'\vec{n})p$ REACTION

SCIENTIFIC PARTICIPANTS

Kent State Universtity
Kent, OH 44242
R. Madey (Spokesman)
B. Anderson
A. Baldwin
T. Eden
D. Keane
A. Lai
D. Manley
J. Watson
W. Zhang
Graduate Student(s)

CEBAF
Newport News, VA 23606
R. Carlini
D. Mack
J. Mitchell
P. Ulmer
R. Whitney
S. Wood
C. Yan

Hampton Universtity
Hampton, VA 23668
K. Baker
S. Beedoe
K. Beard
L. Tang
Graduate Student(s)

M.I.T.
Cambridge, MA 02139
W. Bertozzi
G. Dodson
M. Farkhondeh
W. Korsch
S. Kowalski
Graduate Student(s)

College of William and Mary
Williamsburg, VA 23185
M. Finn

Gettysburg College
Gettysburg, PA 17325
P. Pella

American University
Washington, DC 20016
B. Flanders

Duke University
Durham, NC 27707
C. Howell
W. Ternow
R. Walter
Graduate Student(s)

University of Virginia
Charlottesville, VA 22901
R. Lourie

I.U.C.F.
Bloomington, IN
J. Cameron

Old Dominion University
Norfolk, VA 23508
L. Weinstein

University of Maryland
College Park, MD 20742
C. Chang
J. Kelly
P. Markowitz

[This document was prepared by R. Madey, A. Lai, T. Eden, and W-M. Zhang of Kent State University.]

ABSTRACT

We propose to determine the electric form factor G_E^n of the neutron by scattering longitudinally-polarized electrons from deuterium quasielastically and measuring the transverse polarization component $P_{S'}$ of the recoil neutron. The neutron polarization component $P_{S'}$, which lies in the scattering plane and normal to the neutron momentum, is directly proportional to G_E^n in the impulse approximation. The neutron is detected in coincidence with the scattered electron. The experiment utilizes a neutron polarimeter provided by Kent State University and a liquid-deuterium (LD_2) target provided by CEBAF. The neutron polarimeter operated successfully with a duty cycle of about 0.8% at Bates with a luminosity of $3 \times 10^{36} \mathrm{cm}^{-2}\mathrm{s}^{-1}$; at CEBAF with a duty cycle of unity, the neutron polarimeter is expected to operate satisfactorily with a luminosity of 3.8×10^{38} $\mathrm{cm}^{-2}\mathrm{s}^{-1}$.

The uncertainties in the best available measurements of G_E^n as a function of Q^2 are too large to distinguish between form factor models, and they can not even distinguish between $G_E^n = 0$ and the dipole parameterization ($G_E^n = -\tau G_M^n$) when the Dirac form factor $F_{1n} = 0$; however, we propose to measure the neutron polarization $P_{S'}$ at $Q^2 = 0.30$, 0.50, 1.0, 1.5, and 2.0 $(\mathrm{GeV/c})^2$ with uncertainties that will distinguish between different parameterizations such as the dipole parameterization ($G_E^n = -\tau G_M^n$), the Galster parameterization $[G_E^n = -\tau G_M^n (1 + 5.6\tau)^{-1}]$, and $G_E^n = 0$,

A theoretical study by Arenhövel (1987) indicates that the transverse polarization component of the recoil neutron has almost no dependence on the deuteron model, and is insensitive to the influence of final-state interactions, meson-exchange currents, and isobar configurations.

SUMMARY

This proposal presents details of a design for the experiment CEBAF E89-05, which is aimed at determining the neutron electric form factor G_E^n. The measurement technique uses a neutron polarimeter to meaure transverse polarization $P_{S'}$ of the recoiling neutron from the reaction $d(\vec{e}, e'\vec{n})p$ in coincidence with the scattered electron. A schematic view of the experimental arrangement is shown in Fig. 6. We want to do this experiment for the following reasons: *ONE*, accurate measurements of G_E^n provide fundamental information about both nucleon and nuclear structure; *TWO*, previous measurements of G_E^n are far from satisfactory, as shown in Figs. 2 through 4 in the proposal, because of large uncertainties and model-dependent features with most experiments, which failed to distinguish between different G_E^n parameterizations; and *THREE*, the technique proposed for this experiment will give model-insensitive measurement of G_E^n with uncertainties that permit distinguishing between different parameterizations of G_E^n. This technique, suggested in 1981,[14] was found later to be insensitive to the influence of final-state-interactions, meson-exchange currents, and isobar configurations.[5,9,10,11]

By measuring the transverse polarization $P_{S'}$, the ratio $g \equiv G_E^n/G_M^n$ can be extracted from Eq. (9) in Section 2 of the proposal, and thus $G_E^n = g\, G_M^n$ can also be extracted because the magnetic form factor G_M^n of the neutron has been measured satisfactorily or can be measured (model-insensitively) again for our kinematics (see our proposal for CEBAF E89-05 Extension). For this experiment, the uncertainties in g can be calculated from Eq. (16) in Section 4.1, which propagates into the total uncertainty in G_E^n as shown in Eq. (74) in Section 4.13.

The key experimetal apparatus employed in this experiment will be the high momentum spectrometer (HMS) of Hall C and a neutron polarimeter provided by Kent State University. We choose the HMS because its horizontal angular acceptance in the reversed-quad mode is the largest available at CEBAF. Details of the neutron polarimeter and its shielding enclosure are given in Section 3 of the proposal and shown in Figs. 7, 8A, and 8B

This experiment is optimized in terms of finding the maximum figure-of-merit (FOM), defined in Eq. (33) in Section 4.4, which is equivalent to finding the minimum data acquisition time for a desired relative statistical uncertainty. This FOM associated with a triple-differential cross section averaged over the detector acceptances differs from the conventional FOM associated with a "point" (unaveraged) triple-differential cross section. We found that the FOM has a maximum at a relatively large electron scattering angle [see, for example, Fig. 22 for $Q^2 = 1.0$ $(\mathrm{GeV/c})^2$] for all the Q^2 points proposed for this experiment, and thus the experiment is designed to be carried out at these relatively large electron scattering angles as given in Table II(c) of the proposal. We present in Section 4.11 the reasons for the difference between the FOM as defined in Eq. (33) and the FOM defined in terms of the "point" cross section. The latter definition favors small electron scattering angles [as shown also in Fig. 22].

The values of the averaged triple-differential cross section are calculated from MCEEP[17] and presented in Table IX in the proposal. The angular acceptances in both neutron and electron arms are determined partially by considerations of the neutron energy resolution (described in Section 4.6) and the background reduction (described in Section 5); the final choice of the angular acceptances is $\Delta\theta_n = \pm 3.00°$, $\Delta\theta_e = \pm 3.40°$, $\Delta\phi_n^{\mathrm{v}} = \pm 0.0750°$. Careful attention has been given to the angular matching of both arms as described in Section 4.8. These studies justify the angular acceptances given above, and the vertical angular acceptance $\Delta\phi_e^{\mathrm{v}}$ of the electron arm is matched kinematically with $\Delta\phi_n^{\mathrm{v}}$ of the neutron arm. With these angular acceptances and the values of the averaged triple-differential cross sections from MCEEP, we estimated the real counting rates from Eq. (56) in Section 4.10 of the proposal. Also, as described in Section 4.12, we calculated the accidental counting rates from Eq. (69) by scaling the observed accidental counting rates in our earlier experiment at Bates. The reals and the accidental counting rates are listed in Table X of the proposal for a luminosity of 3.2×10^{38} $\mathrm{cm}^{-2}\mathrm{s}^{-1}$. With these counting rates and data acquisition times chosen as described in Section 6 and shown in Figs. 38 through 42, the relative statistical uncertainties

in G_E^n are calculated and given in Table X with values of $\Delta G_E^n/G_E^n$ ranging from $\lesssim$ 10% [at Q^2 = 0.3 (GeV/c)^2] to $\lesssim \pm$30% [at Q^2 = 2.0 (GeV/c)^2] depending on the actual values of G_E^n. The projected statistical uncertainties are shown in Fig. 29 for the dipole, Galster, and $G_E^n = 0$ parameterizations. As shown, these uncertainties make it possible to distinguish between different parameterizations of G_E^n; the numerical values of these projected results are listed in Tables XVI, XVII, and XVIII. Also we estimated the uncertainties in G_E^n for parameterizations other than the three cases studied in detail (viz., dipole, Galster, and $G_E^n = 0$); as shown in Fig. 30, the uncertainties will be in between those of the three cases.

We studied backgrounds with the CEBAF Large Acceptance Spetrometer Event Generator (CELEG).[21] These studies show that the inclusive background neutrons from inelastic scattering can be reduced substantially by proper choice of the neutron angular acceptance. We show these results in Figs. 31 through 36. Also, we studied possible backgrounds from pion production processes and found that the experiment will be free from these backgrounds as shown in Fig. 37.

We propose initially to carry out a measurement of G_E^n at Q^2 = 1.0 (GeV/c)^2, and then to make measurements at other Q^2 points in separately scheduled runs. The data acquisition times with a liquid-deuterium target are 150, 250, 500, 500, and 800 hours at Q^2 = 0.30, 0.50, 1.0, 1.5, and 2.0 (GeV/c)^2. The two measurements at Q^2 = 0.30 and 0.50 (GeV/c)^2 may be carried out at the Bates Linear Accelerator Center.

Finally, we provide two appendices. Appendix A deals with the important issue of model-insensitivity of this experiment based on Arenhövel's calculations made explicitly for the Q^2 values proposed for this experiment. The figures and tables presented in Appendix A indicate that our choice of the angular acceptances will preserve the model-insensitivity of this experiment. Appendix B deals with another important issue of neutron polarimeter calibrations, which describes how the analyzing power and the efficiency of the neutron polarimeter was measured for Bates E85-05.

TABLE OF CONTENTS

LIST OF TABLES

LIST OF FIGURES

CEBAF E89-05

The Electric Form Factor of the Neutron from the d($\vec{e}, e'\vec{n}$)p Reaction

1. Scientific Background and Motivation

The electric form factor G_E^n of the neutron is a fundamental quantity needed for the understanding of both nucleon and nuclear structure. The dependence of G_E^n on Q^2, the four-momentum-transfer-squared, is determined by the charge distribution of the neutron. At $Q^2 = 0$, the slope of G_E^n is known to 2% accuracy by scattering neutrons from atomic electrons[1] . At $Q^2 > 0$ the electric form factor G_E^n is small and poorly known. Present models of the neutron predict different values of G_E^n at high momentum transfer; accordingly, good determinations of G_E^n will provide an important test of these models. Also the influence of G_E^n is not negligible in the interpretation of electron scattering from nuclei at high momentum transfer. For these reasons, it is of paramount importance to obtain reliable determinations of G_E^n with smaller uncertainties than before.

At high values of Q^2, the values of G_E^n according to some models are comparable or larger than the values of G_E^p, the electric form factor of the proton; for example, for the dipole parameterization of G_E^n and G_E^p, shown in Fig. 1 as a function of Q^2, the magnitudes of G_E^p and G_E^n are comparable in the Q^2 region of above about 1 $(\mathrm{GeV/c})^2$, which is accessible at CEBAF. Because the isovector form factors of nuclei are essentially proportional to the difference $G_E^p - G_E^n$ (and the isoscalar form factors are essentially proportional to the sum $G_E^p + G_E^n$), the value of G_E^n is needed for the understanding of electron scattering experiments that probe atomic nuclei at high momentum transfer.

Our present knowledge of the electric and magnetic form factors G_E and G_M for protons and neutrons was obtained from measurements of the angular dependence of the cross section by elastic electron–proton scattering and quasielastic electron–deuteron scattering. Previous experiments contain large systematic errors because of uncertainties in the theoretical description of the deuteron, mostly from final-state interactions (FSI) and meson-exchange currents (MEC). Based on a recent

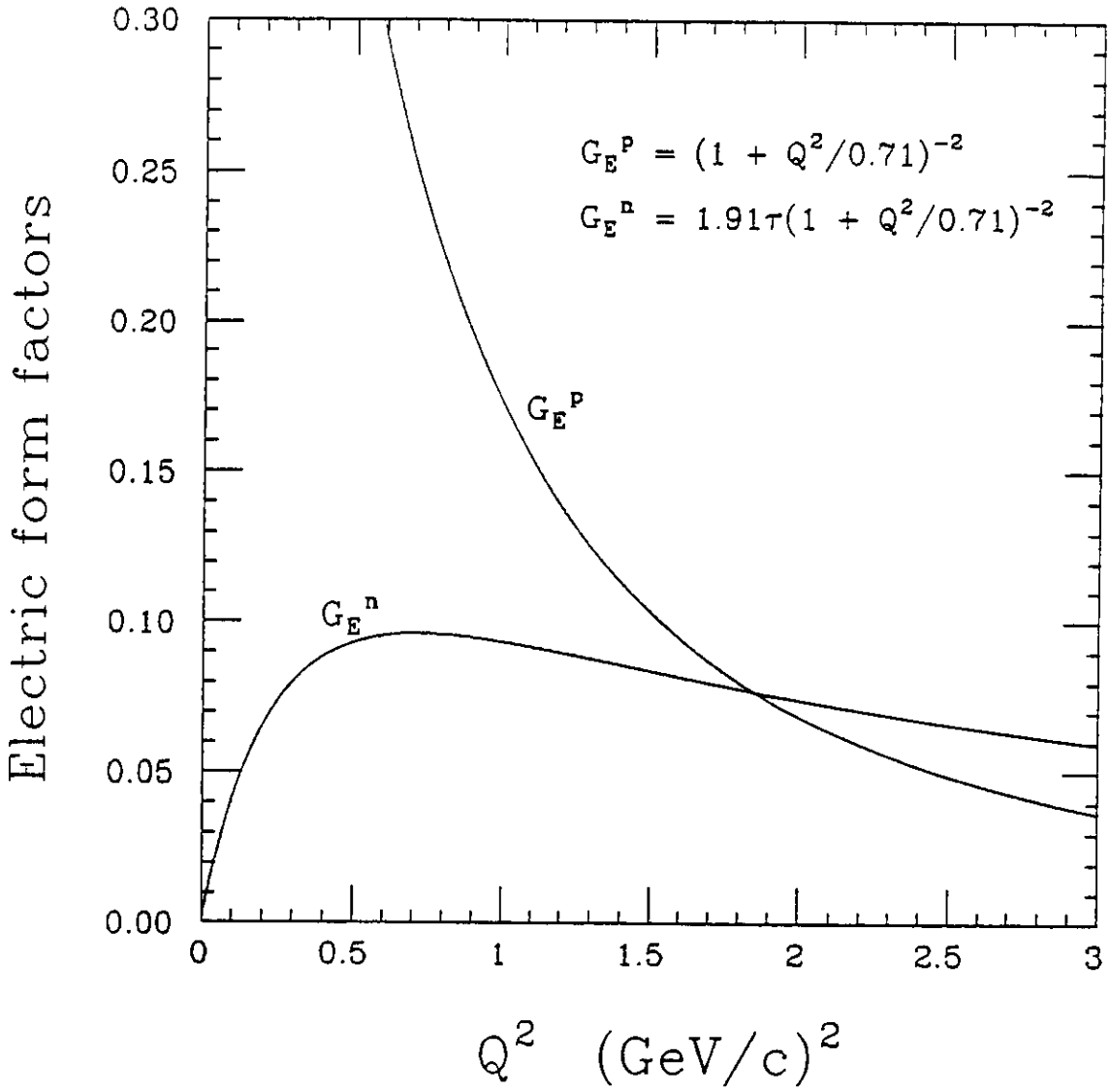

Fig. 1 Proton and Neutron Electric Form Factors as a Function of Q^2, the Four-Momentum-Transfer-Squared.

measurement of quasielastic electron-deuteron scattering at Saclay, Platchkov *et al.*[2] inferred G_E^n up to $Q^2 = 0.78$ (GeV/c)^2 by unfolding the Paris potential: however, unfolding with other potentials yields different form factors. The results of Platchkov *et al.* for $G_E^n(Q^2)$ vs Q^2 by unfolding the Paris potential are shown in Fig. 2; their deduced results for G_E^n by unfolding with four potentials are shown in Fig. 3. The uncertainties or model dependencies are too large to distinguish between different models. Lung *el al.*[3] reported new measurements from SLAC-NE11 of quasielastic *e-d* cross sections at forward and backward angles, which permit Rosenbluth separations of G_E^n and G_M^n at $Q^2 = 1.75$, 2.50, 3.25 and 4.00 (GeV/c)^2. Although Lung *et al.*[3] stated that their G_E^n data from SLAC-NE11 were consistent with $(G_E^n)^2 = 0$ for $1.75 \leq Q^2$ (GeV/c)$^2 \leq 4.00$, the correct Q^2-dependence of G_E^n remains in doubt; for example, our preliminary result from Bates E85-05[4] in combination with the data of Lung *et al.*[3] favors the Galster type of parameterization of G_E^n, and the fit shown in Fig. 4 to the combined data excludes $G_E^n = 0$ at a confidence level of 95%.

Arenhövel[5] calculated the effect of the electric form factor of the neutron G_E^n on the polarization transfer in the $d(\vec{e}, e'\vec{n})p$ reaction in the quasifree region, where the deuteron serves as a neutron target while the proton acts mainly as a spectator. Using a nonrelativistic theory and a realistic nucleon-nucleon potential, Arenhövel found that the sideways polarization of the recoil neutron $P_{S'}$, which vanishes for coplanar kinematics and unpolarized electrons, is most sensitive to G_E^n for neutron emission in the quasifree case. Using the parameterization of Galster *et al.*[6] for G_E^n, Arenhövel's calculation indicates that even away from the forward-emission direction (with respect to the direction of the momentum transfer $\vec{q}$), the increase in the sideways polarization of the neutron $P_{S'}$ prevails up to a neutron angle of nearly 30° measured with respect to $\vec{q}^{\,c.m.}$ in the center-of-mass system. In the forward direction with respect to $\vec{q}^{\,c.m.}$, Arenhövel found also that the neutron polarization $P_{S'}$ is insensitive to the influence of final-state interactions, meson-exchange currents, and isobar configurations, and that this lack of sensitivity holds again up to an angle of nearly 20° away from the forward direction with respect

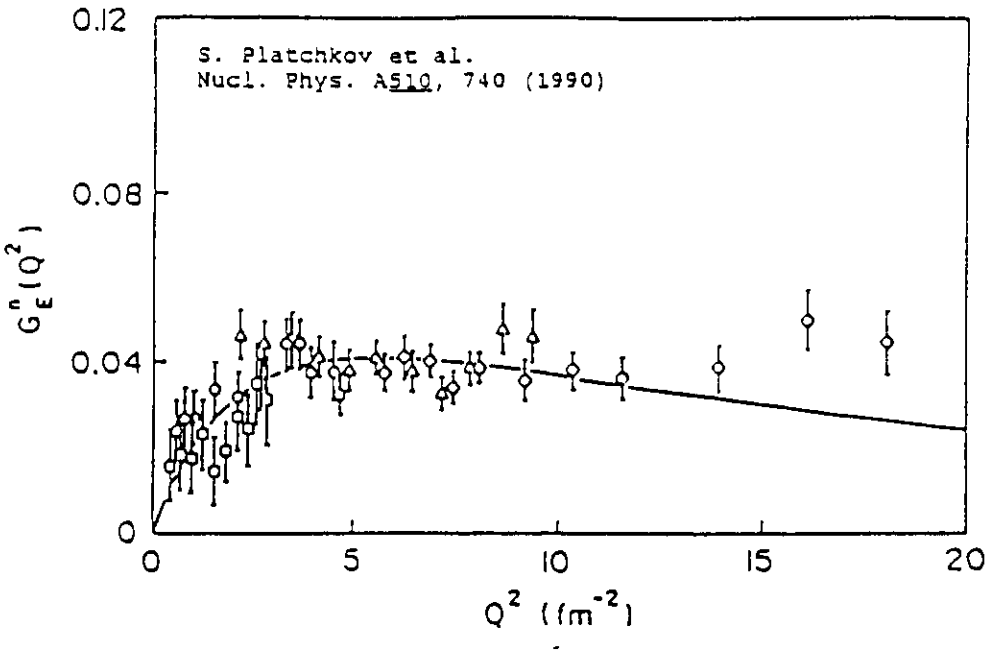

Fig. 2 $G_E^n(Q^2)$ vs Q^2 by unfolding the paris potential.

S. Platchkov et al. / The deuteron $A(Q^2)$ structure function

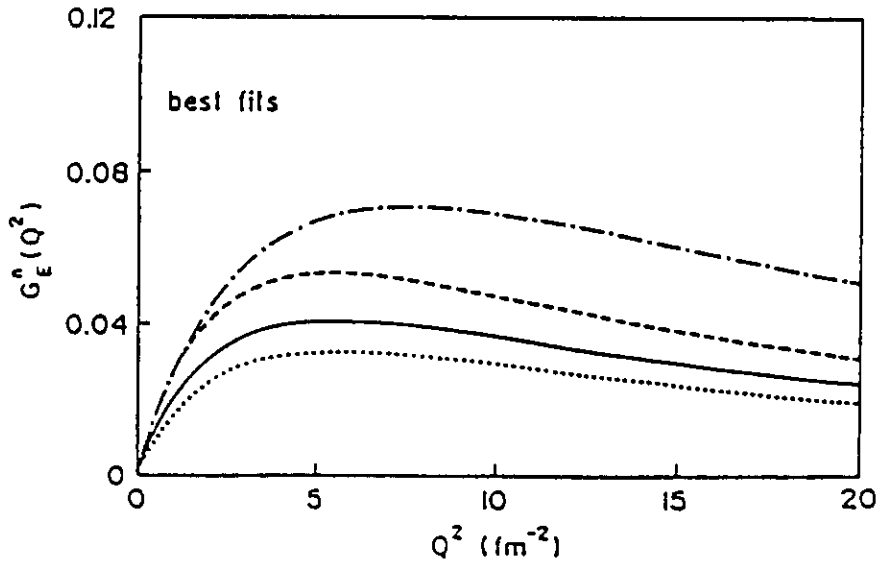

Fig. 3 Two-Parameter Fits to Data for G_E^n Deduced from $A(Q^2)$ by Unfolding the Paris (solid), RSC (dotted), Argonne V14 (dashed) or Nijmegen (dash-dotted) Potentials. For clarity, the corresponding sets of data points are not shown.

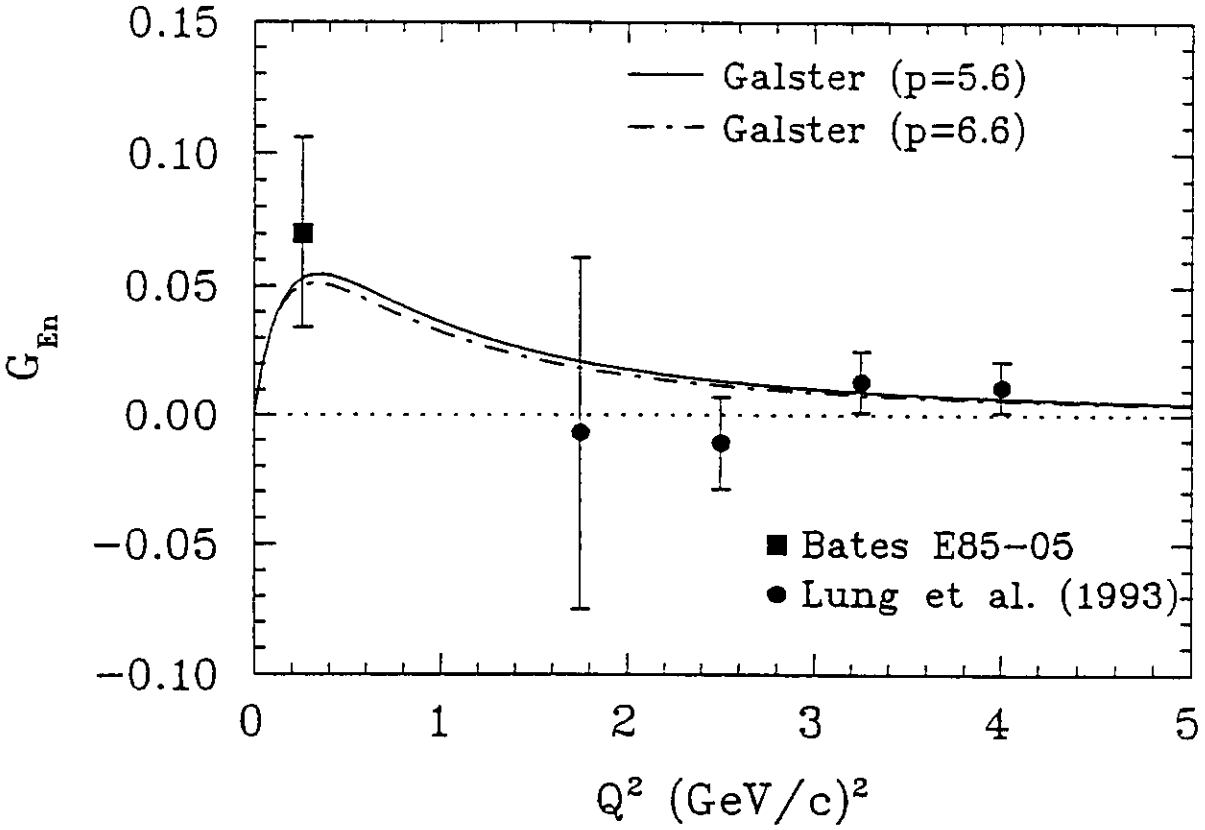

Fig. 4 G_E^n vs Q^2 from SLAC-NE11 [Lung *et al.*, Phys. Rev. Lett. 70, 718(1993)] and the Preliminary Result from Bates E85-05. A fit to these five data points excludes $G_E^n = 0$ at a confidence level of 95%.

to $\vec{q}^{c.m.}$, which as shown in Appendix A corresponds to a laboratory angle of about a few degrees away from the forward direction with respect to $\vec{q}^{lab}$. In Appendix A, we discuss the range of recoil momenta and laboratory scattering angles θ_{nq}^{lab} allowed by the calculations of Arenhövel,[7] which he made explicitly for the kinematic conditions proposed for this experiment. His result for each particular set of kinematic conditions can be converted to a neutron angular spread (with respect to $\vec{q}$) in the lab system within which the neutron polarization $P_{S'}$ will be insensitive to the influence of final-state interactions, meson-exchange currents, and isobar configurations. These angular spreads are larger than the angular acceptance of the neutron polarimeter designed for this experiment. Arenhövel also studied the influence of different deuteron wave functions on the transverse neutron polarization $P_{S'}$. His results for quasifree kinematics (*i.e.*, for neutron emission along $\vec{q}$) show almost no dependence on the deuteron model. The Arenhövel calculation shows that dynamical uncertainties are very small. Finally, Beck and Arenhövel[8] investigated the role of relativistic effects in electrodisintegration of the deuteron for quasifree kinematics. They find that the dependence on the parameterization of the nucleon current in terms of Dirac-Pauli or Sachs form factors is reduced considerably by inclusion of the relativistic contributions.

Rekalo, Gakh, and Rekalo[9] used the relativistic impulse approximation to describe the polarization effects sensitive to G_E^n in deuteron electrodisintegration. In the deuteron quasielastic peak, the neutron polarizations calculated in the relativistic approach agree with the results of Arenhövel.[5] A later study by Mosconi, Pauschenwein, and Ricci[10] of nucleonic and pionic relativistic corrections in deuteron electrodisintegration does not change the results of Arenhövel. Laget[11] investigated the effects of nucleon rescatterings and meson-exchange currents on the determination of the neutron electric form factor in the $d(\vec{e}, e'\vec{n})p$ reaction. He concluded that the measurements of the sideways polarization of the neutron appears to be the most direct way to determine the neutron electric form factor. He concluded also that in quasifree (colinear) kinematics, the neutron polarization in the exclusive reaction is equal to the value expected in the elementary reaction

$n(\vec{e},e')\vec{n}$; in contrast, Friar[12] showed that the neutron polarization in inclusive scattering is scaled down by a large dilution factor. Laget[13] concluded further that corrections from final-state interactions and meson-exchange currents are negligible above $Q^2 = 0.30$ (GeV/c)^2, but that these corrections become sizable below this momentum transfer.

Gari and Krümpelmann[14] reanalyzed the electromagnetic form factor data of the nucleon with emphasis on the neutron electric form factor. They showed that strange quark contributions can reduce the neutron electric form factor at low Q^2 with little effect on the other nucleon form factors. They concluded that "precision measurements of the neutron electric form factor are... of greatest importance for an understanding of nucleon structure."

2. Measurement of G_E^n with a Neutron Polarimeter.

Arnold, Carlson, and Gross[14] (1981) suggested that G_E^n might be determined more accurately by measuring the polarization of the recoil neutron after quasielastic scattering of a longitudinally-polarized electron from an unpolarized neutron. The components of the polarization of the recoil neutron lie in the scattering plane of the electron and the recoil neutron. The polarization component normal to the scattering plane vanishes in the one-photon-exchange approximation. The component of the neutron polarization parallel to the scattering plane but normal to the momentum transfer is proportional to G_E^n. According to the Madison convention (1970), these nonzero components of the neutron polarization are the sideways component $P_{S'}$ and the longitudinal component $P_{L'}$, where L' denotes the direction of the path of the recoil neutron and, in a right-handed coordinate system, S' lies in the scattering plane.

The polarization transfer coefficient of special interest here is $D_{LS'}$ because it is related to G_E^n in the impulse approximation:

$$I_o D_{LS'} = -2\,(G_M^n\, G_E^n)\sqrt{\tau\,(1+\tau)}\tan\left(\frac{\theta_e}{2}\right) \equiv -(G_M^n G_E^n)\,A(\theta_e), \qquad (1)$$

with

$$I_o = (G_E^n)^2 + (G_M^n)^2 \left[\tau + \frac{1}{2}A^2(\theta_e)\right] \equiv (G_E^n)^2 + (G_M^n)^2\, B(\theta_e), \tag{2}$$

Here $\tau \equiv Q^2/4M^2$ and θ_e is the electron scattering angle. The quantity $I_o/(1+\tau)$ is just the cross section (in units of the Mott cross section) for elastic scattering of unpolarized electrons from an unpolarized neutron; that is, $d\sigma/d\Omega = \sigma_{Mott}\, I_o/(1+\tau)$. The Mott cross section $\sigma_{Mott}(\theta_e)$ for a structureless nucleon is given by

$$\sigma_{Mott}(\theta_e) = \left(\frac{\alpha^2}{Q^2}\right)\left(\frac{E'}{E}\right)^2 \cot^2\left(\frac{\theta_e}{2}\right) \tag{3}$$

with

$$Q^2 = 4EE' \sin^2\left(\frac{\theta_e}{2}\right) \tag{4}$$

and

$$\frac{E'}{E} = \frac{1}{1 + 2(E/M)\sin^2(\theta_e/2)}. \tag{5}$$

Here E is the incident electron energy, and α is the fine structure constant.

From Eqs. (1) and (2), the polarization transfer coefficient $D_{LS'}$ is given by

$$D_{LS'} = \frac{-(G_E/G_M)\, A(\theta_e)}{B(\theta_e) + (G_E/G_M)^2}, \tag{6}$$

with

$$A(\theta_e) \equiv 2\sqrt{\tau(1+\tau)}\, \tan\left(\frac{\theta_e}{2}\right). \tag{7}$$

and

$$B(\theta_e) \equiv \tau + \frac{1}{2}A^2(\theta_e). \tag{8}$$

For the case of a longitudinally-polarized electron beam, $D_{LS'}$ is determined from the relation $P_{S'} = P_L D_{LS'}$ by measuring the neutron polarization $P_{S'}$ for a known (measured) longitudinal electron polarization P_L. Note that $D_{LS'} = P_{S'}$ for 100% polarization of the incident beam (*i.e.*, for $P_L = 1$).

From Eq. (6), the ratio G_E^n/G_M^n ($\equiv g$) is given by the following expression:

$$g \equiv \frac{G_E^n}{G_M^n} = \frac{\left(A^2 - 4BD_{LS'}^2\right)^{1/2} - A}{2D_{LS'}}. \tag{9}$$

We discarded the negative sign in front of the square root because of the physical constraint that $G_E^n/G_M^n \to 0$ as $D_{LS'} \to 0$.

Arnold, Carlson, and Gross[14] (1981) calculated the recoil polarization $P_{S'}$ for various nucleon form factors. Plotted in Fig. 5 is the polarization transfer coefficient $D_{LS'}$ at an electron scattering angle $\theta_e = 50^\circ$ for several different form factor models. All five models give plausible estimates for G_E^n within the range covered by the large uncertainties at the present time; however, these models predict large variations in the neutron polarization $P_{S'}$. We are planning to measure the polarization of the recoil neutron at Q^2 = 0.30, 0.50, 1.0, 1.5 and 2.0 $(\mathrm{GeV/c})^2$ with uncertainties that will be able to distinguish between different parameterizations such as the dipole parameterization $G_E^n = -\tau G_M^n$, the Galster parameterization $G_E^n = -\tau G_M^n(1 + 5.6\tau)^{-1}$, and $G_E^n = 0$.

3. Experimental Arrangement

Figure 6 is a schematic diagram of the experimental arrangement. A longitudinally polarized electron beam is incident on an upolarized liquid-deuterium target. A neutron polarimeter measures the transverse polarization $P_{S'}$ of the recoil neutron at a laboratory emission angle θ_n after quasielastic scattering of the electron from an unpolarized neutron in deuterium. A magnetic spectrometer measures the momentum of the electron scattered at an angle θ_e. The recoil neutron is measured in coincidence with the scattered electron. The neutron kinetic energy for the real electron-neutron coincidence events is obtained from a measurement of the neutron time-of-flight from the target to the front analyzer detectors in the polarimeter.

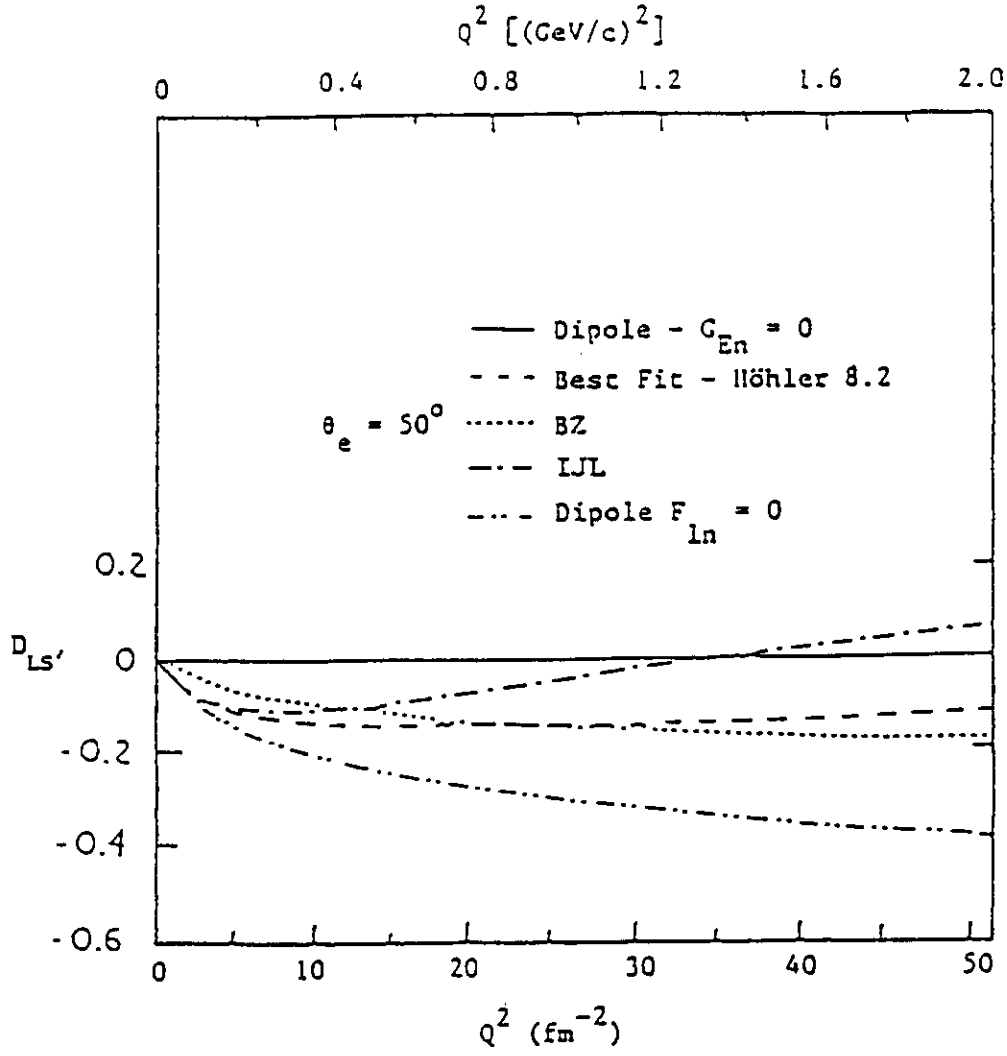

Fig. 5 The Polarization Transfer Coefficient $D_{LS'}$ ($P_{S'}$ for $P_L = 1$) at an Electron Scattering Angle $\theta_e = 50°$ Calculated for Various Nucleon Form Factors as a Function of Q^2.

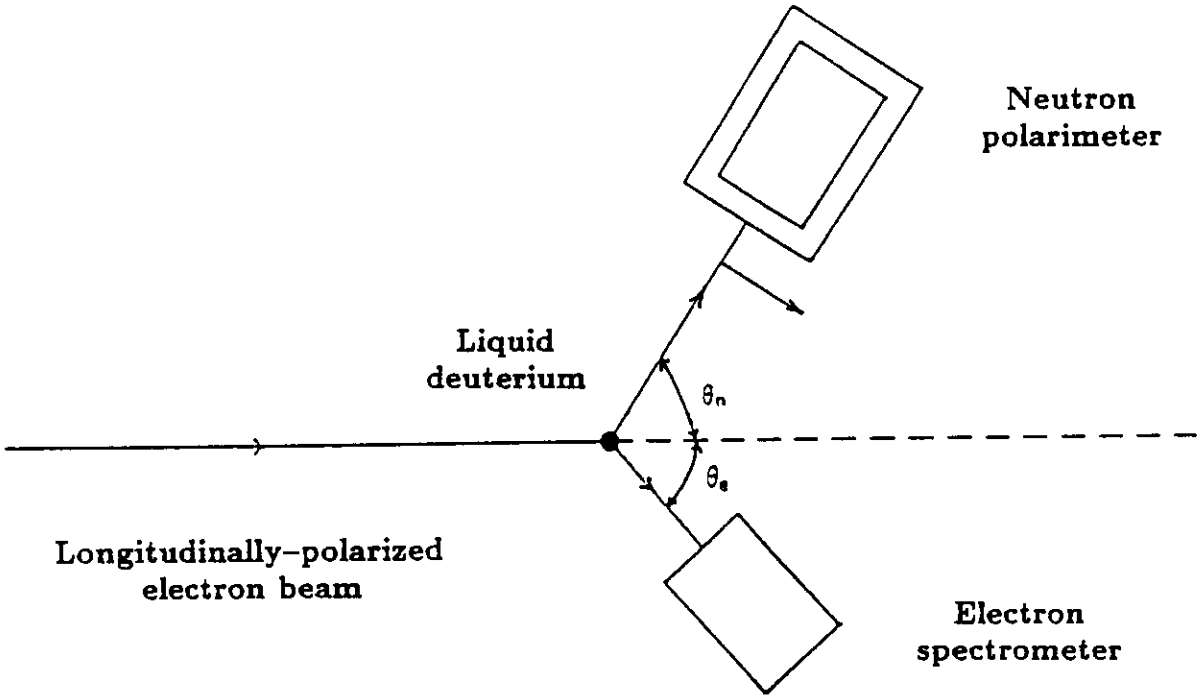

Fig. 6 A Schematic View of the Experimental Arrangement.

3.1 Neutron Polarimeter

The neutron polarimeter shown in Fig. 7 was designed and constructed at Kent State University specifically for measurements of the neutron electric form factor.[15] This polarimeter was calibrated (in August 1989) with polarized neutrons of about 134 MeV (for Bates E85-05) from the Indiana University Cyclotron Facility (IUCF). It will be calibrated at 160 MeV (for Bates E89-04) at the IUCF; and at neutron energies up to 1100 MeV at Saturne. This polarimeter consists of twelve 10.16 cm thick scintillation counters — four primary scatterers (1 through 4) and two sets of four rear detectors (5 through 12). The rear detectors are located at a polar angle θ with respect to the direction of the three-momentum transfer $\vec{q}$. For neutrons of about 135 MeV, $\theta \sim 21°$. The mean flight path from the point midway between primary scatters #2 and #3 to the midpoint of each rear detector array is 2.75 m for the measurements proposed for CEBAF E89-05. All 12 scintillation detectors are mounted with the long dimension normal to the plane of the paper. The rear scintillators are 1.016 m long by 0.254 m high (NE-102) plastic; for CEBAF E89-05, the front scintillators are 1.016 m long by 0.254 m high (NE-102) plastic. [For Bates E85-05, the front scintillators were 0.508 m long by 0.254 m high (BC 517L) mineral oil scintillators. The lucite plastic container for each of the front scintillator has a wall thickness of 0.95 cm]. In front of each set of four detectors is a thin (0.95 cm) plastic scintillation counter to veto charged particles. The design of the polarimeter is based on the properties of n-p scattering as a polarization analyzer. This polarimeter configuration (of four front analyzer scintillators and eight rear detectors for scattered neutrons) requires that the front and rear detector signals be processed independently to allow simplified data processing and easy on-line observation of the relevant polarimeter signals.

Because measurements of the neutron polarization will be made at different values of Q^2, it is necessary to move the neutron polarimeter to neutron scattering angles θ_n that are matched kinematically to the associated electron scattering angles θ_e.

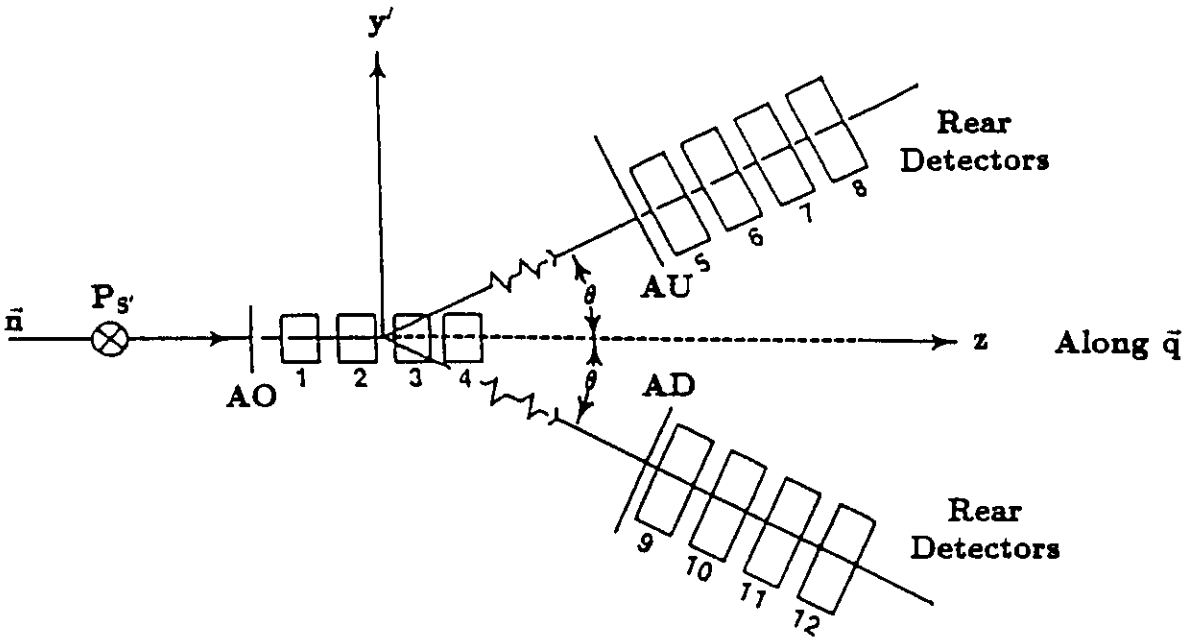

Fig. 7 A Schematic View of the Neutron Polarimeter.

3.2 Steel Collimater and Shielding Enclosure

Based on measurements of neutrons in the test runs at Bates (in February and June 1989), the neutron polarimeter must be contained in a shielding enclosure similar to that shown in Fig. 8A. In Bates E85–05, the rear wall and the two side walls are high density ($\rho = 3.9$ g/cm^3) concrete, four-feet thick, obtained from the Cambridge Electron Accelerator. The roof of the enclosure was covered with high-density concrete roof beams, two-feet thick. The interaction mean free path in normal density ($\rho = 2.3$ g/cm^3) concrete for 75 MeV neutrons is about one foot; therefore, the transmission of 75 MeV neutrons is about 1.8% through four feet; for high-density ($\rho = 3.9$ g/cm^3) concrete, the interaction mean free path is about 18 cm ($\sim$ 7 in) for 75 MeV neutrons and the transmission is about 0.10%. The front wall consists of lead, 4 in. thick, supported by two steel plates, each $1\frac{1}{4}$ in. thick; in addition, steel blocks were used to collimate the front detectors of the polarimeter and to provide additional shielding for the rear detectors. The transmission of neutrons with kinetic energies $\gtrsim$ 100 MeV through this front shielding wall of 10.16 cm of lead plus 6.350 cm of steel is 39 percent. Because this front shielding wall contains about 22 radiation lengths, the reduction in energy of a high–energy photon incident on this front shielding is expected to be so large as to be below the detection threshold. A steel shadow shield, three-feet thick, was used to block the direct path of neutrons from the target to measure the room background.

For CEBAF E89-05, we show the plan view of the shielding enclosure of the neutron polarimeter in Fig. 8B; a side view was shown in Fig. 8A. The rear wall and the two side walls are normal density ($\rho = 2.5$ g/cm^3) concrete, eight-feet thick, obtained from the University of Illinois accelerator. The roof of the enclosure is covered with normal-density concrete roof beams, 42-inches thick. The front wall consists of lead, 4 in. thick, poured into steel containers with 1.25 in. walls. The shielding enclosure together with the supporting base weighs about 1400 tons as listed below:

Shielding Components	Weights (tons)	
1. Shielding Enclosure		**530.4**
1.1 Sides (2.5 g/cm^3 concrete)	400.4	
1.2 Roof (2.5 g/cm^3 concrete)	126.5	
1.3 Floor (steel)	3.5	
2. Collimator		**120.4**
2.1 Steel (7.87 g/cm^3)	83.9	
2.2 Concrete (2.5 g/cm^3)	36.5	
3. Lead-steel Wall		**21.3**
4. Base (3.25 g/cm^3 concrete)		**707.0**
No concrete below steel wall		
TOTAL		**1379.1**

4. Design of the Experiment

4.1 Uncertainty in $G_E^n/G_M^n \equiv g$

We want to design this experiment to measure G_E^n with the smallest practicable uncertainty ΔG_E^n. The polarization transfer coefficient $D_{LS'}$ in the $d(\vec{e}, e'\vec{n})p$ reaction is given by Eq. (6): $D_{LS'} = -gA(\theta_e)/[B(\theta_e) + g^2]$ with $g \equiv G_E^n/G_M^n$, and the kinematic functions $A(\theta_e)$ and $B(\theta_e)$ as defined by Eqs. (7) and (8). From Eq. (6), the ratio g is given by Eq. (9): $g = [(A^2 - 4D_{LS'}^2 B)^{1/2} - A]/(2D_{LS'})$. For a given Q^2, g depends only on the two independent variables θ_e and $D_{LS'}$; accordingly, the relative uncertainty $\Delta g/g$ is given by:

$$\left(\frac{\Delta g}{g}\right)^2 = \left(\frac{\partial \ln g}{\partial \ln D_{LS'}}\right)^2 \left(\frac{\Delta D_{LS'}}{D_{LS'}}\right)^2 + \left(\frac{\partial \ln g}{\partial \theta_e}\right)^2 (\Delta\theta_e)^2 \qquad (10)$$

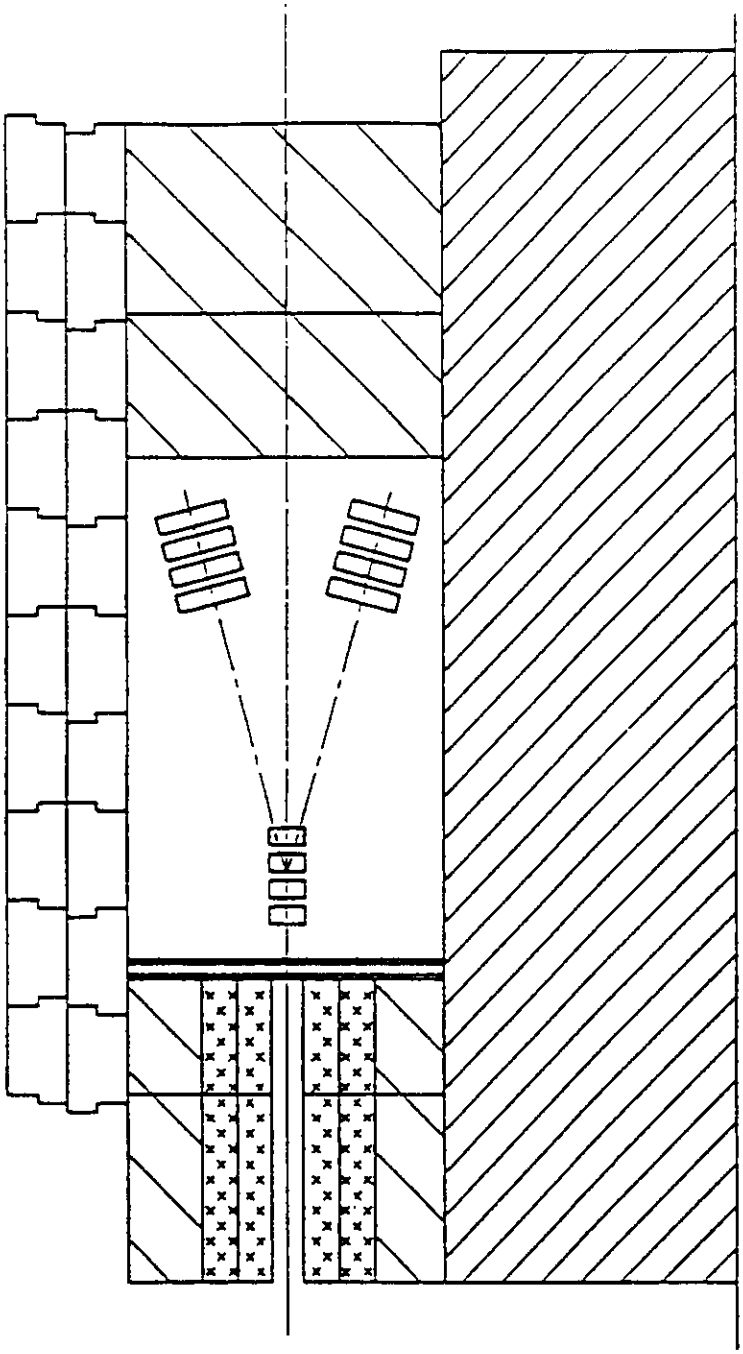

Fig. 8A A Side View of the Steel Collimator and Shielding Enclosure of the Neutron Polarimeter for CEBAF E89-05.

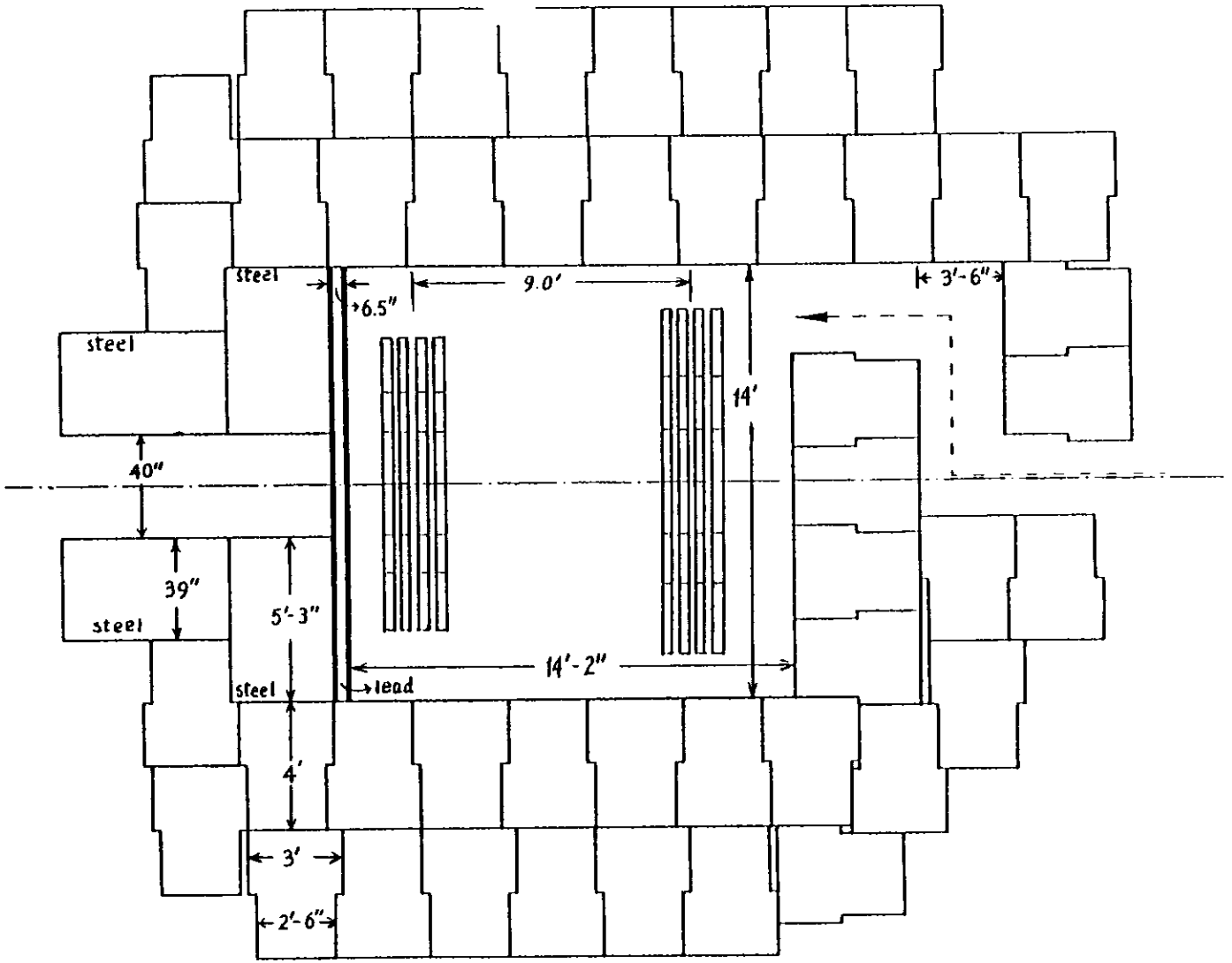

Fig. 8B A Plan View of the Steel Collimator and Shielding Enclosure of the Neutron Polarimeter for CEBAF E89-05.

with

$$\frac{\partial \ln g}{\partial \theta_e} = \left(\frac{\partial \ln g}{\partial \ln A}\right)\left(\frac{d \ln A}{d\theta_e}\right) + \left(\frac{\partial \ln g}{\partial \ln B}\right)\left(\frac{d \ln B}{d\theta_e}\right). \tag{11}$$

In view of Eq. (9) and the following definition of the function f_1,

$$f_1(D_{LS'}, \theta_e) \equiv \frac{A}{(A^2 - 4D_{LS'}^2 B)^{1/2}}, \tag{12}$$

we can write

$$\frac{\partial \ln g}{\partial \ln D_{LS'}} = f_1(D_{LS'}, \theta_e) \tag{13}$$

$$\frac{\partial \ln g}{\partial \ln A} = -f_1(D_{LS'}, \theta_e) \tag{14}$$

$$\frac{\partial \ln g}{\partial \ln B} = \frac{f_1(D_{LS'}, \theta_e) + 1}{2} \tag{15}$$

Substituting these expressions for the partial derivatives into Eq. (10), we obtain

$$\left(\frac{\Delta g}{g}\right)^2 = f_1^2(D_{LS'}, \theta_e)\left(\frac{\Delta D_{LS'}}{D_{LS'}}\right)^2 + f_2^2(D_{LS'}, \theta_e)(\Delta\theta_e)^2, \tag{16}$$

where

$$f_2(D_{LS'}, \theta_e) \equiv -\frac{\partial \ln g}{\partial \theta_e} \equiv f_1 \frac{d \ln A}{d\theta_e} - \frac{f_1 + 1}{2}\frac{d \ln B}{d\theta_e}, \tag{17}$$

$$\frac{d \ln A}{d\theta_e} = \left[1 + \left(\frac{M}{E}\right)^2 \frac{4\tau^2(1 + 2\tau)}{A^2}\right]\frac{1}{\sin\theta_e}, \tag{18}$$

$$\frac{d \ln B}{d\theta_e} = \left[1 + \left(\frac{M}{E}\right)^2 \frac{2\tau^2[1 + 2(1 + 2\tau)\tan^2(\theta_e/2)]}{A^2 \tan^2(\theta_e/2)}\right]\frac{A^2}{B \sin\theta_e}. \tag{19}$$

In the next three sections, we will discuss relative contributions in Eq. (16) to the relative uncertainty $\Delta g/g$.

4.2 Statistical and Scale Uncertainties

The polarization transfer coefficient $D_{LS'}$ is just the scattering asymmetry ξ scaled by the product $A_y P_L$, where A_y is the average analyzing power of the neutron polarimeter, and P_L is the beam polarization:

$$D_{LS'} \equiv \frac{P_{S'}}{P_L} = \frac{\xi}{A_y P_L}. \tag{20}$$

Because a measurement of the scattering asymmetry ξ relates directly to the statistics of the coincidence events N, and because we perform separate measurements of the scale factors P_L and A_y, we make separate estimates of the statistical and the scale uncertainties in $D_{LS'}$. The relative statistical uncertainty in $D_{LS'}$ is given by:

$$\left(\frac{\Delta D_{LS'}}{D_{LS'}}\right)_{stat} = \frac{\Delta \xi}{\xi}. \tag{21}$$

The relative scale uncertainty in $D_{LS'}$ is given by

$$\left(\frac{\Delta D_{LS'}}{D_{LS'}}\right)_{scale} = \left[\left(\frac{\Delta A_y}{A_y}\right)^2 + \left(\frac{\Delta P_L}{P_L}\right)^2\right]^{1/2}. \tag{22}$$

The relative statistical uncertainty in $D_{LS'}$ is inversely proportional to $D_{LS'}$ as shown in Eq. (31) of Section 4.4, while the relative scale uncertainty in $D_{LS'}$ will have a constant value that depends on the precision of the measurements of A_y and P_L. We expect to achieve of about six percent for $(\Delta D_{LS'}/D_{LS'})_{scale}$. [For Bates E85-05, we found $\Delta P_L/P_L \lesssim 0.05$ and $\Delta A_y/A_y \sim 0.05$].

We will project the statistical uncertainty separately from the scale uncertainty, and we will endeavor to obtain a statistical uncertainty that will be comparable to the scale uncertainty. For a quadrature combination of statistical and scale uncertainties, the total relative uncertainty in $D_{LS'}$ is

$$\left(\frac{\Delta D_{LS'}}{D_{LS'}}\right)^2 = \left(\frac{\Delta D_{LS'}}{D_{LS'}}\right)^2_{stat} + \left(\frac{\Delta D_{LS'}}{D_{LS'}}\right)^2_{scale} \tag{23}$$

Now Eq. (16) for the total relative uncertainty in g can be rewritten:

$$\left(\frac{\Delta g}{g}\right)^2 = \left(\frac{\Delta g}{g}\right)^2_{stat} + \left(\frac{\Delta g}{g}\right)^2_{scale} + \left(\frac{\Delta g}{g}\right)^2_{syst} \tag{24}$$

with the statistical uncertainty

$$\left(\frac{\Delta g}{g}\right)_{stat} = f_1 \left(\frac{\Delta D_{LS'}}{D_{LS'}}\right)_{stat} = f_1 \left(\frac{\Delta \xi}{\xi}\right), \tag{25}$$

the scale uncertainty

$$\left(\frac{\Delta g}{g}\right)_{scale} = f_1 \left(\frac{\Delta D_{LS'}}{D_{LS'}}\right)_{scale} = f_1 \left[\left(\frac{\Delta A_y}{A_y}\right)^2 + \left(\frac{\Delta P_L}{P_L}\right)^2\right]^{1/2}, \tag{26}$$

and the systematic uncertainty

$$\left(\frac{\Delta g}{g}\right)_{syst} = f_2(\Delta\theta_e). \tag{27}$$

4.3 Minimum Uncertainty in g

The squared relative uncertainty $(\Delta g/g)^2$ has a minimum, which occurs at an incident energy near the energy that corresponds to the vanishing of the function f_2. We illustrate this statement by plotting in Fig. 9 the squared relative uncertainties versus the incident beam energy for the case of $Q^2 = 1.0$ (GeV/c)^2. Panel (a) is for the Galster parameterization [$g = -\tau/(1 + 5.6\tau)$]; panel (b) is for the dipole parameterization [$g = \tau$]. The $(\Delta g/g)^2_{syst}$ [$= (f_2 \Delta\theta_e)^2$] term in Eq. (24) vanishes when the function f_2 vanishes, and the $(\Delta g/g)^2_{syst}$ term is small compared to either $(\Delta g/g)^2_{stat}$ [$= (f_1 \Delta\xi/\xi)^2$] or $(\Delta g/g)^2_{scale}$ [$= (f_1 \Delta A_y/A_y)^2 + (f_1 \Delta P_L/P_L)^2$] over a range of beam energies around the energy that corresponds to the vanishing of the function f_2. In this energy region, the relative uncertainty $\Delta g/g$ is given to a good

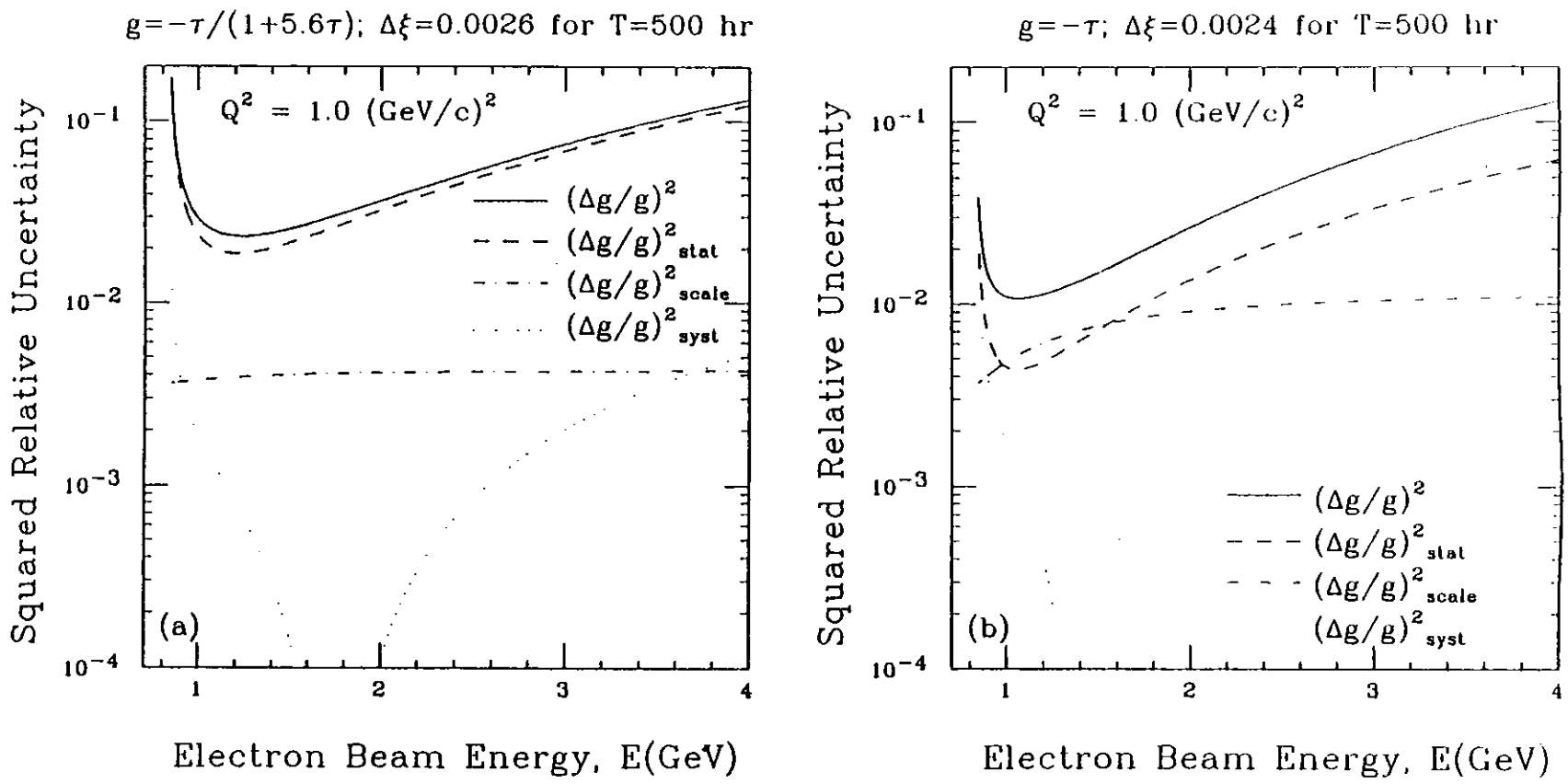

Fig. 9 Contributions to the Squared Relative Uncertainty $(\Delta g/g)^2$.

approximation by

$$\frac{\Delta g}{g} = \left[\left(\frac{\Delta g}{g}\right)^2_{stat} + \left(\frac{\Delta g}{g}\right)^2_{scale}\right]^{1/2} = f_1(D_{LS'}, \theta_e)\frac{\Delta D_{LS'}}{D_{LS'}}. \qquad (28)$$

From Eq. (28) we see that the relative uncertainty $\Delta g/g$ will be a minimum for a desired $\Delta D_{LS'}$ when $D_{LS'}/f_1$ is a maximum.

4.4 Minimum Data Acquisition Time and Figure – of – Merit

In this section, we will show that the data acquisition time will be a minimum for a specified relative statistical uncertainty $(\Delta g/g)_{stat}$ when $(D_{LS'}/f_1)^2\langle\sigma_3\rangle$ is a maximum. Here $\langle\sigma_3\rangle$ is the triple differential cross section averaged over the acceptances. The product $(D_{LS'}/f_1)^2\langle\sigma_3\rangle$ is a figure-of-merit for this experiment.

The data acquisition time T required to obtain N events with a counting rate R is

$$T = \frac{N}{R}. \qquad (29)$$

The number of events N needed to measure the ratio g with a specified relative statistical uncertainty $(\Delta g/g)_{stat}$ is given by

$$N = \left(\frac{1+2/r}{A_y^2 P_L^2}\right)\left[\frac{1}{(\Delta g/g)^2_{stat}(D_{LS'}/f_1)^2}\right], \quad r \equiv \frac{R}{A} \qquad (30)$$

where A_y is the average analyzing power of the polarimeter, P_L is the beam polarization, and r is the ratio of the real counting rate R to the accidental counting rate A. [The derivation of Eq. (30) is based on the fact that the relative statistical uncertainty $\Delta\xi/\xi$ in the measured asymmetry ξ is

$$\left(\frac{\Delta\xi}{\xi}\right)^2 = \frac{1+2/r}{\xi^2 N} = \frac{1+2/r}{P_S^2 A_y^2 N} = \frac{1+2/r}{A_y^2 P_L^2 D^2_{LS'} N} \qquad (31)$$

The first equality in Eq. (31) follows from the fact that $\Delta\xi = (1+2/r)^{1/2}/N^{1/2}$. The factor $1/N^{1/2}$ comes from a binomial distribution for N events. The factor

$(1 + 2/r)^{1/2}$ comes from the subtraction of the accidental rate (A) from the real plus accidental rate ($R + A$). The second equality in Eq. (31) uses the fact that $\xi = P_{S'} A_y$; the third equality uses $P_{S'} = P_L D_{LS'}$. Solving Eq. (31) for N and using Eq. (25), we obtain Eq. (30)].

Now because the real counting rate R is proportional to $\langle \sigma_3 \rangle$, the triple differential cross section averaged over the acceptances, the data acquisition time can be written:

$$T \propto \frac{1}{(\Delta g/g)^2_{stat} (D_{LS'}/f_1)^2 \langle \sigma_3 \rangle} \tag{32}$$

Equation (32) follows from Eq. (30). For a desired relative uncertainty $(\Delta g/g)_{stat}$, we see from Eq. (32) that the data acquisition time T will be a minimum when the quantity $(D_{LS'}/f_1)^2 \langle \sigma_3 \rangle$ is a maximum. The figure-of-merit (FOM) for this experiment is

$$\text{FOM} = \left(\frac{D_{LS'}}{f_1} \right)^2 \langle \sigma_3 \rangle \tag{33}$$

The figure-of-merit is a function of the electron scattering angle θ_e. We illustrate for $Q^2 = 1.0$ (GeV/c)^2 with the dipole parameterization ($g = -\tau$) and the Galster parameterization [$g = -\tau/(1+5.6\tau)$]. Plotted as a function of θ_e is $D_{LS'}$ in Fig. 10, the function f_1 in Fig. 11, and the quantity $(D_{LS'}/f_1)^2$ in Fig. 12. The quantity $(D_{LS'}/f_1)^2$ reaches a maximum at relatively large scattering angles. Because f_1 is larger than unity, the effective polarization transfer coefficient $D^{eff}_{LS'} \equiv D_{LS'}/f_1$ is smaller than the actual polarization transfer coefficient $D_{LS'}$. We will show later in Section 4. 10 that the figure-of-merit is a maximum also at relatively large scattering angles.

4.5 Optimal Kinematic Conditions

In Table I, we list some possible kinematic conditions for five values of Q^2 in the range $0.30 \leq Q^2$(GeV/c)$^2 \leq 2.0$. For each Q^2 point, there is an optimal beam energy (and an associated electron scattering angle) that gives the minimum relative uncertainty $\Delta g/g$, where $g \equiv G^n_E/G^n_M$, achievable in a fixed data

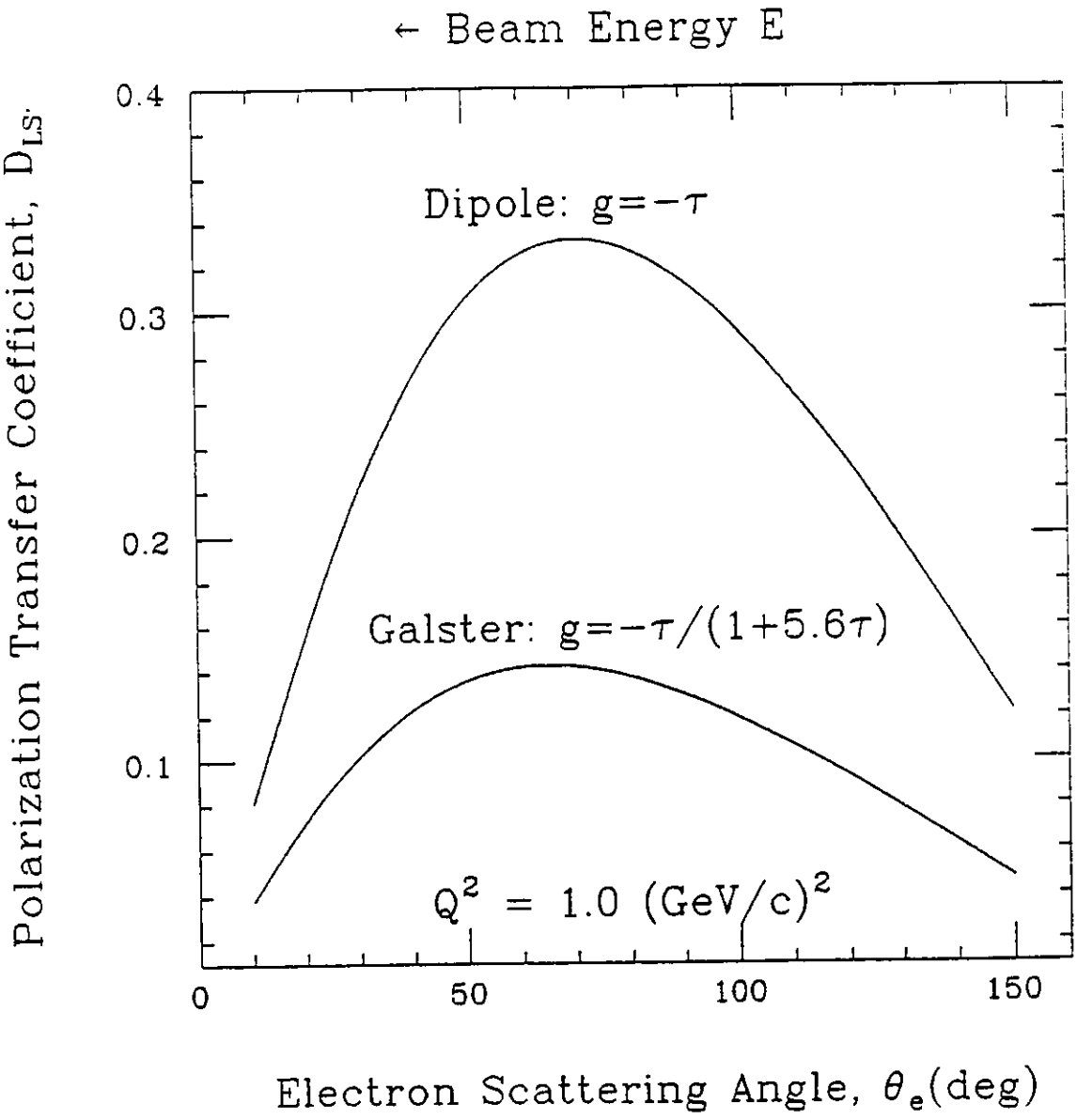

Fig. 10 Polarization Transfer Coefficient $D_{LS'}$ as a Function of Electron Scattering Angle θ_e for $Q^2 = 1.0\ (\mathrm{GeV/c})^2$.

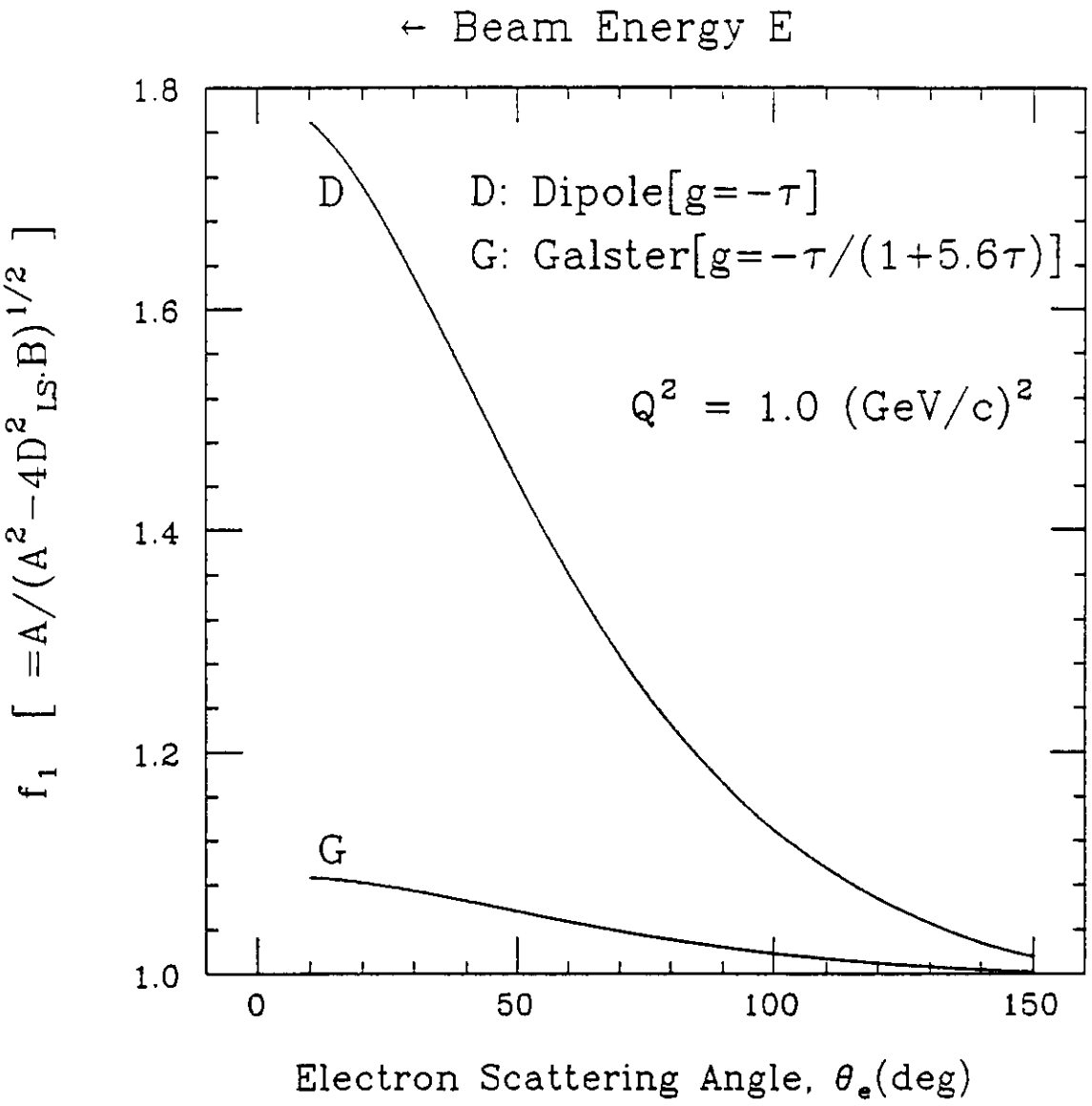

Fig. 11 The Function f_1 vs Electron Scattering Angle θ_e for $Q^2 = 1.0$ $(GeV/c)^2$.

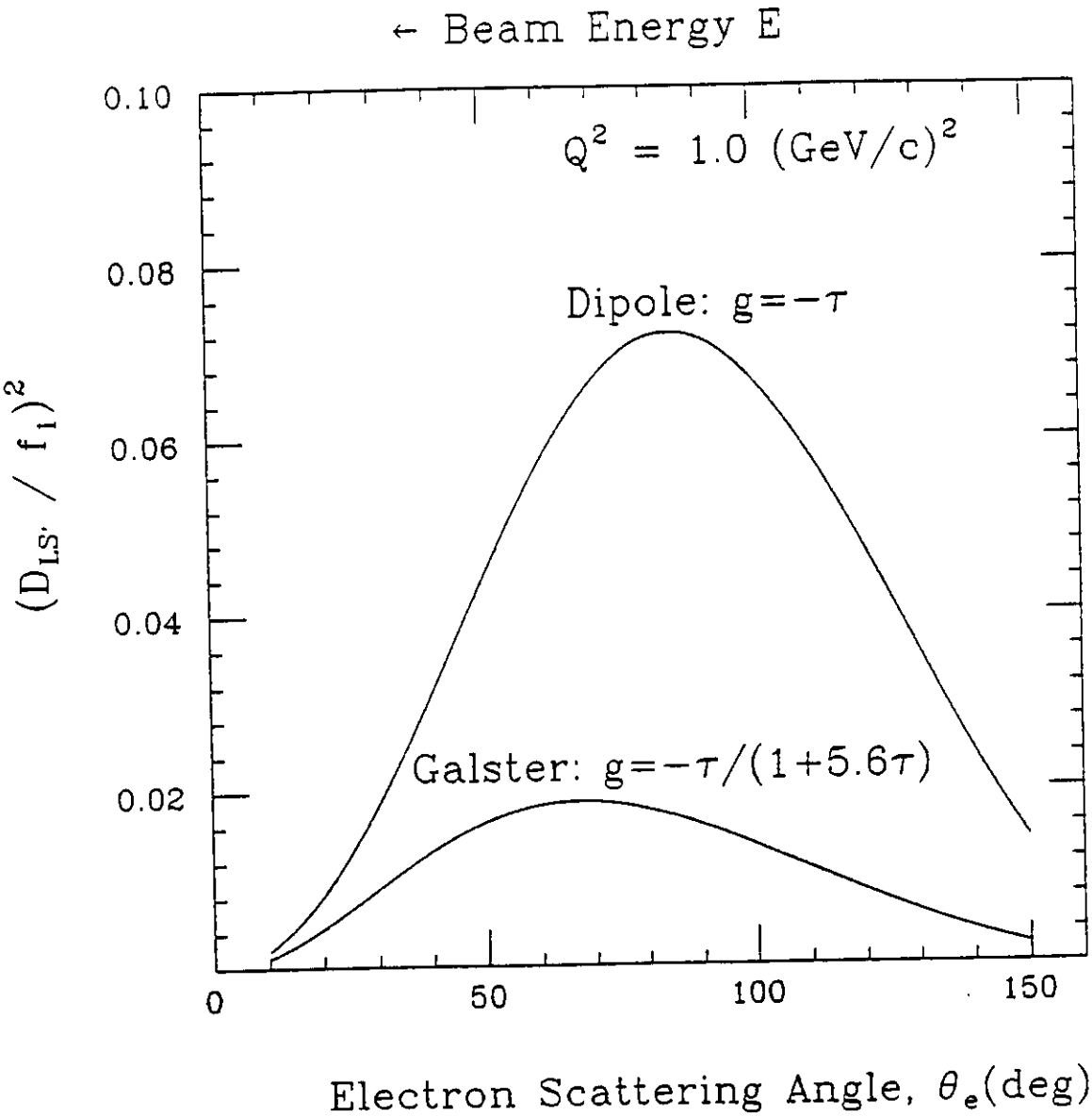

Fig. 12 The Term $(D_{LS'}/f_1)^2$ as a Function of Electron Scattering Angle θ_e for $Q^2 = 1.0$ (GeV/c)^2.

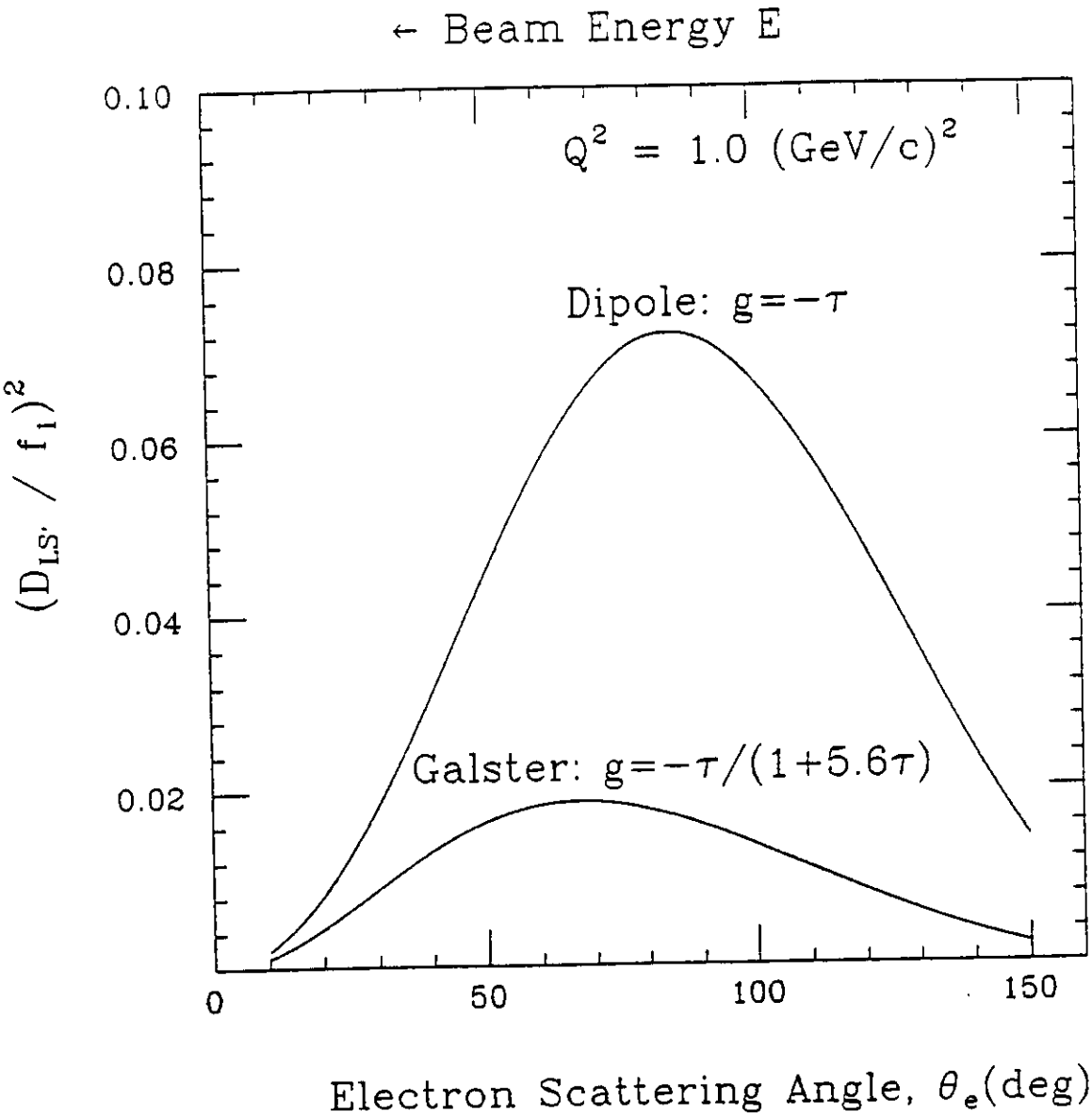

Fig. 12 The Term $(D_{LS'}/f_1)^2$ as a Function of Electron Scattering Angle θ_e for $Q^2 = 1.0$ (GeV/c)^2.

acquisition time. This optimization occurs because the relative uncertainty $\Delta g/g$ is a function of the electron scattering angle, as shown in Section 4.1; accordingly, for a given Q^2 point, the relative uncertainty $\Delta g/g$ for a fixed data acquisition time is a function of the beam energy. Because the data acquisition time to measure the neutron polarization $P_{S'}$ is proportional to the inverse square of the polarization uncertainty $\Delta P_{S'}$, the relative uncertainty $\Delta g/g$ will be a minimum for a given data acquisition time (or fixed $\Delta P_{S'}$ or $\Delta D_{LS'}$) when $P_{S'}$ (or $D_{LS'}$) is near its maximum value. Actually, as shown in Section 4.2, the relative uncertainty $\Delta g/g$ is a minimum for a given data acquisition time when $D_{LS'}/f_1$ is a maximum, where $f_1 = A/(A^2 - 4\,B\,D_{LS'}^2)^{1/2}$ with A and B given in Eqs. (7) and (8). Note that the optimal beam energy depends on the model chosen for the form factor; for example, if G_E^n follows the dipole parameterizaion ($g = -\tau$), the optimal energy to measure G_E^n for $Q^2 = 2.0$ (GeV/c)^2 is 1.6 GeV, while it is 3.2 GeV if G_E^n follows the Galster parameterization [$g = -\tau/(1 + 5.6\tau)$].

We determined the optimal kinematic conditions for the dipole and the Galster parameterizations of G_E^n, and then selected a single set of optimal kinematic conditions based on the study of these two parameterizations. The optimal kinematic conditions selected from Table I are listed in Table II(a) for the dipole parameterization and in Table II(b) for the Galster parameterization; and in Table II(c), we give the single set of optimal kinematic conditions chosen for the design of this experiment. Because the energies of the electron beams at CEBAF are available only with discrete values 0.8 GeV apart, we determined the optimal beam energies for the measurement at each of the five proposed Q^2 points.

Table I. Possible Kinematic Conditions

Q^2	T_n	P_n	E	θ_e	θ_n	P'_e
$(GeV/c)^2$	(MeV)	(MeV/c)	(GeV)	(deg)	(deg)	(MeV/c)
2.0	1064	1771	4.0	23.9	42.0	2935
			3.2	31.4	38.9	2134
			2.4	46.6	33.1	1333
			1.6	100.0	17.2	533
1.5	799	1464	4.0	19.8	47.5	3201
			3.2	25.5	45.0	2401
			2.4	36.4	40.5	1600
			1.6	65.6	29.8	799
1.0	532	1133	4.0	15.6	54.3	3462
			3.2	19.7	52.5	2667
			2.4	27.3	49.1	1867
			1.6	45.0	41.2	1066
0.50	267	757	4.0	10.5	64.1	3732
			3.2	13.4	62.7	2931
			2.4	18.0	60.5	2132
			1.6	28.0	55.9	1333
			0.8	65.7	39.8	532
0.30	160	572	4.0	8.0	69.6	3839
			3.2	10.1	68.5	3038
			2.4	13.7	66.8	2238
			1.6	20.8	63.4	1439
			0.8	45.1	52.3	638

Table II. Selected Kinematic Conditions for Hall C in the Reversed-Quad Mode

(a) For the Dipole Parameterization

Q^2 $(GeV/c)^2$	T_n (MeV)	P_n (MeV/c)	E (GeV)	θ_e (deg)	θ_n (deg)	P'_e (MeV/c)
2.0	1064	1771	1.6	100.0*	17.2†	533
1.5	799	1464	1.6	65.6	29.8	799
1.0	532	1133	1.6	45.0	41.2	1066
0.50	267	757	0.8	65.7	39.8	532
0.30	160	572	0.8	45.1	52.3	638

(b) For the Galster Parameterization

Q^2 $(GeV/c)^2$	T_n (MeV)	P_n (MeV/c)	E (GeV)	θ_e (deg)	θ_n (deg)	P'_e (MeV/c)
2.0	1064	1771	3.2	31.4	38.9	2133
1.5	799	1464	2.4	36.4	40.5	1600
1.0	532	1133	1.6	45.0	41.2	1066
0.50	267	757	1.6	28.0	55.9	1333
0.30	160	572	0.8	45.1	52.3	638

(c) For the Experiment

Q^2 $(GeV/c)^2$	T_n (MeV)	P_n (MeV/c)	E (GeV)	θ_e (deg)	θ_n (deg)	P'_e (MeV/c)
2.0	1064	1771	2.4	46.6	33.1	1333
1.5	799	1464	1.6	65.6	29.8	799
1.0	532	1133	1.6	45.0	41.2	1066
0.50	267	757	0.8	65.7	39.8	532
0.30	160	572	0.8	45.1	52.3	638

* HMS restricted to $\theta_e \leq 90°$

† Not allowable by shielding at $x = 9.70$ m

4.6 Flight Path and Energy Resolutions

As shown later in Section 5, background from inelastic processes can be reduced to a small fraction of quasielastic signal events by a suitable choice of $\Delta\theta_n$, the horizontal angular acceptance of the neutron polarimeter. Based on these Monte Carlo simulations, we chose $\Delta\theta_n = \pm 3.00°$. Later in Section 4.8, we will show that this horizontal angular acceptance of $\Delta\theta_n = \pm 3.00°$ is a suitable choice in terms of horizontal angular matching for each of the kinematic conditions proposed in the last section. The flight path x (to the center of the front detector array of the neutron polarimeter) that corresponds to a horizontal angular interval $\Delta\theta_n = \pm 3.00° = \pm 52.4$ mr for front neutron detectors of width $w = 40$ in $= 1.016$ m is 9.70 m:

$$x = \frac{w}{2\Delta\theta_n} = \frac{1.016}{2 \times 52.4 \times 10^{-3}} = 9.70 \text{ m}. \tag{34}$$

At this flight path and for a resolving time $\tau = 0.70$ ns (fwhm), neutron energy resolutions are listed in Table III for the proposed points at Q^2 between 0.30 and 2.0 $(\text{GeV/c})^2$. The neutron energy resolutions are calculated from the usual relation:

$$\frac{\Delta T}{T} = \gamma(\gamma+1)\left[\left(\frac{\Delta t}{t}\right)^2 + \left(\frac{\Delta x}{x}\right)^2\right]^{\frac{1}{2}}. \tag{35}$$

Table III. Neutron Energy Resolution*

Four-Momentum-Transfer Squared	Neutron Energy	Lorentz Factor	Flight Time	Energy Resolution	
Q^2 $(\text{GeV/c})^2$	T_n (MeV)	γ	t (ns)	$\Delta T/T$ (%)	ΔT (MeV)
2.0	1064	2.131	36.6	7.2	77
1.5	799	1.848	38.5	5.5	44
1.0	532	1.564	42.1	3.9	21
0.50	267	1.284	51.6	2.5	6.7
0.30	160	1.170	62.3	1.9	3.1

* For $x = 9.70$ m, $\Delta x = \pm 5.0$ cm, $\Delta t = \pm 0.35$ ns.

4.7 Comparision of Hall A HRS and Hall C HMS

In Table IV, we list some features of the Hall A High Resolution Spectrometer (HRS) and the Hall C High Momentum Spectrometer (HMS) for both normal- and reversed-quad operating modes. In the normal operating mode, the magnet in the Hall A High Resolution Spectrometer (HRS) has a vertical-to-horizontal aspect ratio of 1.85; the horizontal angular acceptance is ± 30 mr, and the vertical angular acceptance is ± 55 mr. The momentum acceptance of the Hall A magnet is ± 5 percent for electrons with momenta from 0.3 to 4 GeV/c. In the normal operating mode, the HMS in the Hall C has a vertical-to-horizontal aspect ratio of 3.30; the horizontal angular acceptance is ± 25 mr, and the vertical angular acceptance is ± 83 mr. The momentum acceptance of the Hall C HMS is ± 10 percent, which is twice that of the Hall A HRS. For either the Hall A HRS or the Hall C HMS magnet, the minimum angle between the beam and the magnet is 12.5°; the maximum angle of the electron arm is 165° for the HRS and 90° for the HMS. It should be noted that both the Hall A HRS and the Hall C HMS can be run in the reversed-quad operating mode. We are particularly interested in the reversed-quad mode with the Hall C HMS because the horizontal angular acceptance increases to slightly more than twice that of the Hall A HRS in the normal operating mode. This increase in the horizontal angular acceptance results in a significant increase in the coincidence counting rate, which will reduce the statistical uncertainties if the experiment is to run for the same time period; or conversely, the data acquisition time to achieve a desired statistical uncertainty will be about one-half of that with the Hall A HRS.

Table IV. Comparison of Hall A HRS and Hall C HMS

Parameters	Hall A HRS		Hall C HMS	
	Normal	Reversed-Quad	Normal	Reversed-Quad
Maximum Horizontal Angular Acceptance, $\Delta\theta_e$(mr)	±30	±36	±25	±62
Maximum Vertical Angular Acceptance, $\Delta\phi_e$(mr)	±55	±98	±82.5	±22.5
Minimum Scattering Angle, θ_{min}(deg)	12.5	22*	12.5	12.5
Maximum Scattering Angle, θ_{max}(deg)	165	165	90	90
V/H ratio	1.85	2.72	3.30	0.36
H/V ratio	0.55	0.37	0.30	2.75
Momentum Acceptance $\Delta p/p$ (%)	±5	±4	±10	±5
Maximum Momentum, p_{max}(GeV/c)	4.0	2.4	7.5	7.5
Momentum Resolution, $\delta p/p$	1×10^{-4}	3×10^{-4}	$< 1 \times 10^{-3}$	$\sim 1 \times 10^{-3}$
E89-05 Design Horizontal Angular Acceptance, $\Delta\theta_e$(deg)	1.70	2.00	1.43	3.40
Target-Collimator Distance, z_{TC}(m)	1.67	0.85	1.2†	1.2†
Target-Aperture Distance, z_{TA}(m)	1.36	0.56‡	1.2†	1.2†
Central Path Length, L_0(m)	23.4	23.4	27	27
Spread in Path Length, $\Delta L/L_0$	±1/80	±1/80	$\pm 2.5 \times 10^{-3}$	$\pm 1.25 \times 10^{-3}$
Time Resolution, $\Delta t/t$	±1/80	±1/80	$\pm 2.5 \times 10^{-3}$	$\pm 1.25 \times 10^{-3}$
Time Spread, Δt(ps)	±1000	±1000	±2250	±1125

* Q1-Q2 moved forward 80 cm. Front quad Q1 has an aperture of 15 cm.

† Collimator defines acceptance for 5.0 cm target.

‡ Radius of scattering chamber is 50 cm.

4.8 Solid – Angle Matching for Electron – Neutron Coincidences; Acceptances and Solid Angles

In order to optimize the electron-neutron coincidence rate, we want to provide

the best match between the angular acceptance of the electron spectrometer and the angular acceptance of the neutron polarimeter; thus, we examine the matching in the horizontal (θ) and the vertical (ϕ^v) planes.

• Horizontal (θ) Matching

For the case of elastic scattering from a stationary neutron, transverse momentum conservation ($p_\perp^e = p_\perp^n$) in the electron scattering plane requires that

$$p_\perp^e \equiv p_e \sin\theta_e = p_\perp^n \equiv p_n \sin\theta_n. \tag{36}$$

Longitudinal-momentum conservation in the reaction plane requires

$$p_o = p_\parallel^e + p_\parallel^n = p_e \cos\theta_e + p_n \cos\theta_n. \tag{37}$$

Here the momentum of the incident electron $p_o = E$ in the approximation $m_e = 0$ (which we will use throughout this section), the momentum of the elastically-scattered electron $p_e = E' = E/[1 + 2(E/M)\sin^2(\theta_e/2)]$, and p_n is the momentum of the recoil neutron. These momentum conservation equations lead to the following kinematical relations:

$$\tan\theta_n = \frac{1}{(1 + E/M)\tan(\theta_e/2)}, \tag{38}$$

$$p_n = \frac{E \sin\theta_e \sqrt{1 + (1 + E/M)^2 \tan^2(\theta_e/2)}}{1 + 2(E/M)\sin^2(\theta_e/2)} = 2M\sqrt{(1+\tau)\tau}. \tag{39}$$

The last equality in Eq. (39) follows by using Eqs. (4) and (5). From Eqs. (38) and (39), we have the horizontal angular kinematical matching functions $(d\theta_n/d\theta_e)^k$:

$$\left(\frac{d\theta_n}{d\theta_e}\right)^k_E = \frac{-(1 + E/M)}{2[1 + (1 + E/M)^2 \tan^2(\theta_e/2)]\cos^2(\theta_e/2)}, \tag{40}$$

$$\left(\frac{d\theta_n}{d\theta_e}\right)^k_{Q^2} = \frac{-1}{2[1 + (1 + E/M)^2 \tan^2(\theta_e/2)]} \left[\frac{1 + E/M}{\cos^2(\theta_e/2)} - \frac{\sqrt{\tau}}{\sin(\theta_e/2)\sqrt{1 + \tau\sin^2(\theta_e/2)}}\right]. \tag{41}$$

Here the subscript E in $(d\theta_n/d\theta_e)^k_E$ or Q^2 in $(d\theta_n/d\theta_e)^k_{Q^2}$ denotes *fixed* E or *fixed* Q^2, respectively. The superscript k denotes that these expressions arise from kinematics. In Fig. 13, we plot $(d\theta_n/d\theta_e)^k_{Q^2}$ as a function of θ_e for the five Q^2 points proposed; and in Fig. 14, we show $(d\theta_n/d\theta_e)^k_E$ as a function of θ_e for the five E values (0.8, 1.6, 2.4 3.2, and 4.0 GeV) available at CEBAF. In this experiment, the horizontal angular acceptance of the electron arm is fixed, viz., $\Delta\theta_e = \pm 3.40^\circ$ with the Hall C high-momentum spectrometer (HMS) in the reversed-quad mode; therefore, because Q^2 is not fixed in the experiment, the kinematically-matched horizontal angular spread of the neutron flux can be calculated:

$$(\Delta\theta_n)^k_E = \left(\frac{d\theta_n}{d\theta_e}\right)^k_E \Delta\theta_e, \tag{42}$$

It should be pointed out that the kinematically-matched horizontal angular spread of the neutron flux for fixed Q^2 is given by:

$$(\Delta\theta_n)^k_{Q^2} = \left(\frac{d\theta_n}{d\theta_e}\right)^k_{Q^2} \Delta\theta_e. \tag{43}$$

Now, the neutron flux will be spread further because of the Fermi motion of the neutron inside the deuteron before breaking up; this Fermi spreading can be estimated by

$$(\Delta\theta_n)^F = \frac{\Delta q}{q}, \tag{44}$$

where q is the three-momentum transfer, and Δq is given by the Fermi momentum in the deuteron, with a typical value $\Delta q = \sqrt{2M\epsilon} \sim \pm 65$ MeV/c. In view of Eqs. (42) and (44), the total horizontal angular spread of the neutron flux for a given beam energy E is

$$\Delta\theta_n = (\Delta\theta_n)^k_E + (\Delta\theta_n)^F = \left(\frac{d\theta_n}{d\theta_e}\right)^k_E \Delta\theta_e + \frac{\Delta q}{q}. \tag{45}$$

In Table V, we present the estimated horizontal angular spread of the neutron flux. From Table V, we see that $\Delta\theta_n$ is larger than ± 4.0 degrees for all the proposed

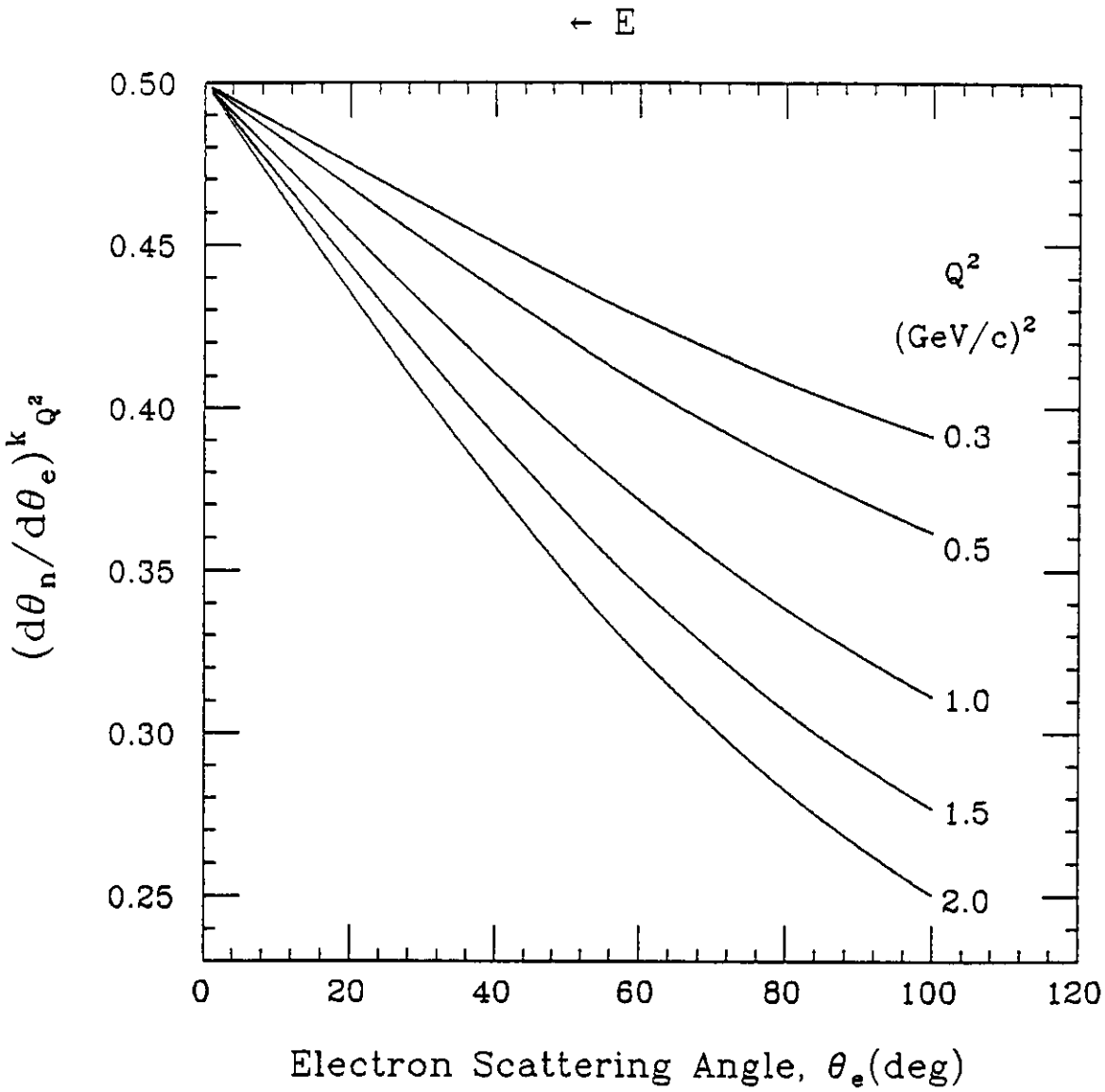

Fig. 13 $(d\theta_n/d\theta_e)^k_{Q^2}$ vs Electron Scattering Angle θ_e.

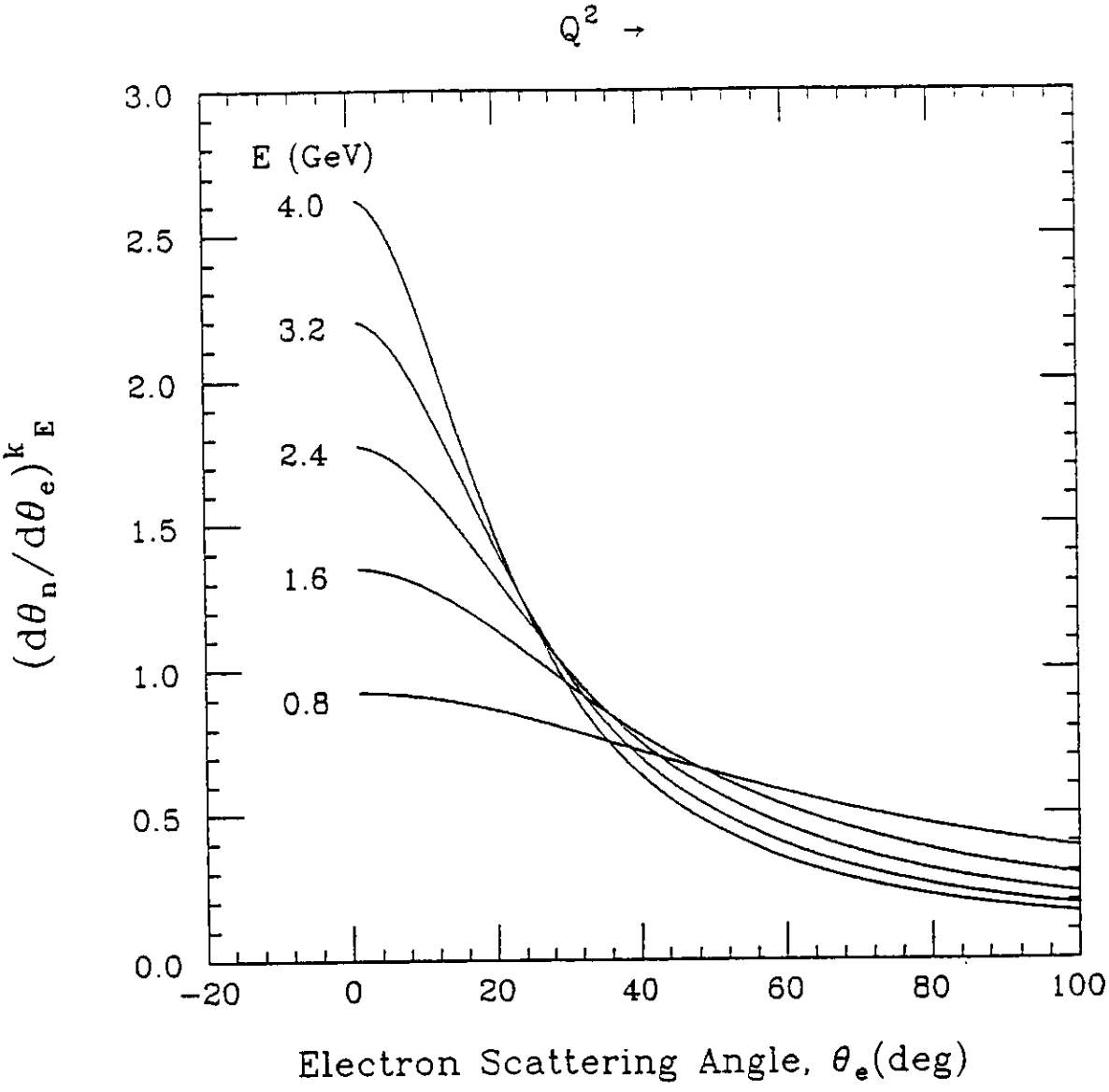

Fig. 14 $(d\theta_n/d\theta_e)^k_E$ vs Electron Scattering Angle θ_e.

kinematic conditions; however, the background study described in Section 5 favors a smaller $\Delta\theta_n$ in order to discriminate against neutrons associated with inclusive pion emission. Here we choose a horizontal angular acceptance of $\Delta\theta_n = \pm 3.0°$ for all the Q^2 points proposed.

Table V. Estimated Horizontal Angular Spread of Neutron Flux

Q^2 $(\mathrm{GeV/c})^2$	θ_e (deg)	E (GeV)	θ_n (deg)	q (MeV/c)	$(d\theta_n/d\theta_e)^k_E$	*$(\Delta\theta_n)^k_E$ (deg)	†$(\Delta\theta_n)^F$ (deg)	$\Delta\theta_n$ (deg)
2.0	46.6	2.4	33.1	1771	0.630	±2.14	±2.11	±4.25
1.5	65.6	1.6	39.8	1464	0.474	±1.61	±2.55	±4.16
1.0	45.0	1.6	41.7	1133	0.703	±2.39	±3.29	±5.68
0.5	65.7	0.8	39.8	757	0.540	±1.84	±4.91	±6.75
0.3	45.1	0.8	52.3	572	0.682	±2.32	±6.51	±8.83

* Calculated with $\Delta\theta_e = \pm 3.40°$

† Estimated with $\Delta q = \pm 65$ MeV/c

• Vertical (ϕ^v) Matching

For electron scattering planes that are rotated about the beam axis through a small azimuthal angle ϕ with respect to the horizontal (reference) plane, the sum of the momentum components perpendicular to the horizontal plane must vanish; that is,

$$p^e_\perp \sin\phi_e = p^n_\perp \sin\phi_n, \tag{46}$$

or, in view of Eq. (36),

$$p_{e'} \sin\theta_e \sin\phi_e = p_n \sin\theta_n \sin\phi_n. \tag{47}$$

In this experiment, the vertical angular acceptance $\Delta\phi^v$ in the neutron arm is fixed with given flight path $x(= 9.70$ m) and vertical dimension $h(= 0.254$ m) of the front detector in the neutron polarimeter; therefore, the vertical angular acceptance $\Delta\phi^v$ in the electron arm has to be matched to that of the neutron arm.

For the neutron arm,

$$\Delta\phi_n^{\mathrm{v}} = \Delta\phi_n \sin\theta_n = \frac{h}{2x}, \tag{48}$$

and

$$\Delta\phi_n = \frac{\Delta\phi_n^{\mathrm{v}}}{\sin\theta_n} = \frac{h}{2x\sin\theta_n} \tag{49}$$

where θ_n is the neutron scattering angle. For $h = 0.254$ m and $x = 9.70$ m, values of $\Delta\phi_n$ are listed in Table VI for each Q^2 point.

Because $\phi_e = \pi - \phi_n$, the magnitudes of the azimuthal angular intervals for electrons and neutrons are equal:

$$\Delta\phi_e = |\Delta\phi_n|. \tag{50}$$

Hence, this equality means that

$$\Delta\phi_e^{\mathrm{v}} = \Delta\phi_e \sin\theta_e = |\Delta\phi_n| \sin\theta_e = \frac{h}{2x}\frac{\sin\theta_e}{\sin\theta_n}. \tag{51}$$

The values of $\Delta\phi_e^{\mathrm{v}}$ are listed also in Table VI.

Finally, the solid angle $\Delta\Omega$ is:

$$\Delta\Omega = 4\Delta\theta\ \Delta\phi\ \sin\theta = 4\Delta\theta\ \Delta\phi^{\mathrm{v}}, \tag{52}$$

where $2\Delta\theta$ is the horizontal angular acceptance, and $2\Delta\phi\sin\theta \equiv 2\Delta\phi^{\mathrm{v}}$ is the vertical angular acceptance. The numerical values of the electron and neutron solid angles are given in Table VI for the five proposed Q^2 points.

Table VI. Acceptances and Solid Angles

(a) For Hall A HRS (normal mode) and $\Delta\theta_e = \pm 1.70°$, $\Delta\theta_n = \pm 26.2$ mr

Q^2 (GeV/c)^2	E (GeV)	Δp_e $^{\odot}$ (MeV/c)	$\Delta\phi_n$ * deg (mr)	$\Delta\phi_e^x$ $^{\otimes}$ deg (mr)	$\Delta\Omega_e$ * (msr)	$\Delta\Omega_n$ * (msr)	$2\Delta p_e \Delta\Omega_e \Delta\Omega_n$ (10^{-4}MeV $\cdot$ sr^2)
2.0	2.4	53	1.37(24.0)	1.00(17.4)	2.07	1.37	3.03
1.5	1.6	32	1.51(26.3)	1.37(24.0)	2.85	1.37	2.50
1.0	1.6	43	1.14(19.9)	0.801(14.0)	1.67	1.37	1.95
0.50	0.80	21	1.17(20.5)	1.07(18.7)	2.21	1.37	1.29
0.30	0.80	26	0.95(16.5)	0.674(11.8)	1.39	1.37	0.97

(b) For Hall C HMS (reversed-quad mode) and $\Delta\theta_e = \pm 3.40°$, $\Delta\theta_n = \pm 52.4$ mr

Q^2 (GeV/c)^2	E (GeV)	Δp_e $^{\odot}$ (MeV/c)	$\Delta\phi_n$ * deg (mr)	$\Delta\phi_e^x$ $^{\otimes}$ deg (mr)	$\Delta\Omega_e$ * (msr)	$\Delta\Omega_n$ * (msr)	$2\Delta p_e \Delta\Omega_e \Delta\Omega_n$ (10^{-4}MeV $\cdot$ sr^2)
2.0	2.4	53	1.37(24.0)	1.00(17.4)	4.13	2.74	12.1
1.5	1.6	32	1.51(26.3)	1.37(24.0)	5.69	2.74	9.98
1.0	1.6	43	1.14(19.9)	0.806(14.1)	3.34	2.74	7.80
0.50	0.80	21	1.17(20.5)	1.07(18.7)	4.42	2.74	5.17
0.30	0.80	26	0.95(16.5)	0.674(11.8)	2.78	2.74	3.89

$\odot$ $\Delta p_e = \pm 0.040\, p_e$

$\star$ $\Delta\phi_e = |\Delta\phi_n| = h/(2x \sin\theta_n)$, $\Delta\phi_n^x = h/2x = 0.750° = 13.1$ mr, $\Delta\Omega_n = 4\Delta\theta_e \Delta\theta_n^x$

$\otimes$ $\Delta\phi_e^x = \Delta\phi_e \sin\theta_e$

$*$ $\Delta\Omega_e = 4\Delta\theta_e \Delta\phi_e^x$

4.9 Efficiency and Analyzing Power of the Neutron Polarimeter

It is necessary to calibrate the neutron polarimeter by measuring the analyzing power and the efficiency at the neutron energy associated with a given value of Q^2. Such a calibration was carried out in 1989 for neutrons of 135 MeV. A report of these measurements appears in Appendix B.

To measure the analyzing power A_y (averaged over the polarimeter acceptances), we measure the average scattering asymmetry ξ for neutrons of known sideways polarization $P_{S'}$.

$$A_y = \frac{\xi}{P_{S'}}. \tag{53}$$

To obtain neutrons of known polarization $P_{S'}$, we use the $0^+ \rightarrow 0^+$ transition to the isobaric analog state in the $^{14}C(\vec{p},\vec{n})^{14}N$ (E_x = 2.31 MeV) reaction at zero degrees. If the proton polarization P_p is perpendicular to the reaction plane, and if the interaction conserves angular momentum $\vec{J}$ and parity π, then the general relation is

$$P_n[1 + P_p A_y(\theta)] = P(\theta) + D_{NN'}, \tag{54}$$

where $D_{NN'}$ is the polarization transfer coefficient. At $\theta = 0°$, the polarization function $P(0°) = 0$ and $A_y(0°) = 0$. Hence, for a $0^+ \rightarrow 0^+$ transition, $D_{NN'} = 1$ and

$$P_n = P_p. \tag{55}$$

We know P_n by measuring P_p in the upstream polarimeter at the IUCF.

To measure the double-scattering efficiency of the neutron polarimeter, we use the known cross section at 0° for the $^{12}C(p,n)^{12}N$(g.s.) and $^{14}C(p,n)^{14}N$ (3.95 MeV,1^+) reactions. For an incident proton beam of 138.4 MeV, the neutron energy is 119.7 MeV for the $^{12}C(p,n)^{12}N$(g.s.) reaction and 133.8 MeV for the $^{14}C(p,n)^{14}N$ (3.95 MeV, 1^+) reaction.

Results for the performance of the polarimeter at a neutron energy of 133.8 MeV are summarized in Table VII. Actually, the results for A_y and ξ depend on the value of the so-called velocity ratio R_v. The velocity ratio R_v ratio is defined as the ratio of the scattered neutron velocity v_{sc} (obtained from the time-of-flight between a scatterer in the front array and a rear detector) to the velocity v_{np} calculated for $n-p$ scattering. The velocity ratio observed at the IUCF is shown in Fig. 15. The events above an R_v cut just below unity are mostly neutron scatterings from

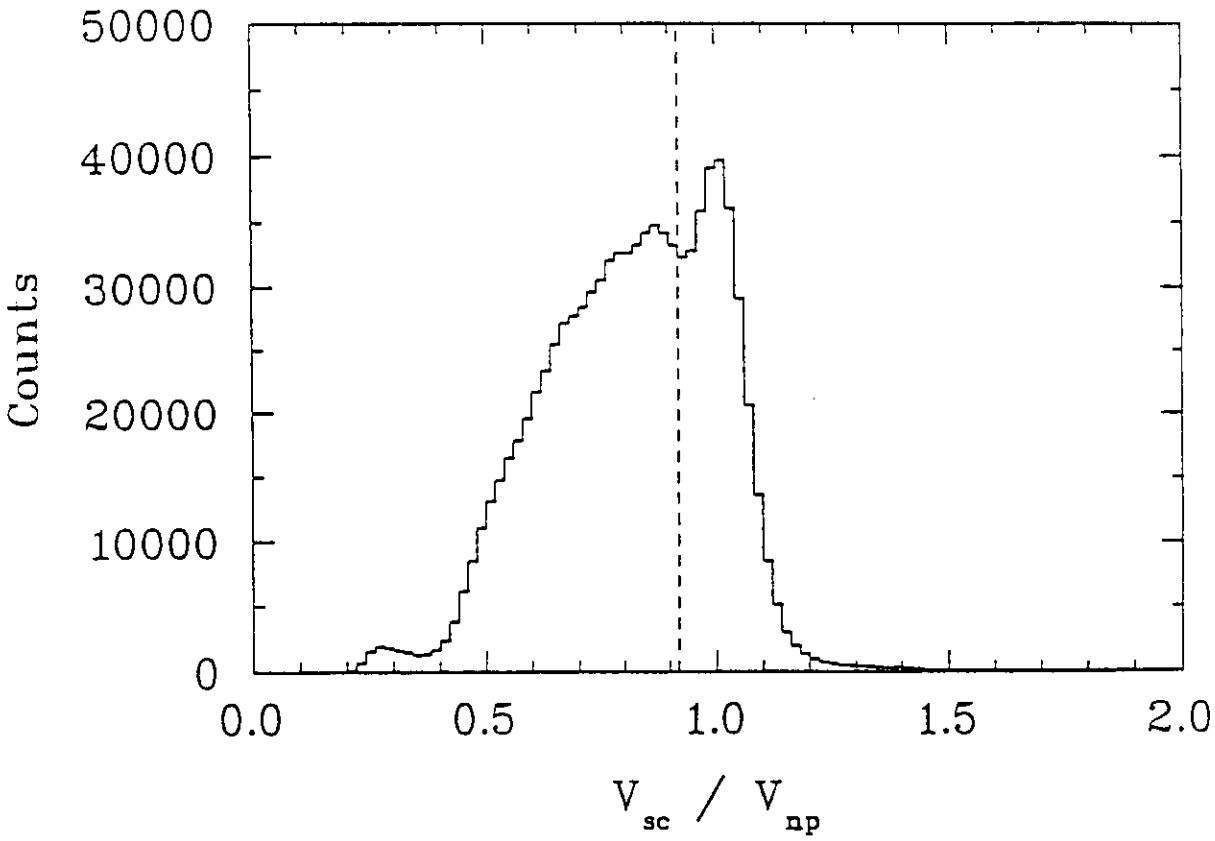

Fig. 15 The Velocity Ratio V_{sc}/V_{np} Spectrum at 134 MeV.

a proton, wherease events above a lower R_v cut include scatters from hydrogen and carbon nuclei. Shown in Fig. 16 is the analyzing power A_y [in panel (a)], the efficiency ϵ [in panel (b)], and the figure of merit $A^2\epsilon$ [in panel (c)].

We are able to project the polarimeter efficiency as a function of neutron energy from calculations of the neutron-proton differential cross section based on nucleon-nucleon phase shifts. We used the SAID program of Arndt *et al.*[16] to plot $\sigma(\theta)$, $A_y(\theta)$, and the product $A_y^2\sigma$ as a function of the neutron scattering angle in the laboratory for neutron energies corresponding to each Q^2. These plots are shown in Figs. 17, 18, 19, 20 and 21 for neutron energies of 160, 267, 531, 798, and 1063 MeV, respectively. From these data, we estimated the optimum neutron-proton scattering angle θ^*, the efficiency ϵ, and the average analyzing power A_y of the polarimeter at each neutron energy. The values of ϵ and A_y used to calculate count rates and uncertainties are listed in Table VIII. Also listed in Table VIII is the scattering angle θ^* for a maximum figure-of-merit.

Table VII. Performance for Neutron Energy of 133.8 MeV

Scatterer	Analyzing Power, A_y	Efficiency $\epsilon(\%)$	Figure of Merit $A_y^2\epsilon = \eta(\%)$
H (mostly)	0.43	0.26	0.048
H + C	0.39	0.28	0.043

The neutron polarimeter will be calibrated at Saturne at Saclay. We are interested in measuring the analyzing power A_y, averaged over the polar and azimuthal angular acceptances of the neutron polarimeter, with a relative statistical uncertainty $\Delta A_y/A_y$ of about two percent. This value of $\Delta A_y/A_y$ will not limit the uncertainty in our measurements of G_E^n.

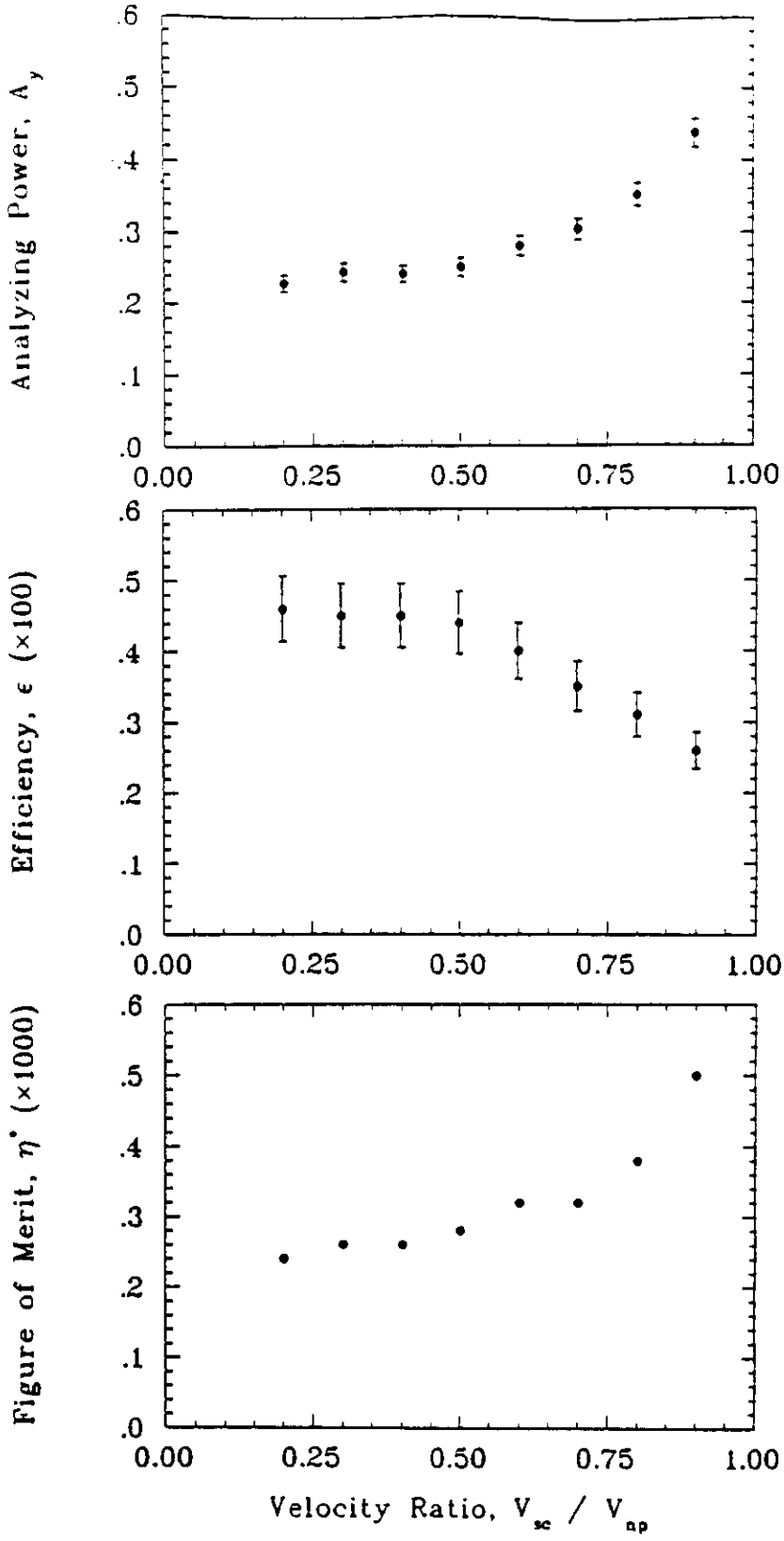

Fig. 16 The Analyzing Power A_y, the Efficiency ϵ, and the Figure of Merit $A_y^2\epsilon$ as a Function of Velocity Ratio V_{sc}/V_{np} for Neutron Kinetic Energy $T_n = 134$ MeV.

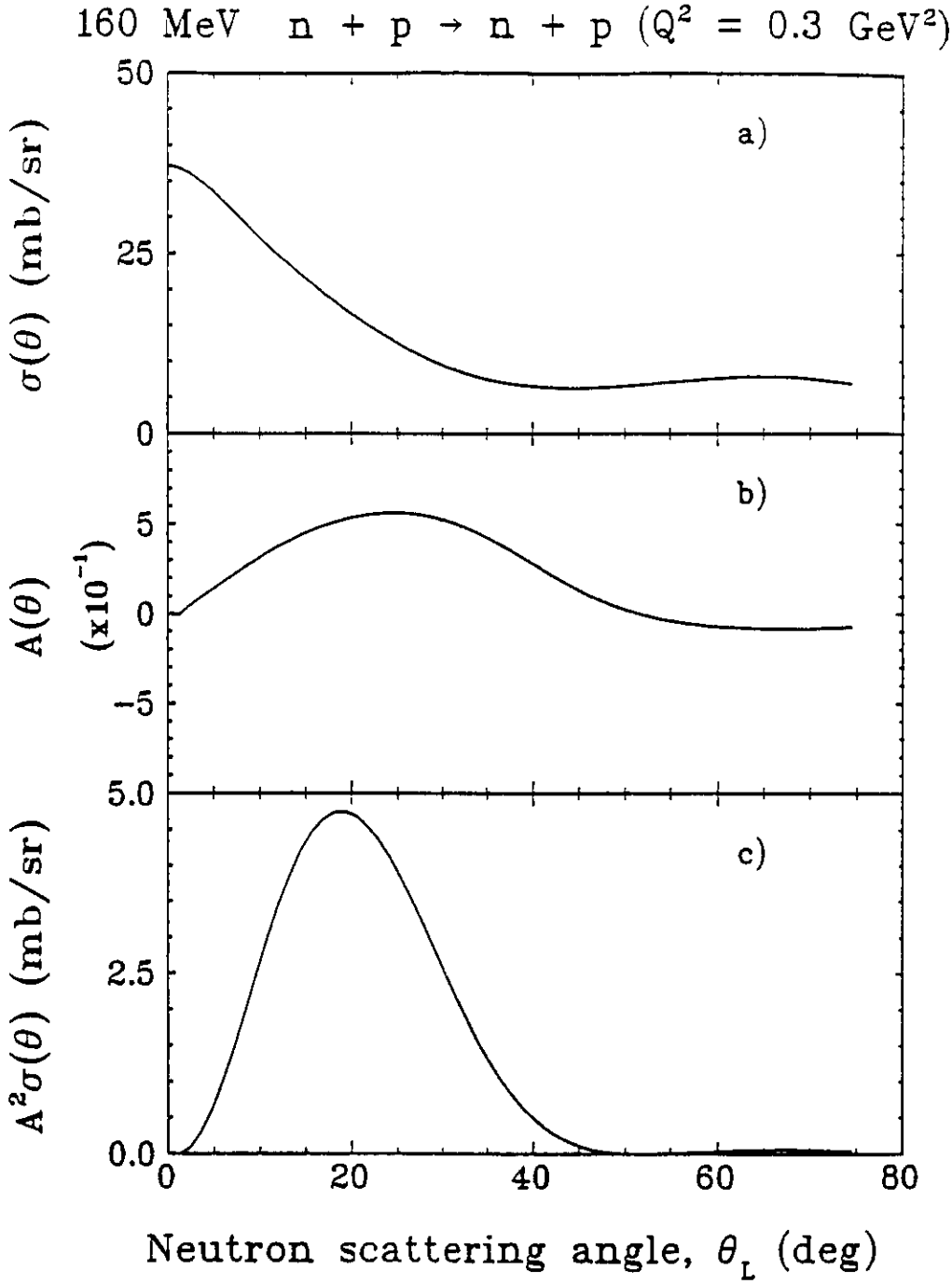

Fig. 17 The n-p Scattering Cross Section $\sigma(\theta)$, the Analyzing Power $A(\theta)$, and $A^2\sigma$ vs the Neutron Scattering Angle θ for T_n = 160 MeV.

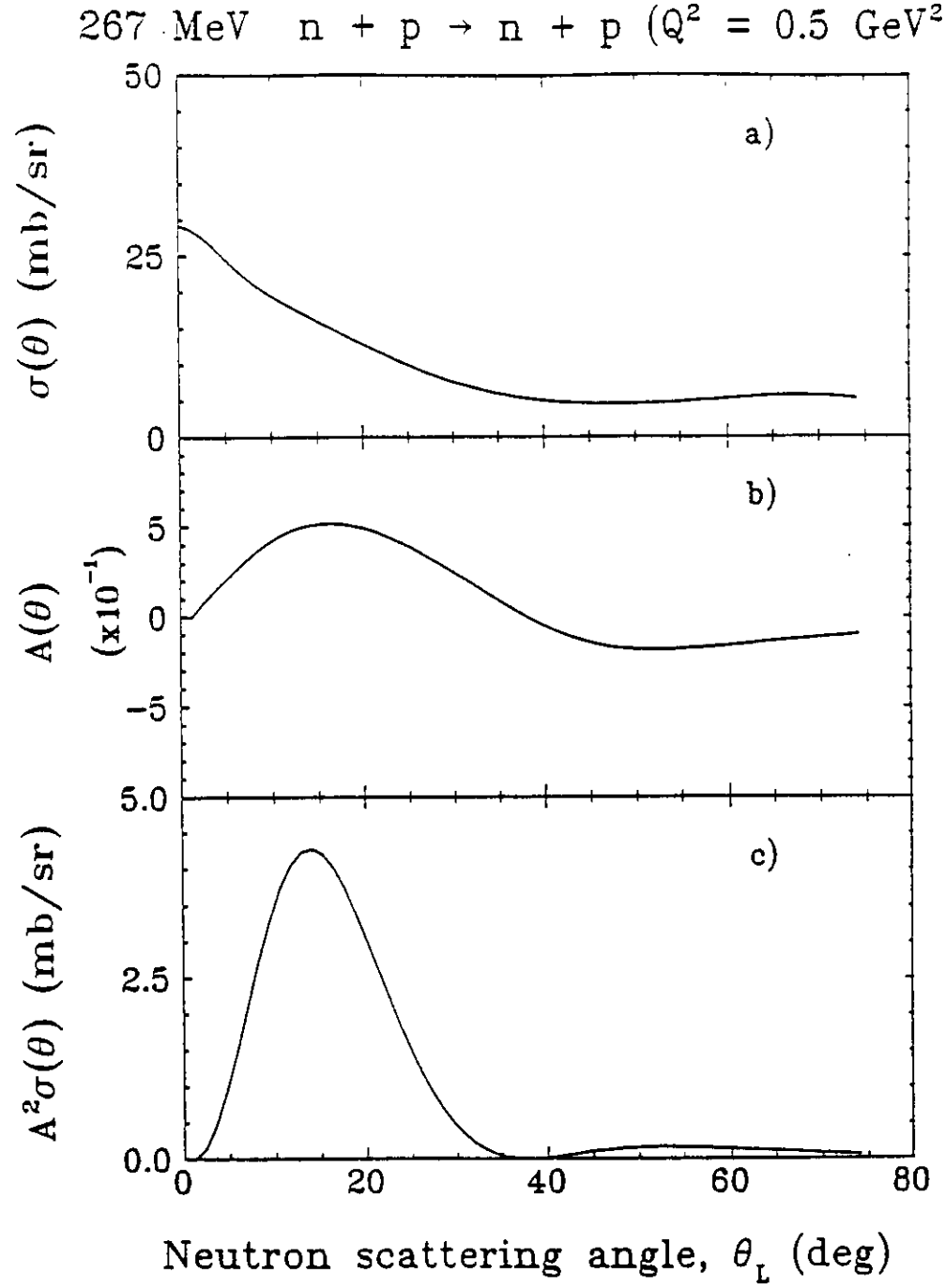

Fig. 18 The n-p Scattering Cross Section $\sigma(\theta)$, the Analyzing Power $A(\theta)$, and $A^2\sigma$ vs the Neutron Scattering Angle θ for T_n = 267 MeV.

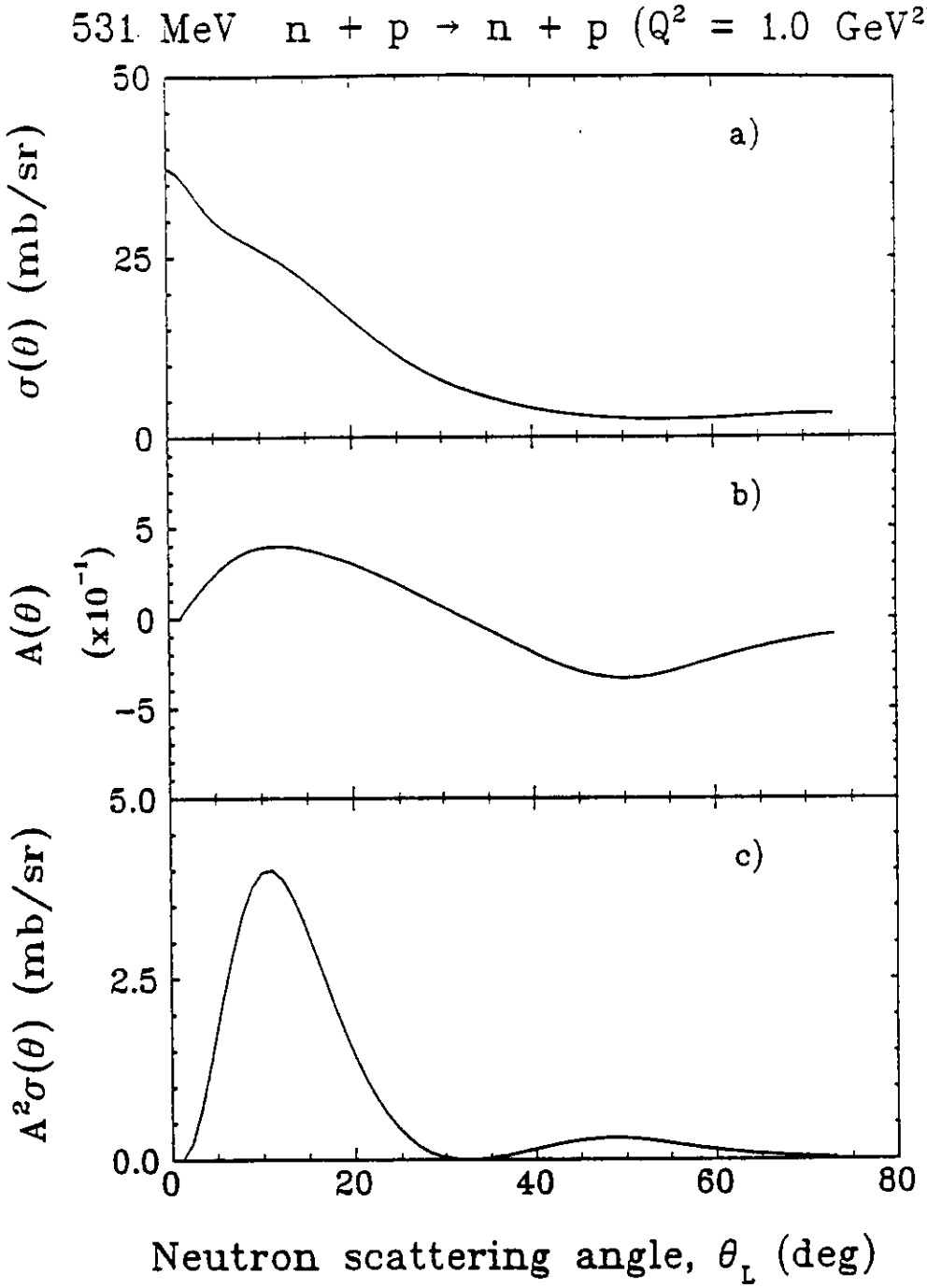

Fig. 19 The n-p Scattering Cross Section $\sigma(\theta)$, the Analyzing Power $A(\theta)$, and $A^2\sigma$ vs the Neutron Scattering Angle θ for $T_n = 531$ MeV.

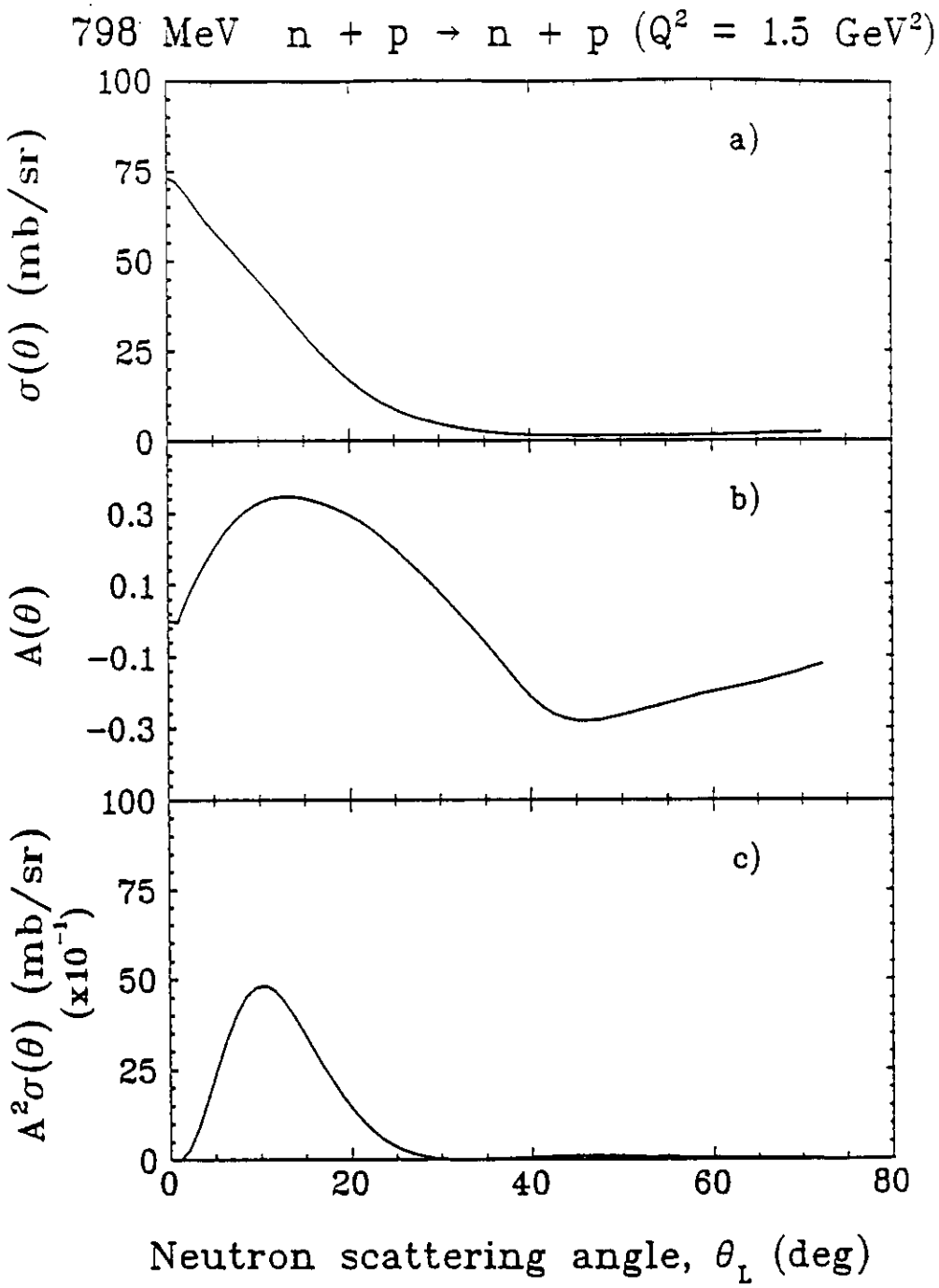

Fig. 20 The n-p Scattering Cross Section $\sigma(\theta)$, the Analyzing Power $A(\theta)$, and $A^2\sigma$ vs the Neutron Scattering Angle θ for T_n = 798 MeV.

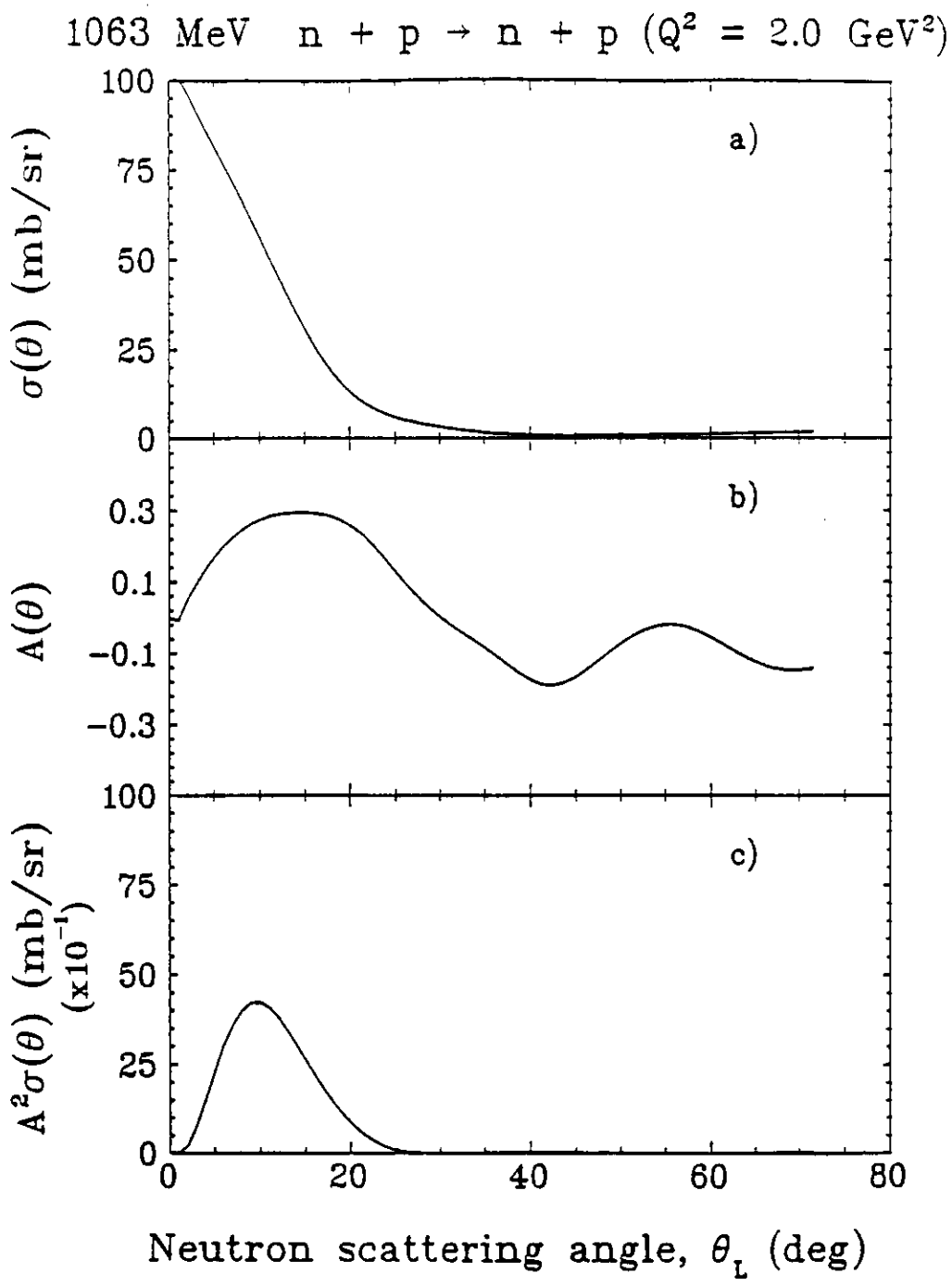

Fig. 21 The n-p Scattering Cross Section $\sigma(\theta)$, the Analyzing Power $A(\theta)$, and $A^2\sigma$ vs the Neutron Scattering Angle θ for T_n = 1063 MeV.

Table VIII. Analyzing Power and Efficiency
of the Polarimeter
for Different Neutron Kinetic Energies

Q^2 $(\mathrm{GeV/c})^2$	T_n (MeV)	θ^* (deg)	$\sigma(\theta^*)$ (mb/sr)	A_y	ϵ_p (%)
0.30	160	19.3	17.2	0.40	0.16
0.50	267	14.1	16.6	0.40	0.16
1.0	531	11.1	25.3	0.34	0.12†
1.5	798	11.1*	41.0	0.29	0.19†
2.0	1063	11.1*	50.4	0.23	0.24†

* For a maximum FOM, $\theta^* = 10.5°$ for $T_n = 798$ MeV and $\theta^* = 10.0°$ for $T_n = 1063$ MeV. We plan to keep the mean scattering angle at 11.1° to shield the rear detectors from the direct neutrons from the target.

† The mean distance between the front and the rear detector arrays is 2.75 m (instead of 2.0 m) in order to shield the rear detectors from the direct path of neutrons from the target.

4.10 Coincidence Counting Rates

The electron-neutron coincidence counting rate R can be estimated from the following expression:

$$R = L\langle\sigma_3(p_e,\theta_e,\theta_n)\rangle(2\Delta p_e)\Delta\Omega_e\,\Delta\Omega_n\,\epsilon_n\,\epsilon_{wc}\,l_{wc}\,\epsilon_{rad}\,l\,t \tag{56}$$

where the luminosity

$$L(\mathrm{cm}^{-2}\mathrm{s}^{-1}) = F\,\frac{N_o}{A}\,\rho x \tag{57}$$

and

F = incident flux of longitudinally-polarized electrons, (electron/s)

ρ_n = numerical density of deuterium nuclei, cm^{-3}

ρx = target thickness of LD_2 [= (0.162 g/cc)(5 cm) = 0.81 g/cm^2 LD_2]

N_o = Avogadro's number (= 6.022×10^{23} nuclei/mole)

A = mass number of target (=2.14 g/mole)

Δp_e = half of the electron momentum bite, MeV

$\Delta\Omega_e$ = electron solid angle, sr

$\Delta\Omega_n$ = neutron solid angle, sr

$\langle\sigma_3(p_e, \theta_e, \theta_n)\rangle$ = triple differential cross section per deuterium nucleus for scattering an electron with an incident energy E at an angle θ_e into a solid angle $\Delta\Omega_e$, with a momentum p_e in an interval Δp_e, and with a recoil neutron at an angle θ_n into a solid angle $\Delta\Omega_n$. This cross section is the value averaged over the experimental acceptances; it has units of $cm^2/MeV \cdot sr^2$

ϵ_n = efficiency of the neutron polarimeter

ϵ_{wc} = track reconstruction efficiency of the wire chambers ($\sim$ 0.97 based on Bates E85-05)

l_{wc} = live-time fraction of the wire chambers ($\sim$ 0.95, based on Bates E85-05)

ϵ_{rad} = radiative correction factor ($\sim$ 0.83)

l = live-time fraction of the data acquisition system ($\sim$ 0.95)

t = transmission of neutrons from the target to the polarimeter through lead shielding designed to attenuate photons emitted from the target (For neutrons with $T \gtrsim 100$ MeV through 4 in. Pb contained within two $1\frac{1}{4}$ in steel plates, $t = 0.39$).

To obtain values of the triple differential cross section averaged over the experimental acceptances, we used the Monte Carlo program MCEEP of P. E. Ulmer.[17] These averaged cross sections $d^3\sigma_e/(dp_e\, d\Omega_e\, d\Omega_n) \equiv \langle\sigma_3\rangle$ are listed in the fourth and fifth columns of Table IX for the Galster and the dipole parameterizations of G_E^n, respectively, for the optimal kinematic conditions in

Table II. In Fig. 22 for $Q^2 = 1.0$ (GeV/c)^2, we plot the figure of merit (FOM) [viz., $(D_{LS'}/f_1)^2\langle\sigma_3\rangle$] as a function of the electron scattering angle θ_e for both the dipole and the Galster parameterizations of G_E^n. The maximum occurs near $\theta_e = 40°$ for the Galster parameterization and near 60° for the dipole parameterization. Studies at other Q^2 points all result in relatively large electron scattering angles for a maximum figure-of-merit. This result is somewhat surprising because it is commonly thought that the figure-of-merit should be maximized at small electron scattering angles where the triple differential cross section maximizes. Shown for dipole parameterization as an example with the dashed curve in Fig. 22 is a "figure-of-merit" associated with a "point" triple differential cross section σ_3 instead of an averaged cross section $\langle\sigma_3\rangle$. This "figure-of-merit" is maximized when $\theta_e \to 0$. We will give a detailed explanation for this surprising difference of the maximum FOM between FOM($\langle\sigma_3\rangle$) and FOM(σ_3) in the next section.

Table IX. Triple Differential Cross Sections and Single-Arm Cross Sections†

Q^2	θ_e	E	$\frac{d^3\sigma(p_e,\theta_e,\theta_n)}{dp_e d\Omega_e d\Omega_n} \equiv \langle\sigma_3\rangle$		$\frac{d^2\sigma(p_e,\theta_e)}{dp_e d\Omega_e}$		$\frac{d\sigma(\theta_n, p_e^{th}<p_e<p_e^{max})}{d\Omega_n}$	
(GeV/c)^2	(deg)	(GeV)	(nb/sr^2 − MeV)		(nb/sr − MeV)		(nb/sr)	
			G*	D*	G*	D*	G*	D*
2.0	46.6	2.4	0.13	0.17	0.014	0.019	3058	4032
1.5	65.5	1.6	0.23	0.27	0.0086	0.0073	2843	3306
1.0	45.0	1.6	1.23	1.43	0.068	0.074	2044	2405
0.50	65.5	0.80	3.66	3.84	0.30	0.32	1497	1576
0.30	45.0	0.80	11.7	12.1	2.35	2.40	847	874

† For Hall C acceptances in the reversed-quad mode

* G refers to the Galster parameterization; and D to the dipole parameterization of G_E^n.

For the Hall C acceptances, the electron-neutron coincidence counting rates R for a luminosity of 3.2×10^{38} cm^{-2}s^{-1} are listed in Table X, and for an *effective*

luminosity of 2.8×10^{38} cm^{-2}s^{-1} in Table XI. The experimental conditions for obtaining the count rates for this experiment are listed in Table XII.

Table X. Counting Rates, Data Acquisition Times, and Uncertainties with a Luminosity $L = 3.2 \times 10^{38}$ cm^{-2}s^{-1}

Q^2	θ_e	E	Case*	R	A	r	$N^\star$	ξ	$\Delta\xi$	$T^\otimes$	$\Delta G_E^{n\ddagger}$	$\Delta G_E^n/G_E^{n\ddagger}$
(GeV/c)^2	(deg)	(GeV)		(min^{-1})	(min^{-1})	$\equiv R/A$	($\times 10^5$)	($\times 10^{-2}$)	($\times 10^{-2}$)	(hr)	($\times 10^{-2}$)	
2.0	46.6	2.4	I	1.96	0.060	33	0.94	0	0.33	800	0.52	–
			II	2.66	0.080	33	1.28	3.48	0.29		1.30	0.17
			III	2.01	0.060	34	0.97	1.11	0.33		0.55	0.31
1.5	65.5	1.6	I	2.35	0.15	16	0.71	0	0.40	500	0.63	–
			II	2.80	0.15	19	0.84	4.46	0.36		1.01	0.12
			III	2.39	0.15	16	0.72	1.55	0.40		0.66	0.26
1.0	45.0	1.6	I	6.06	0.684	8.9	1.82	0	0.26	500	0.51	–
			II	7.15	0.876	8.2	2.15	3.94	0.24		0.85	0.091
			III	6.24	0.684	9.1	1.87	1.77	0.26		0.55	0.15
0.50	65.5	0.8	I	16.2	1.53	11	2.43	0	0.22	250	0.48	–
			II	17.3	1.72	10	2.60	3.97	0.22		0.58	0.063
			III	16.5	1.53	11	2.48	2.32	0.22		0.51	0.099
0.30	45.0	0.80	I	38.8	5.12	7.6	3.50	0	0.19	150	0.52	–
			II	41.2	5.39	7.6	3.71	2.76	0.18		0.61	0.076
			III	39.9	5.12	7.8	3.59	1.93	0.19		0.56	0.10

* Case I: $G_E^n = 0$; Case II: $G_E^n = -\tau G_M^n$; Case III: $G_E^n = -\tau G_M^n (1 + 5.6\tau)^{-1}$

$\star$ $N = \frac{1+2/\tau}{(A_y \Delta P_{y'})^2}$ with A_y given in Table VIII

$\otimes$ $T(\text{hr}) = \frac{N}{60R(\text{min}^{-1})}$

‡ Statistical only

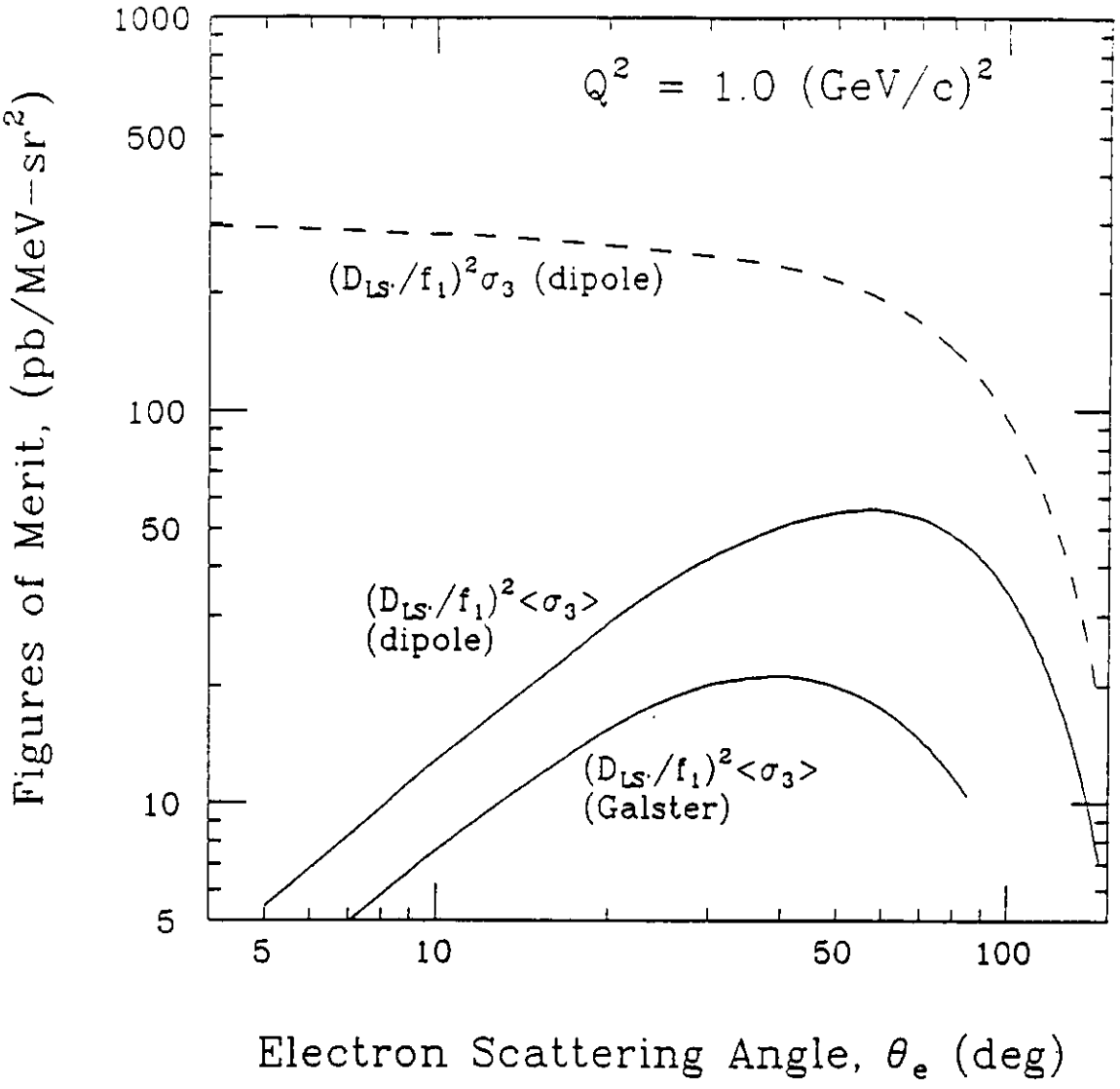

Fig. 22 Figure-of-Merit (FOM) for the G_E^n Experiment at $Q^2 = 1.0\,(\mathrm{GeV/c})^2$. Note the fundamental difference between using the averaged cross section and using the "point" cross section: FOM($\langle\sigma_3\rangle$) maximizes at relatively large electron scattering angles while FOM(σ_3) at $\theta_e \rightarrow 0$.

Table XI. Counting Rates, Data Acquisition Times, and Uncertainties with an Effective Luminosity $L_{eff} = 2.8 \times 10^{38}$ cm^{-2}s^{-1}

Q^2 (GeV/c)^2	θ_e (deg)	E (GeV)	Case*	R (min^{-1})	A (min^{-1})	$r \equiv R/A$	N * ($\times 10^5$)	ξ ($\times 10^{-2}$)	$\Delta\xi$ ($\times 10^{-2}$)	T ⊗ (hr)	ΔG_E^n ‡ ($\times 10^{-2}$)	$\Delta G_E^n / G_E^n$ ‡
2.0	46.6	2.4	I	1.71	0.060	29	0.82	0	0.36	800	0.56	–
			II	2.33	0.080	29	1.12	3.48	0.31		1.39	0.19
			III	1.76	0.060	29	0.85	1.11	0.35		0.59	0.33
1.5	65.5	1.6	I	2.06	0.15	24	0.62	0	0.43	500	0.68	–
			II	2.93	0.15	26	0.74	4.46	0.39		1.09	0.13
			III	2.09	0.15	24	0.63	1.55	0.43		0.71	0.28
1.0	45.0	1.6	I	5.30	0.684	7.6	1.59	0	0.28	500	0.56	–
			II	6.26	0.876	7.1	1.88	3.94	0.26		0.92	0.099
			III	5.46	0.684	8.0	1.64	1.77	0.28		0.60	0.16
0.50	65.5	0.8	I	14.2	1.53	9.3	2.12	0	0.24	250	0.52	–
			II	15.2	1.72	8.8	2.28	3.97	0.23		0.63	0.068
			III	14.5	1.53	9.5	2.17	2.32	0.24		0.55	0.11
0.30	45.0	0.80	I	34.0	5.12	6.6	3.06	0	0.21	150	0.56	–
			II	36.1	5.39	6.7	3.25	2.76	0.20		0.88	0.082
			III	34.9	5.12	6.8	3.15	1.93	0.20		0.71	0.11

* Case I: $G_E^n = 0$; Case II: $G_E^n = -\tau G_M^n$; Case III: $G_E^n = -\tau G_M^n (1 + 5.6\tau)^{-1}$

* $N = \frac{1+2/\tau}{(A_y \Delta P_{y'})^2}$ with A_y given in Table VIII

⊗ $T(\text{hr}) = \frac{N}{60R(\text{min}^{-1})}$

‡ Statistical only

Table XII. Experimental Conditions [$Q^2 = 1.0$ (GeV/c)^2]

1. Electron Beam	
1.1 Energy, E (GeV)	1.6
1.2 Polarization, P_L	0.40
1.3 Current, I (μA)	100
1.4 Incident electron flux, $F(10^{14}$ e/s)	6.25
1.5 Duty factor	1.0
2. Liquid Deuterium Target Cell	
2.1 LD_2 thickness, $\rho\, x$ (g/cm^2) [=(0.168 g/cm^3) (5.0 cm)]	0.84
2.2 Effective LD_2 thickness seen by HMS, x_{eff} (cm)	4.4
2.3 Area density of LD_2 nuclei, $\rho_n\, x$ (deuts/cm^2)	5.06×10^{23}
2.4 Effective LD_2 areal density, $\rho_n\, x_{eff}$ (deuts/cm^2)	4.4×10^{23}
2.5 Cell wall thickness, x (mils)	8
2.5.1 Exit window, x_2 (mils Al)	5
2.5.2 Entrance window, x_1 (mils Al)	3
2.5.3 Exit + Entrance windows, x (mils Al)	8
$\rho\, x$ (g/cm^2 ^{27}Al)= (2.70 g/cm^3)(2.03 $\times 10^{-3}$)	5.5×10^{-3}
$\rho_n\, x$ (^{27}Al/cm^2)	1.2×10^{21}
2.6 Power dissipation, P (Watts)	230
3. Luminosity $F\,\rho_n\, x = L$ (cm^{-2} s^{-1})	
3.1 Luminosity for deuterium, L_2 (cm^{-2} s^{-1})	3.2×10^{38}
3.2 Effective Luminosity for Coincidences, L_{e-n}	2.8×10^{38}
3.3 Luminosity for empty cell, L_{27} (cm^{-2} s^{-1})	7.6×10^{35}

(continued on next page)

Table XII. Cont'd

4. Neutron Polarimeter	
4.1 Height of analyzer detectors, h (m)	0.254
4.2 Width of analyzer detectors, w (m)	1.016
4.3 Mean flight path, x (m)	9.70
4.4 Horizontal angular acceptance, $\Delta\theta_n$	$\pm$52.4 mr = $\pm$3.00°
4.5 Vertical angular acceptance, $\Delta\phi_n^{\mathrm{v}}$	$\pm$ 13.2 mr = $\pm$0.754°
4.6 Solid angle, $\Delta\Omega_n$ (msr)	2.75
4.7 Efficiency, ϵ (%)	0.12
4.8 Average analyzing power, $\overline{A_y}$	0.34
4.9 Neutron transmission through Pb-Fe shielding, t	0.39
5. Electron Spectrometer	
5.1 Horizontal angular acceptance, $\Delta\theta_e$	$\pm$ 59.3 mr = $\pm$ 3.40°
5.2 Vertical angular acceptance, $\Delta\phi_e^{\mathrm{v}}$	$\pm$ 14.0 mr = $\pm$ 0.801°
5.3 Solid angle, $\Delta\Omega_e$ (msr)	1.67
5.4 Momentum acceptance, $\Delta p_e/pe$ (%)	$\pm$ 4.4
5.5 Momentum bite, $\Delta p_e = \pm 0.040\, p_e$ (MeV/c)	$\pm$ 43
5.6 Efficiency for a "good" electron, ϵ_{wc}	$\sim$ 0.97
5.7 Live time fraction in wire chambers, l_{wc}	$\sim$ 0.95
5.8 Radiative correction factor, ϵ_{rad}	0.83
6. Data Acquisition System	
6.1 Live time fraction, l	0.95

4.11 Electron Scattering Angle For Maximum Figure – of – Merit

For convenience in this section, we denote the triple differential cross section as s_3, which will be identified later as either the cross section $\langle\sigma_3\rangle$ averaged over the detector acceptances or the "point" cross section σ_3 depending on the definition of the figure-of-merit (FOM).

• Variation of cross section and its effect on the FOM

The FOM can be expressed generally as

$$\mathrm{FOM} = \left(\frac{D_{LS'}}{f_1}\right)^2 s_3 \tag{58}$$

following Eq. (33) in Section 4.3. The variation of this FOM as a function of the electron scattering angle θ_e is determined by:

$$\frac{d\mathrm{FOM}}{d\theta_e} = s_3 \frac{d(D^2_{LS'}/f_1^2)}{d\theta_e} + \frac{D^2_{LS'}}{f_1^2}\frac{ds_3}{d\theta_e} \tag{59}$$

This FOM will have a maximum at a nonvanishing θ_e only if $d\mathrm{FOM}/d\theta_e = 0$ can be satisfied. We know that the slope $ds_3/d\theta_e$ of the cross section is always negative because the cross section falls when the electron scattering angle θ_e increases. Also we know from the slope of the curves in Fig. 12 that the term $d(D^2_{LS'}/f_1^2)/d\theta_e$ vanishes at relatively large angles. In view of these two facts, the slope $d\,\mathrm{FOM}/d\theta_e$ will always be negative when the slope of the cross section is so large that

$$\frac{D^2_{LS'}}{f_1^2}\left|\frac{ds_3}{d\theta_e}\right| > s_3 \frac{d(D^2_{LS'}/f_1^2)}{d\theta_e} \tag{60}$$

is satisfied in the whole region of θ_e; that is, the FOM maximizes at zero electron scattering angle if the above inequality holds. On the other hand, if the cross section varies slowly with θ_e so that

$$\frac{D^2_{LS'}}{f_1^2}\left|\frac{ds_3}{d\theta_e}\right| \sim s_3 \frac{d(D^2_{LS'}/f_1^2)}{d\theta_e} \tag{61}$$

for finite θ_e, then it is likely that $d\,\mathrm{FOM}/d\theta_e = 0$ can be reached at a certain nonvanishing θ_e. In the extreme case where the cross section is a constant, we

would have

$$\frac{d\mathrm{FOM}}{d\theta_e} = s_3 \frac{d(D^2_{LS'}/f_1^2)}{d\theta_e} \qquad (\text{if } s_3 = \text{const.}). \tag{62}$$

In this extreme case, the electron scattering angle θ_e that corresponds to the maximum of the FOM would be the same as that for the maximum of the term $(D_{LS'}/f_1)^2$, which always exists as shown in Section 4.3. This extreme case indicates that the smaller the value of $ds_3/d\theta_e$ (or the slower the variation of s_3 with respect to θ_e), the closer the maximum of the FOM will be with respect to the maximum of $D^2_{LS'}/f_1^2$, which is always at a relatively large electron angle.

Now, an averaged cross section $\langle\sigma_3\rangle$ is used for s_3 in the definition of the FOM for our experiment because of the finite acceptances of the detectors, while a "point" cross section σ_3 is used for s_3 in a more cavalier definition of the FOM. In order to compare the difference between these two definitions of the FOM, we show for $Q^2 = 1.0$ (GeV/c)^2 the averaged and the "point" cross sections in Fig. 23 and their derivatives in Fig. 24 as a function of θ_e. It is clear that the "point" cross section has a much steeper variation with θ_e; we discuss below the reason for this sharp reduction in the steepness of the averaged cross section. In Figs. 25 and 26, we plot the derivatives $d\,\mathrm{FOM}/d\theta_e$ with the contributions from $s_3\, d(D^2_{LS'}/f_1^2)/d\theta_e$ and $(D^2_{LS'}/f_1^2)(ds_3/d\theta_e)$ for $s_3 = \langle\sigma_3\rangle$ (the averaged cross section) and $s_3 = \sigma_3$ (the "point" cross section), respectively. These figures show clearly that the derivative $d\,\mathrm{FOM}/d\theta_e$ with the averaged cross section passes through zero at a relatively large θ_e, while it is always negative with the "point" cross section. The conclusion is that averaging the cross section makes a substantial reduction in the steepness of the cross section, which in turn results in a maximum FOM at a relatively large electron scattering angle, while the unaveraged cross section gives a maximum FOM in the most forward directions.

•Recoil momentum distribution and its effect on the averaging process of the cross section

The change of the steepness of the triple differential cross section as a result of

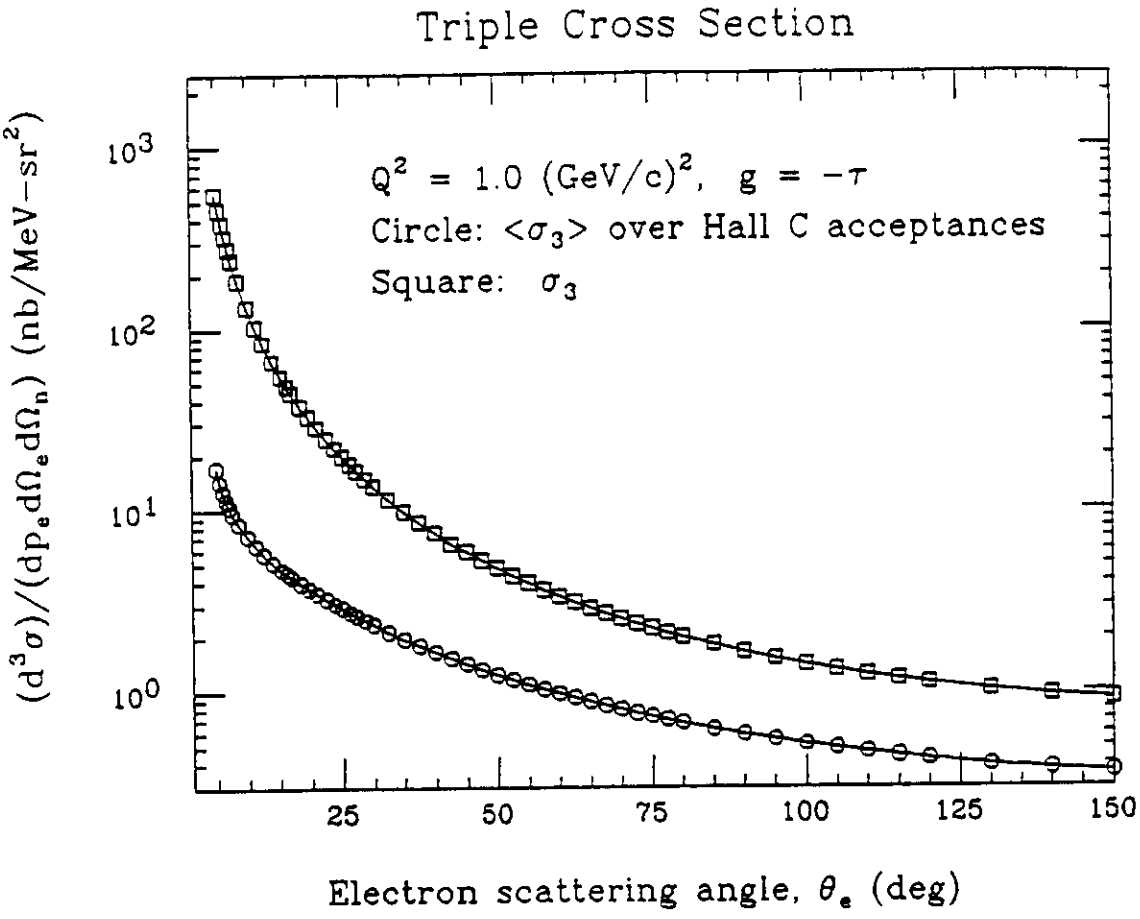

Fig. 23 The Averaged and the "Point" Triple Differential Cross Sections for $Q^2 = 1.0$ (GeV/c)^2 in the Dipole Parameterization.

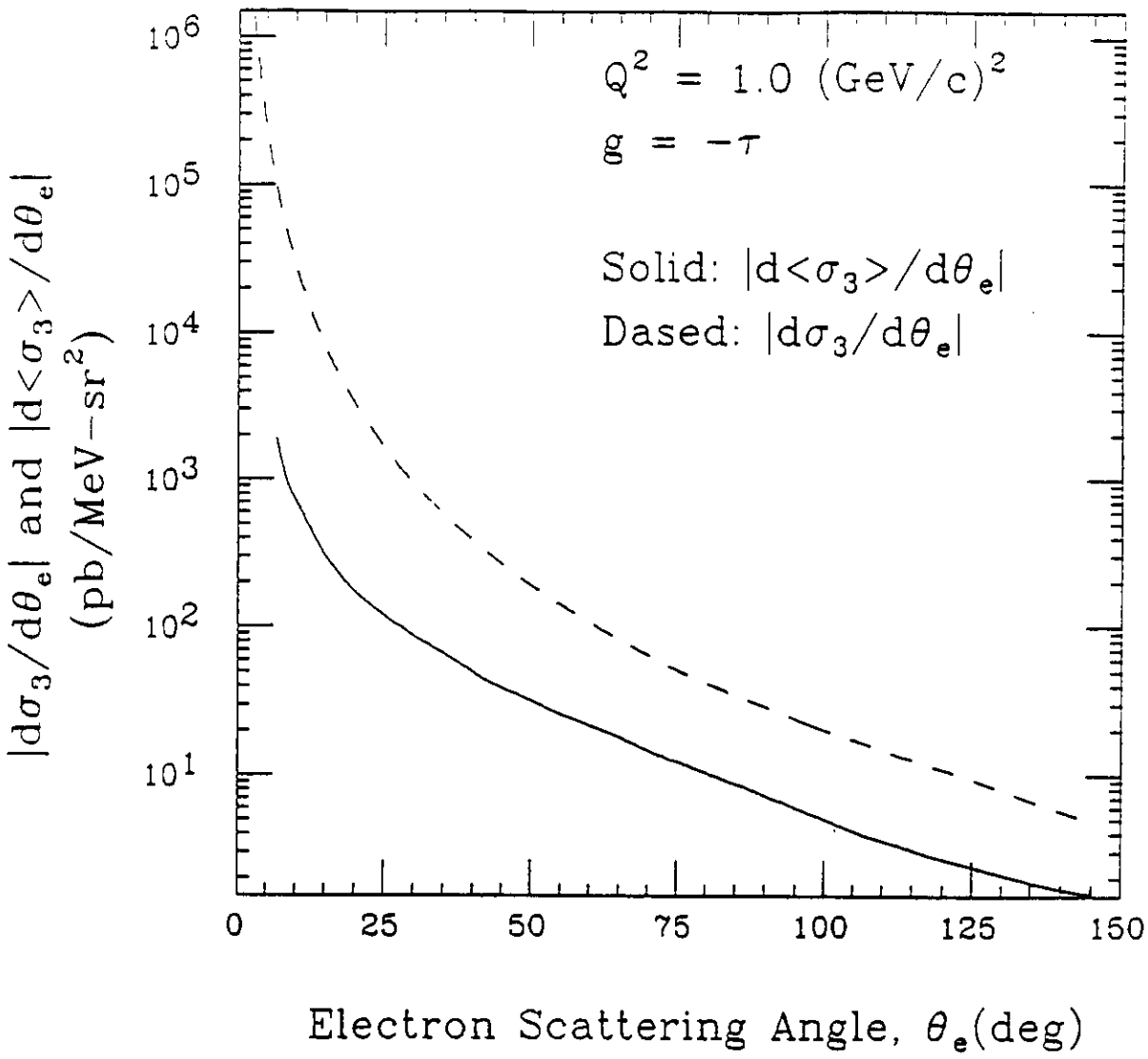

Fig. 24 Slope of the Averaged and the "Point" Triple Differential Cross Sections as a Function of Electron Scattering Angle θ_e. The large difference between the two is responsible for the fundamental difference in the maximum FOM in the two cases as shown in Fig. 22.

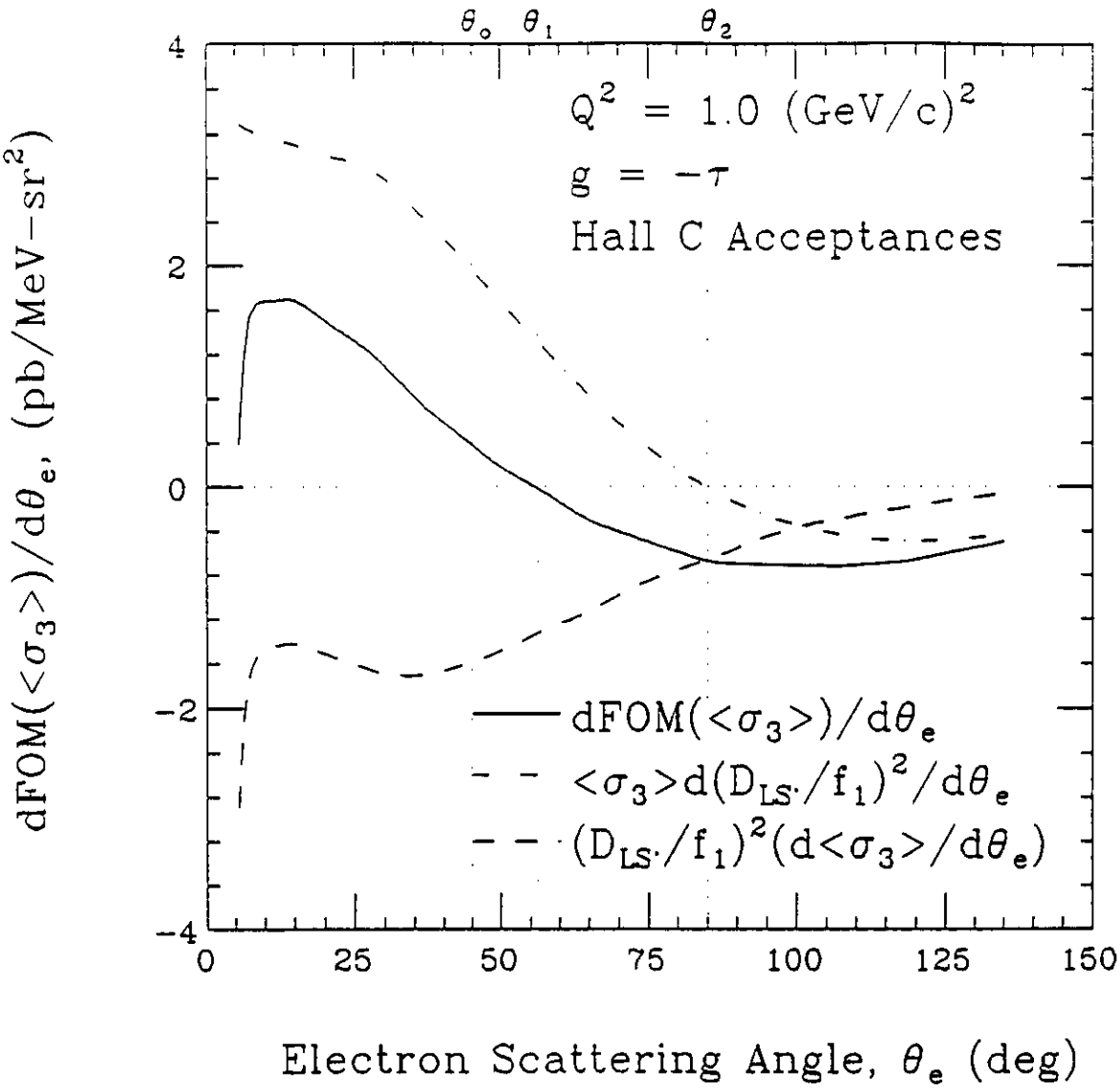

Fig. 25 $d\text{FOM}(\langle\sigma_3\rangle)/d\theta_e$ in the Dipole Parameterization. Note that it passes through zero at a relatively large electron scattering angle $\theta_e = \theta_1$, which is to be compared with Fig. 26 where $d\text{FOM}(\sigma_3)/d\theta_e$ is always negative. In this figure, θ_2 is the electron angle for minimum statistical uncertainty, and θ_o is the designed experimental angle.

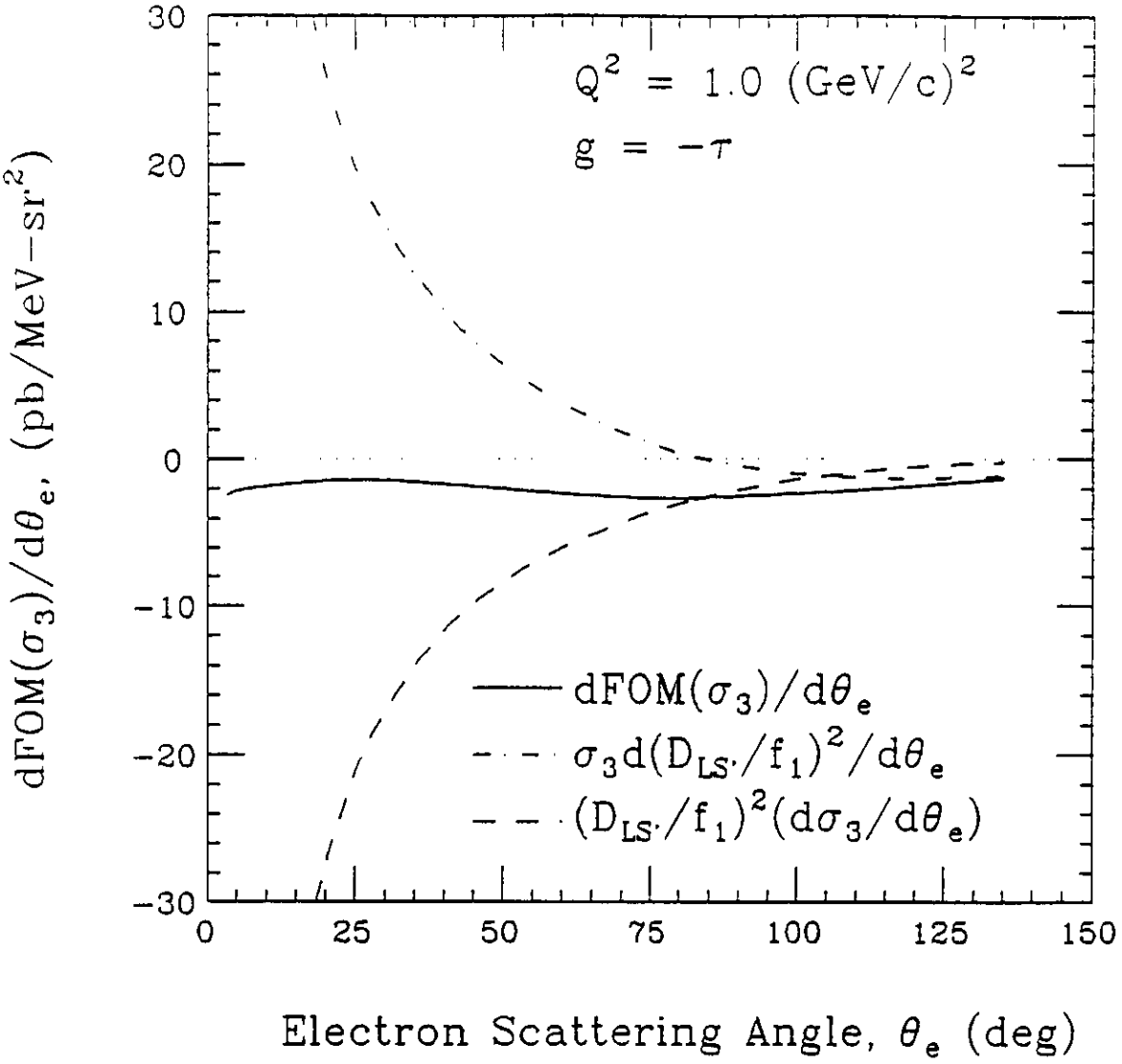

Fig. 26 $d\text{FOM}(\sigma_3)/d\theta_e$ in the Dipole Parameterization. Because of the dominating contribution from the term $(D_{LS'}/f_1)^2(d\sigma_3/d\theta_e)$ (< 0), $d\text{FOM}(\sigma_3)/d\theta_e$ is always negative, leading to a maximum FOM in forward directions.

averaging process can be understood in terms of the recoil momentum distribution. For quasielastic scattering, we know that the triple differential cross section is proportional to the recoil momentum distribution $|\phi(p_r)|^2$:

$$s_3(p_r) \propto |\phi(p_r)|^2 \tag{63}$$

where p_r is the recoil momentum. For the deuteron, $|\phi(p_r)|^2$ drops rapidly as p_r increases; *e.g.*, $|\phi(p_r = 100\,\mathrm{Mev/c})|^2 \sim 3 \times 10^{-2}|\phi(p_r = 0)|^2$. For $Q^2 = 1.0$ $(\mathrm{GeV/c})^2$ at different electron scattering angles, we use MCEEP to obtain the normalized probablility distribution $P_i(p_r^i)$ of the recoil momentum with the detector acceptances as designed; that is,

$$P_i(p_r^i) = \frac{N_i(p_r^i \pm \Delta p_r^i)}{N}, \tag{64}$$

where $N_i(p_r^i \pm \Delta p_r^i)$ is the number of events in the $\mathrm{i^{th}}$ bin generated with the recoil momemtum p_r between p_r^i and $p_r^i \pm \Delta p_r^i$, and $N = \Sigma_i N_i$ is the total number of events generated to obtain the averaged triple cross section $\langle\sigma_3\rangle$ for a given θ_e. It should be noted that the probability distribution thus defined is equivalent to $P_i(p_r^i) = \int_{p_r^i-\Delta p_r^i}^{p_r^i+\Delta p_r^i} |\phi(p_r)|^2 p_r^2 dp_r / \int |\phi(p_r)|^2 p_r^2 dp_r$. Shown in Fig. 27 are these distributions for $Q^2 = 1.0$ $(\mathrm{GeV/c})^2$ as a function of p_r for beam energies of 1.6, 2.4, 3.2, and 4.0 GeV, which correspond to the electron scattering angles of 45, 27, 20, and 15 degrees. This figure demonstrates clearly that the distribution is much wider at smaller electron scattering angles than at larger electron scattering angles. This fact means that we are averaging over a much larger recoil momentum region at smaller θ_e than at larger θ_e. Because the cross section drops rapidly when p_r increases, the averaged cross section $\langle\sigma_3\rangle$ is reduced from the "point" (unaveraged) cross section σ_3 (which has $p_r \to 0$) much more drastically at smaller angles than at larger angles, which results in a much slower variation of $\langle\sigma_3\rangle$ with θ_e; furthermore, this tendency to flatten $\langle\sigma_3\rangle$ causes the FOM to have a maximum value at a relatively large scattering angle θ_e as shown above.

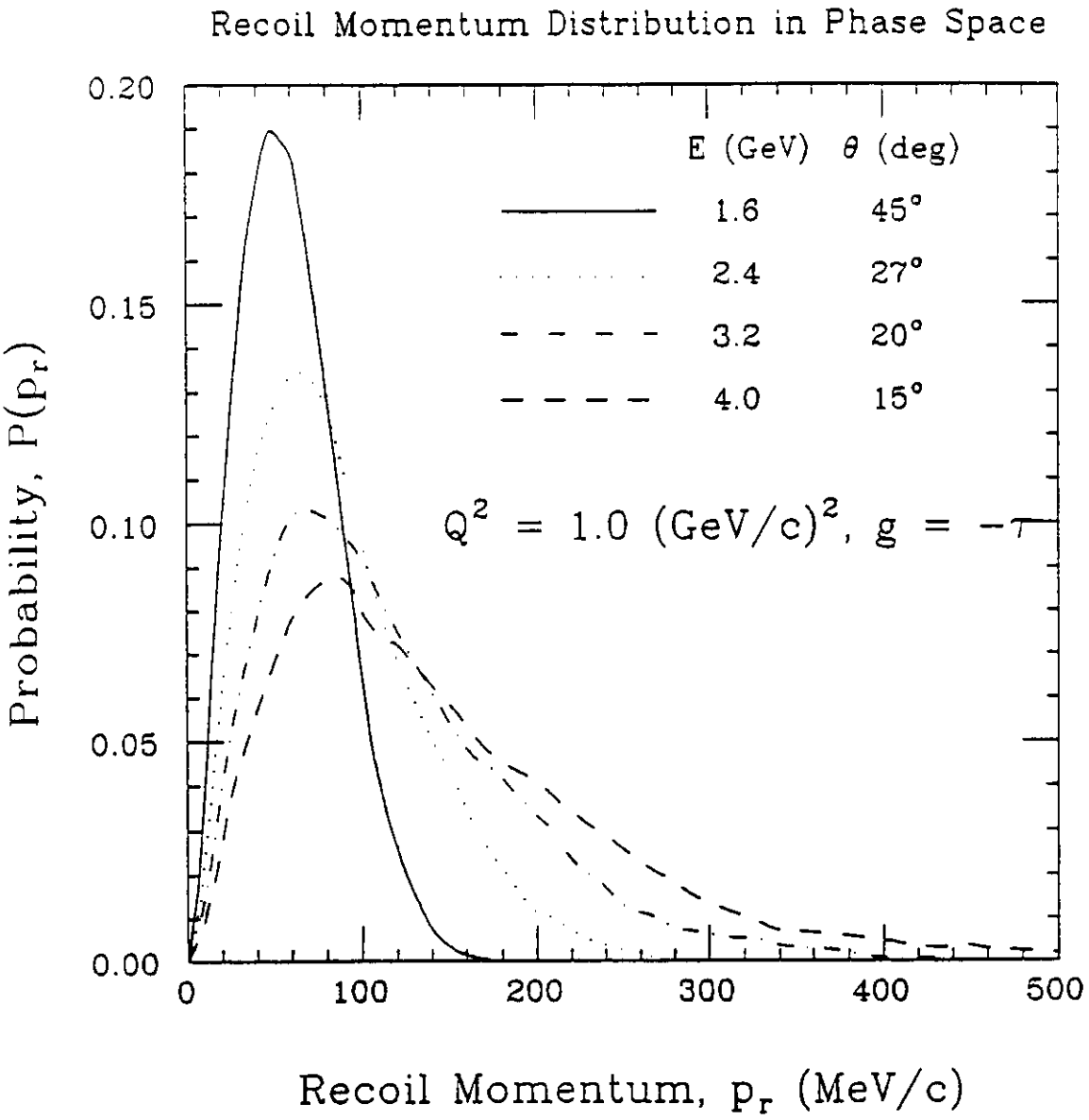

Fig. 27 Probability Distribution of the Recoil Momentum p_r for $Q^2 = 1.0$ $(GeV/c)^2$. The spectrum at smaller electron scattering angle is much wider than that at larger electron scattering angle. This fact results in the reduction of slope of $\langle\sigma_3\rangle$ in comparison with that of σ_3.

The conclusions to be drawn from this study are obvious. In general, coincidence experiments such as ours should be designed with the coincidence differential cross sections *averaged* over the acceptances of the detectors involved. The unaveraged cross sections may result in different results that do not reflect reality. The results indicate that we want to do this particular experiment at relatively large electron scattering angles not only because the kinematic conditions can be optimized there, but also because the probability of having large recoil momentum is minimized at large electron angles, which is desired for quasielastic scattering.

4.12 Accidental Counting Rates

In Bates experiment 85–05, we measured the single-arm counting rates and the accidental coincidence rates as a function of average beam current. The observed singles rates N_e and N_n of electrons and neutrons, respectively, and the observed accidental electron–neutron coincidence rates A are listed in Table XIII as a function of the average beam current I, which we varied over the range from 0.22 to 1.85 μA. The electron-neutron accidental rate A was obtained by multiplying the number of coincidence triggers observed within the 120-ns time-of-flight window by the ratio of the observed coincidence resolving time τ(= 2 ns fwhm) to the duration τ_w(= 120 ns) of the time-of-flight window; that is,

$$A \simeq (\text{Coincidence Triggers in } \tau_w)(\frac{\tau}{\tau_w}) \tag{65}$$

Because the number of true coincidence events is a negligible fraction of the total number of observed coincidence triggers, we obtain a good measure of the accidental rate beneath the time-of-flight peak.

Figure 28 is a plot of the electron–neutron accidental coincidence rate versus the average beam current for Bates E85–05 (with $\theta_e = 37°$, $\theta_n = 57°$, and $E = 868$ MeV). The solid line is the observed rate; the dashed line is the expected rate, which agrees with the observed rate. The expected rate is calculated from the formula $A = \tau N_e N_n / f$ with $f = 0.008$, $\tau = 2.0$ ns, and the measured counting rates N_e and N_n in the electron and neutron arms.

Table XIII. Single-Arm and Accidental Coincidence Rates vs Average Beam Current in Bates E85-05

	Single-Arm Rates		Accidental Coincidence Rates	
Average Beam Current $I(\mu A)$	Electron Rate $N_e(s^{-1})$	Neutron Rate $N_n(s^{-1})$	Observed Rate $A(s^{-1})$	Estimated Rate $A(s^{-1})$
0.22	21.6	441	0.002	0.004
0.55	79.8	1056	0.017	0.02
0.95	182.4	1722	0.06	0.08
1.03	229.2	1872	0.09	0.13
1.35	334.8	2324	0.16	0.23
1.85	503.4	3078	0.31	0.39

To estimate the accidental coincidence counting rates A^C expected at CEBAF, we scale our results from the accidental rates A^B observed at Bates E85–05:

$$\frac{A^C}{A^B} = \frac{\tau^C N_e^C N_n^C f^B}{\tau^B N_e^B N_n^B f^C}. \tag{66}$$

The electron and neutron singles rates N_e and N_n are given by the following expression:

$$N_e = L \frac{d^2\sigma(\theta_e, p_e)}{d\Omega_e dp_e} \Delta\Omega_e \, \Delta p_e \, \epsilon, \tag{67}$$

$$N_n = L \frac{d\sigma_n(\theta_n, E_{th} < E_n < E_{max})}{d\Omega_n} \Delta\Omega_n \, \epsilon. \tag{68}$$

The double-differential cross section for electrons, $d^2\sigma/(d\Omega_e dp_e)$, is obtained from the MONQEE code by Dytmann[18] (1987) based on the equations of Moniz[19] (1969); the energy–integrated cross section for neutrons, $d\sigma/d\Omega$, is obtained from the electroproduction code (EPC) of O'Connell and Lightbody[20] (1988). The results are listed in columns five and six of Table IX. In Eq. (68), ϵ is the neutron detection efficiency averaged over the neutron energy interval $E_{th} < E_n < E_{max}$.

For software thresholds of 4 MeVee (= 8.4 MeV proton energy) on the front detectors and 10 MeVee (= 16.6 MeV proton energy) on the rear detectors, the neutron energy threshold E_{th} = 25 MeV (=17 MeVee). The notation MeVee denotes MeV of electron equivalent energy.

In view of Eqs. (67) and (68), Eq. (66) can be written as

$$\frac{A^C}{A^B} = \frac{\tau^C}{\tau^B}\frac{f^B}{f^C}\frac{(L^C)^2[d^2\sigma^C/(d\Omega_e dp_e)]\Delta\Omega_e^C \Delta p_e^C (d\sigma^C/d\Omega_n)\Delta\Omega_n^C}{(L^B)^2[d^2\sigma^B/(d\Omega_e dp_e)]\Delta\Omega_e^B \Delta p_e^B (d\sigma^B/d\Omega_n)\Delta\Omega_n^B}\frac{\epsilon^C}{\epsilon^B}. \qquad (69)$$

The numerical values of the quantities in Eq. (69) are listed in Table XIV.

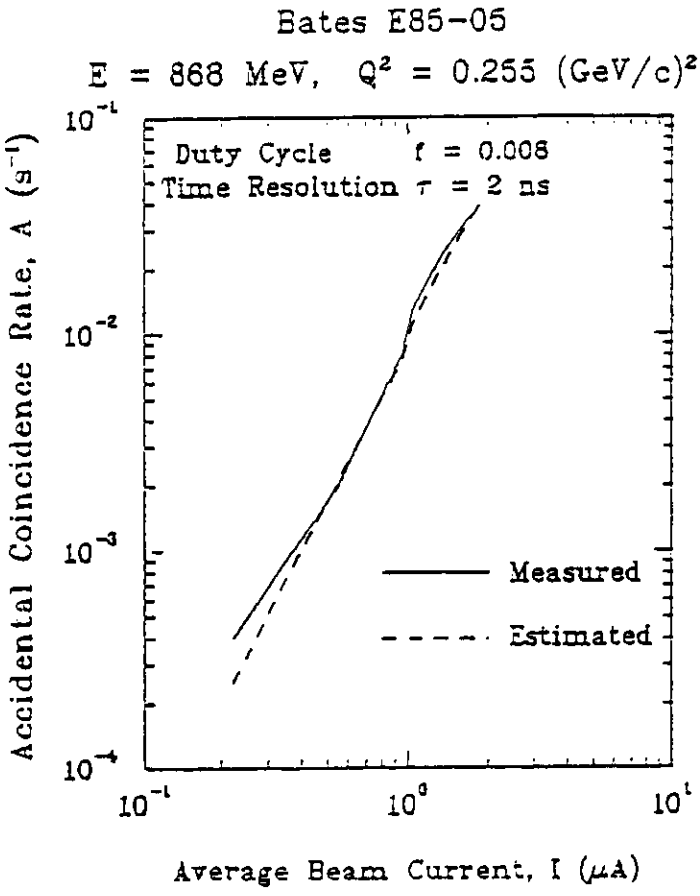

Fig. 28 Accidental Coincidence Rate versus the Average Beam Current for Bates E85-05.

Table XIV. Accidental Coincidence Rates Expected at CEBAF for Hall C HMS

Quantities	Bates E85-05	CEBAF E89-05					
Q^2(GeV/c)^2	0.255	0.25	0.30	0.50	1.0	1.5	2.0
θ_e(deg)	37.0	40.1	45.0	65.5	45.0	65.5	100.
E(GeV)	0.868	0.8	0.8	0.8	1.6	1.6	2.4
τ(ns) (fwhm)	2.0	0.70	0.70	0.70	0.70	0.70	0.70
f	0.008	1.0	1.0	1.0	1.0	1.0	1.0
$L(10^{36}\text{cm}^{-2}\text{s}^{-1})$	2.6	320	320	320	320	320	320
$d^2\sigma_e/(d\Omega_e dp_e)$	5.4	I*:	2.35	0.30	0.068	0.0086	0.0014
$(10^{-33}\text{cm}^2/\text{sr/MeV/c})$		II*: 4.8	2.40	0.32	0.074	0.0073	0.0019
$\Delta\Omega_e$(msr)	5.6	2.42	2.78	4.42	3.34	5.69	4.13
$2\Delta p_e$ (MeV/c)	64.3	53	51	43	85	54	43
$d\sigma/d\Omega_n$	715	I*:	847	1497	2044	2843	3058
$(10^{-33}\text{cm}^2/\text{sr})$		II*: 724	874	1576	2405	3306	5078
$\Delta\Omega_n$(msr)	9.68	2.74	2.74	2.74	2.74	2.74	2.74
ϵ^C/ϵ^B	–	1.0	0.99	0.99	0.96	0.93	0.96
A^C/A^B	–	I*:	2.44	0.728	0.326	0.0719	0.0151
		II*: 0.486	2.57	0.817	0.418	0.0710	0.0340
$A(\text{s}^{-1})$	0.035	I*:	0.0853	0.0255	0.0114	0.0025	0.00051
		II*: 0.017	0.0898	0.0286	0.0146	0.0025	0.0012
$R(\text{s}^{-1})$	–	I*:	0.67	0.28	0.10	0.040	0.036
		II*: 0.41	0.69	0.29	0.12	0.047	0.044
R/A	–	I*:	7.8	11	9.1	16	34
		II*: 17	7.6	10	8.2	19	33

* I: Galster parameterizaton; II: Dipole parameterization.

4.13 Projected Uncertainties ΔG_E^n in G_E^n

The number of events N needed to measure the asymmetry ξ with a specified uncertainty $\Delta\xi$ is given by Eq. (31). Values of N, together with the associated asymmetry uncertainties $\Delta\xi$, are listed in Table X for the five Q^2 points proposed here.

The relative uncertainty in the ratio $g \equiv G_E^n/G_M^n$ is given by Eq. (16) with f_1 defined by Eq. (12) and f_2 defined by Eqs. (17), (18), and (19). In Table XV, we compare the statistical uncertainties (expected in the data acquisition times given in Table X) with the scale uncetainties in both $D_{LS'}$ and g, where a scale uncrtainty of $(\Delta D_{LS'}/D_{LS'})_{scale} = 0.060$ is assumed. In Bates E85-05, we achieved a $(\Delta D_{LS'}/D_{LS'})_{scale} = 0.070$. Also listed in Table XV is the relative systematic uncertainty $(\Delta g/g)_{syst}$ from Eq. (27) and the total projected uncertainty $(\Delta g/g)_{total}$.

Table XV. Projected Uncertainties in $D_{LS'}$ and g with $(\Delta D_{LS'}/D_{LS'})_{scale} = 0.060$

Q^2 (GeV/c)^2	E (GeV)	θ_e (deg)	case	$(\Delta D_{LS'}/D_{LS'})_{stat}$	$(\Delta g/g)_{stat}$	$(\Delta g/g)_{scale}$	$(\Delta g/g)_{syst}$	$(\Delta g/g)_{total}$
2.0	2.4	46.6	D*	0.083	0.175	0.127	0.055	0.223
			G*	0.295	0.307	0.063	0.010	0.313
1.5	1.6	65.6	D*	0.081	0.121	0.089	0.006	0.150
			G*	0.256	0.264	0.062	0.014	0.272
1.0	1.6	45.0	D*	0.061	0.091	0.089	0.021	0.129
			G*	0.144	0.153	0.064	0.007	0.165
0.50	0.8	65.7	D*	0.054	0.063	0.069	0.023	0.096
			G*	0.094	0.099	0.063	0.027	0.120
0.30	0.8	45.1	D*	0.067	0.076	0.068	0.008	0.102
			G*	0.097	0.102	0.064	0.013	0.121

* D: for dipole parameterization; G: for Galster paremeterization.

From Table XV, note that the relative scale uncertainties are smaller than the

projected statistical uncertainties for the Galster parameterization; whereas for the dipole parameterization, the scale uncertainties are comparable to the statistical uncertainties. Also the relative systematic uncerntainty is always small.

Now we evaluate the uncertainties ΔG_E^n for the cases of $G_E^n = 0$, the dipole parameterization $G_E^n = -\tau G_M^n$, and the Galster parameterization $G_E^n = -\tau G_M^n (1.0 + 5.6\tau)^{-1}$.

• Case I : For $G_E^n = 0$, $\Delta G_E^n = G_M^n \Delta g$

For the case $G_E^n = 0$ (and thus $D_{LS'} = 0$, and $f_1 = 1$), the evaluation of the uncertainty Δg in Eq. (16) simplifies because multiplication of both sides of Eq. (16) by g causes all the terms to vanish except for the term with $\Delta\xi$ [note $(\Delta D_{LS'}/D_{LS'})^2 = (\Delta\xi/\xi)^2 + (\Delta A_y/A_y)^2 + (\Delta P_L/P_L)^2$]:

$$\Delta g = g\left(\frac{\Delta\xi}{\xi}\right) = \frac{B(\theta_e)}{A(\theta_e)}\frac{\Delta\xi}{P_L A_y} = \frac{B}{A}\frac{\sqrt{(1+2/\tau)/N}}{P_L A_y}. \tag{70}$$

The right-hand-members in the above equation follow from Eq. (31) and the fact that

$$\lim_{g\to 0}\ \xi = -g\,\frac{A(\theta_e)}{B(\theta_e)}\,P_L A_y, \tag{71}$$

For each of the five proposed Q^2 points, we list in Table XVI the value of the ratio of $B(\theta_e)/A(\theta_e)$, the uncertainties Δg in the ratio $g \equiv G_E^n/G_M^n$ for $P_L = 0.40$, and the corresponding uncertainties $\Delta\xi$ and ΔG_E^n. The expected uncertainties ΔG_E^n assume values of the magnetic form factor G_M^n based on the dipole parameterization

$$G_M^n = -\frac{1.91}{(1 + Q^2/0.71)^2}. \tag{72}$$

The expected uncertainties ΔG_E^n listed in Table XVI are typically about ± 0.005 and less than ± 0.007 for the five points at $Q^2 = 0.3$, 0.5, 1.0, 1.5 and 2.0 $(\mathrm{GeV/c})^2$.

• Case II : For $G_E^n = -\tau G_M^n$ with $G_M^n = -1.91/(1 + Q^2/0.71)^2$

For this dipole parameterization, the projected statistical uncertainty in G_E^n can be calculated:

$$\left(\frac{\Delta G_E^n}{G_E^n}\right)_{stat} = \left(\frac{\Delta g}{g}\right)_{stat} = f_1 \frac{\Delta \xi}{\xi}. \tag{73}$$

Because $G_E^n = gG_M^n$, the total uncertainty in G_E^n can be calculated:

$$\frac{\Delta G_E^n}{G_E^n} = \left[\left(\frac{\Delta g}{g}\right)^2 + \left(\frac{\Delta G_M^n}{G_M^n}\right)^2\right]^{1/2}, \tag{74}$$

where the total relative uncertainty $\Delta g/g$ in g is calculated from Eq. (16) [or Eq. (24) with Eqs. (25), (26) and (27)].

In Table XVII, the values of the statistical and the total uncertainties in G_E^n with the associated values of $\Delta\xi$ from Eq. (31) and $\Delta P_{S'}$ from $(\Delta P_{S'}/P_{S'})^2 = (\Delta\xi/\xi)^2 + (\Delta A_y/A_y)^2$ are listed for the five Q^2 points proposed here. The total uncertainties in Table XVII assume a relative uncertainty $\Delta G_M^n/G_M^n = 0.025$, which is the goal of new measurements. For this dipole parameterization of G_E^n, the projected statistical uncertainties ΔG_E^n are plotted with the dashed curve in Fig. 29.

It should be pointed out that the total uncertainty in G_E^n depends on the uncertainties in A_y, P_L, and G_M^n in addition to the uncertainty in ξ. Also, we used a combined scale uncertainty $(\Delta D_{LS'}/D_{LS'})_{scale} = 0.060$. Measurements on A_y and P_L are expected to result in comparable (or better) precision.

• Case III : For $G_E^n = -\tau G_M^n(1 + 5.6\tau)^{-1}$ with $G_M^n = -1.91/(1 + Q^2/0.71)^2$

The calculation is exactly the same as in the dipole case except that we replace $g \equiv G_E^n/G_M^n = -\tau$ with $g = -\tau(1 + 5.6\tau)^{-1}$. We list the expected uncertainties $\Delta G_E^n/G_E^n$ and ΔG_E^n in Table XVIII, and plot the statistical uncertainties with the solid curve in Fig. 29.

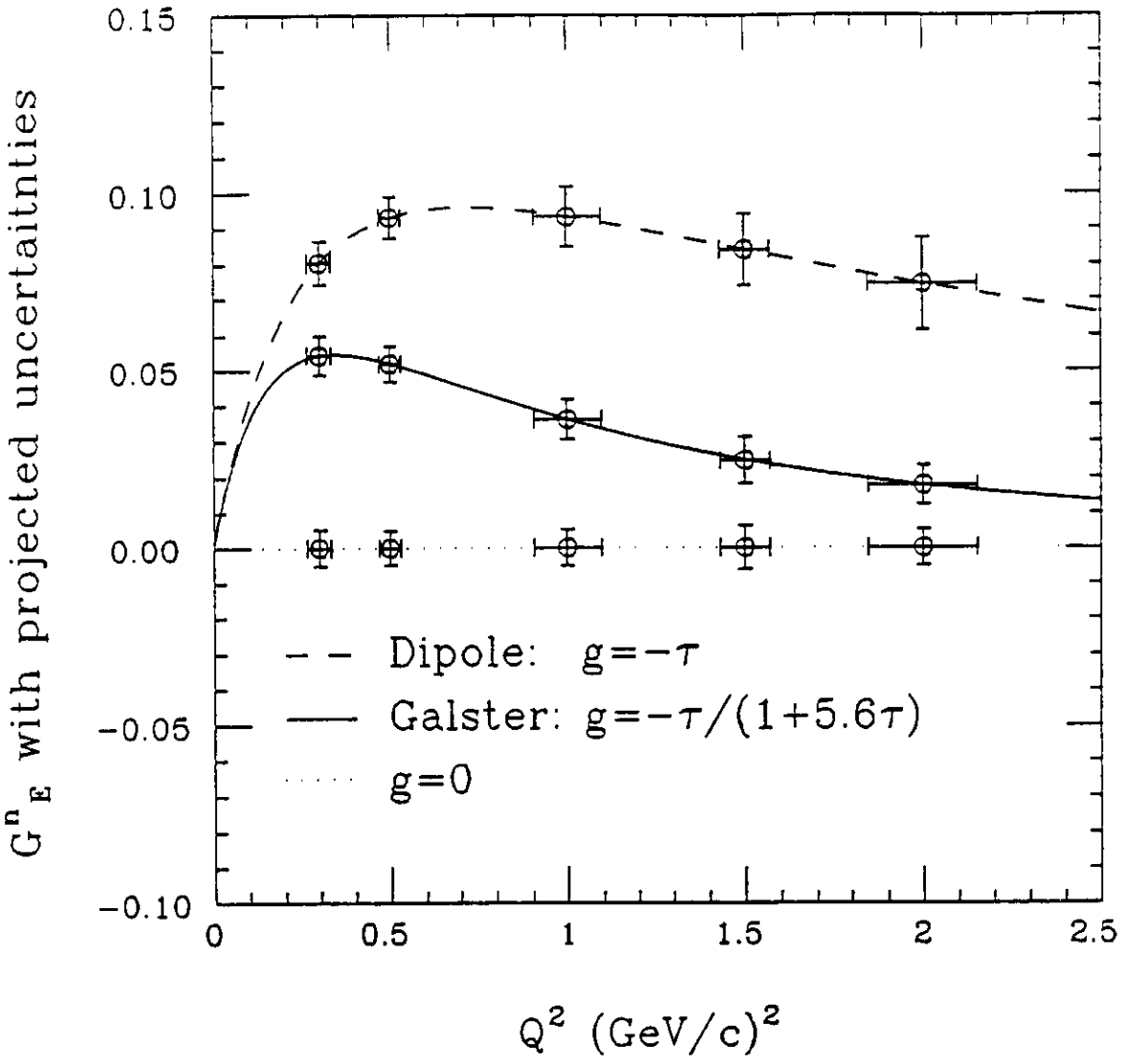

Fig. 29 G_E^n with Projected Statistical Uncertainties $(\Delta G_E^n)_{stat}$ in the Dipole (dashed), the Gaster (solid), and $G_E^n = 0$ (dotted) Parameterizations.

Table XVI. Uncertainties ΔG_E^n if $G_E^n = 0$ (Case I)

Q^2 (GeV/c)^2	E (GeV)	θ_e (deg)	B/A	Δg	ΔG_E^n	$\Delta\xi$
2.0	2.4	46.6	1.104	0.0398	0.0052	0.0033
1.5	1.6	65.6	0.925	0.0319	0.0063	0.0040
1.0	1.6	45.0	0.817	0.0156	0.0051	0.0026
0.50	0.8	65.7	0.532	0.0074	0.0048	0.0022
0.30	0.8	45.1	0.464	0.0055	0.0052	0.0019

Table XVII. Uncertainties ΔG_E^n if $G_E^n = -\tau G_M^n$ (Case II) and $\Delta G_M^n/G_M^n = 0.025$

Q^2 (GeV/c)^2	E (GeV)	θ_e (deg)	$(\Delta G_E^n/G_E^n)_{stat}$	$(\Delta G_E^n)_{stat}$	$\Delta\xi$	$(\Delta G_E^n/G_E^n)$	(ΔG_E^n)	$\Delta P_{S'}$
2.0	2.4	46.6	0.17	0.013	0.0029	0.22	0.017	0.013
1.5	1.6	65.6	0.12	0.010	0.0036	0.15	0.013	0.014
1.0	1.6	45.0	0.091	0.0085	0.0024	0.13	0.012	0.0081
0.50	0.8	65.7	0.063	0.0058	0.0022	0.10	0.0093	0.0063
0.30	0.8	45.1	0.076	0.0061	0.0018	0.10	0.0084	0.0052

Table XVIII. Uncertainties ΔG_E^n if $G_E^n = -\tau G_M^n(1+5.6\tau)^{-1}$ (Case III) and $\Delta G_M^n/G_M^n = 0.025$

Q^2 (GeV/c)^2	E (GeV)	θ_e (deg)	$(\Delta G_E^n/G_E^n)_{stat}$	$(\Delta G_E^n)_{stat}$	$\Delta\xi$	$(\Delta G_E^n/G_E^n)$	(ΔG_E^n)	$\Delta P_{S'}$
2.0	2.4	46.6	0.31	0.0055	0.0033	0.31	0.0056	0.014
1.5	1.6	65.6	0.26	0.0066	0.0040	0.27	0.0068	0.014
1.0	1.6	45.0	0.15	0.0055	0.0026	0.17	0.0060	0.0077
0.50	0.8	65.7	0.099	0.0051	0.0022	0.12	0.0064	0.0058
0.30	0.8	45.1	0.10	0.0056	0.0019	0.12	0.0067	0.0049

If the actual G_E^n does not follow any of the three cases studied here, we will observe a value of $P_{S'}$ that differs from those expected from the three models studied here. For the point at $Q^2 = 1.0$ $(\mathrm{GeV/c})^2$, we plot in Fig. 30 as a function of $P_{S'}$ the value of $G_E^n \pm \Delta G_E^n$ for a beam polarization $P_L = 0.40$ and an average analyzing power $A_y = 0.34$. The points associated with the values of $P_{S'}$ for the three parameterizaitons of G_E^n (viz., dipole, Galster, and $G_E^n = 0$) are denoted differently from those of other values of $P_{S'}$ in the plot. This plot shows that a polarization value in between those for the three cases studied above will generate uncertainties ΔG_E^n that lie in between those of these cases, which were shown in Fig. 29.

5. Background

5.1 Monte – Carlo Simulation of Electron and Neutron Spectra with the Maximum Horizontal Angular Acceptance for Electrons of the High Momentum Spectrometer (HMS)

Proposed kinematic conditions for the quasielastic reaction ed $\rightarrow$ enp are listed in Table II(c). These kinematic conditions were selected to minimize the data acquisition time for achieving a given relative statistical uncertainty in the ratio G_E^n/G_M^n.

We want to be able to discriminate against background neutrons associated with inclusive inelastic processes ed $\rightarrow$ enX. We used the CEBAF Large Acceptance Spectrometer Event Generator (CELEG) of Joyce[21] (1989) to simulate the experiment and to design the acceptances so that the (inelastic) background neutrons represent a sufficiently small fraction of the (quasielastic) signal neutrons. For this study, the ratio of the signal S to the background B is

$$\frac{S}{B} = \frac{ed \rightarrow enp}{ed \rightarrow enX}. \tag{75}$$

CELEG (1989) is a Monte Carlo event generator for lepton-nucleon interactions. In Fig. 31, we plot for the point at $Q^2 = 1.5$ $(\mathrm{GeV/c})^2$ the CELEG-generated

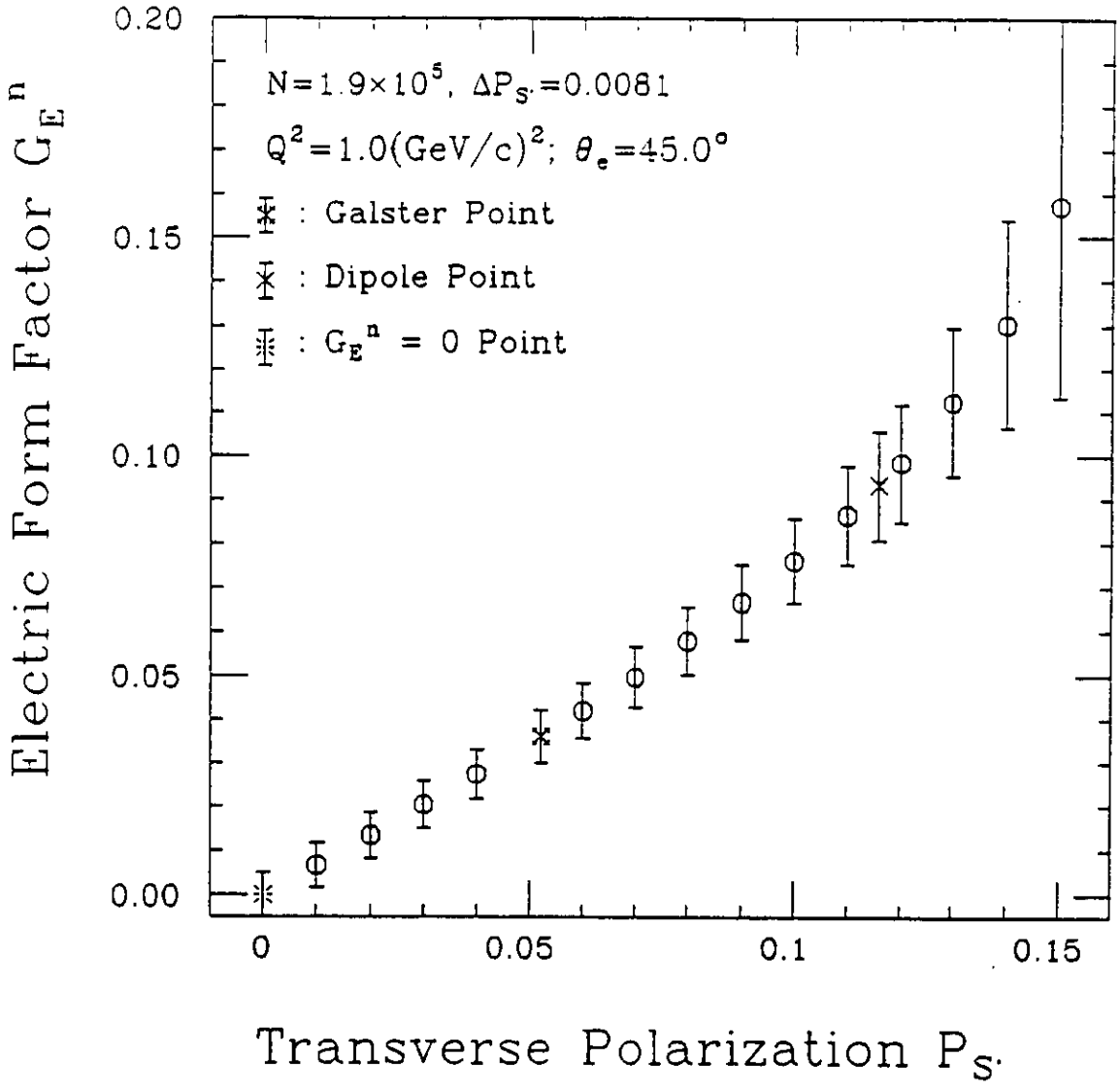

Fig. 30 G_E^n with Expected Uncertainties ΔG_E^n as a Function of $P_{S'}$ at $Q^2 = 1.0$ (GeV/c)^2 for a Data Acquisition Time of 500 hours.

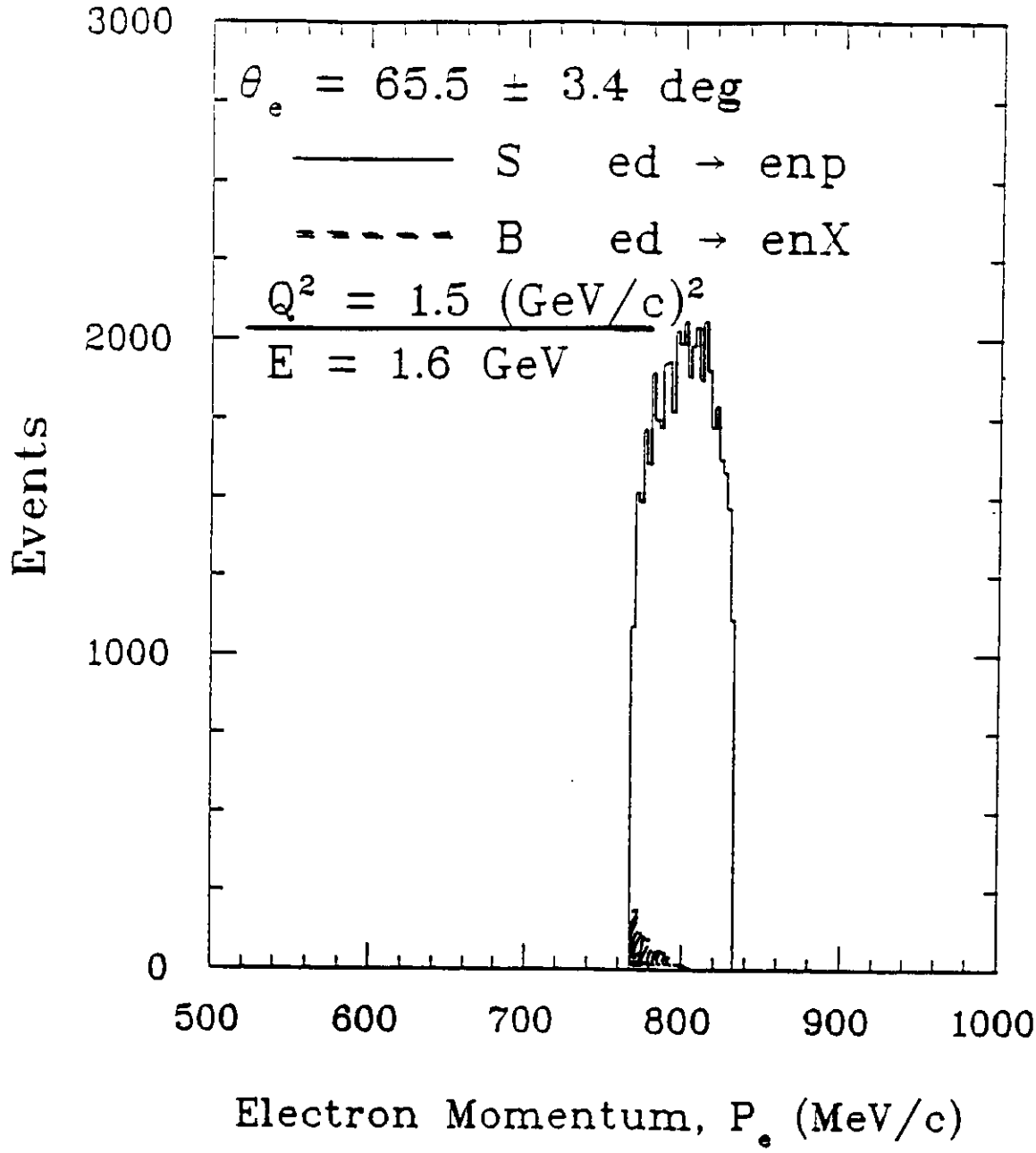

Fig. 31 Electron Momentum Spectrum from CELEG.

momentum spectra of *electrons* that would be seen by the HMS with a maximum horizontal angular acceptance for electrons $\Delta\theta_e = \pm 3.40°$; similarly, Fig. 32 is the CELEG-generated angular distributions of *neutrons* that are expected again with a maximum horizontal angular acceptance for electrons $\Delta\theta_e = \pm 3.40°$. We see from Figs. 31 and 32 that the background neutrons represent a small fraction of the quasielastic signal neutrons.

5.2 Discrimination Against Background Events from Inelastic Processes

In this section, we show that the background from inelastic processes can be reduced to a small fraction of the quasielastic signal events by a suitable choice of $\Delta\theta_n$, the horizontal angular acceptance of the neutron polarimeter, and by reducing the electron momentum bite Δp_e. In Fig. 33 for the point at $Q^2 = 1.5$ (GeV/c)^2 with $E = 1.6$ GeV and $\theta_e = 65.5 \pm 3.4°$, we show the CELEG-generated plots of the ratio of background–to–signal neutrons as a function of $\Delta\theta_n$, the size of one-half of the horizontal angular acceptance of the neutron polarimeter, for values of the electron momentum acceptance $\Delta p_e/p_e = \pm$ 0.050, 0.040, and 0.030. To generate this plot, the cross section for the inelastic process was taken to be equal to that for the quasielastic process. Excitation-energy spectra reveal that these two cross sections are comparable. For $\Delta\theta_n = \pm 3.0°$, we see from Fig. 33 that the background–to–signal ratio for $Q^2 = 1.5$ (GeV/c)^2 is about 1.5% for $\Delta p_e/p_e = \pm 0.050$, about 1% for $\Delta p_e/p_e = \pm 0.040$, and about 0.75% for $\Delta p_e/p_e = \pm 0.030$.

In Fig. 34 for $Q^2 = 1.5$ (GeV/c)^2, we display the *e-n* coincidence events expected on a plot of the neutron angle θ_n versus the electron momentum p_e. The rectangle superimposed on this plot shows the overall acceptance when the neutron angular acceptance $\Delta\theta_n = \pm 3.0°$ and the electron momentum acceptance $\Delta p_e/p_e = \pm 0.040$, which corresponds to an electron momentum bite $\Delta p_e = \pm 0.040\ p_e = \pm(0.040)(800) = \pm 32$ MeV/c.

In Fig. 35, we display the events on a plot of neutron kinetic energy T (MeV) versus electron momentum p_e (MeV/c) with $\Delta\theta_n = \pm 3.0°$. In this plot, we see that

there is a narrow band of events from quasielastic interactions that are separated from a broad band of events from inelastic interactions. Also shown in Fig. 35 is a bar that delineates the neutron energy resolution $\Delta T = \pm 44$ MeV. With this energy resolution, the narrow band of the events from quasielastic interactions does not overlap with the broad band of events from inelastic interactions. This result indicates that the background-to-signal ratio in Fig. 33 can be reduced further by applying a cut on the neutron energy. The resulting CELEG neutron spectra with the selected acceptances are shown in Fig. 36. These CELEG spectra show that the inelastic background events represent a negligibly small fraction of the quasielastic signal events.

5.3 Background from Pion – Electron Coincidences

We used the CELEG code to look at the possibility of coincidences between negative pions and neutrons from the inelastic two pion production process $ed \rightarrow epn\pi^-\pi^+$. The results show that n–π^- coincidence events do not enter into the experimental acceptances of the detectors. In panel (a) of Fig. 37, we see that momentum acceptances alone are sufficient to exclude n–π^- coincidences; in panel (b) and (c), the application of the horizontal angular acceptances further reduces the probability of n–π^- coincidences. After imposing the requirement that the neutron and the negative pion be coplanar (within the azimuthal acceptances), panel (d) shows a significant reduction of the coincidence events because the neutron and the negative pion are not emitted back to back.

There can be no coincidence events from neutrons with negative pions in reactions with single pion production because either a neutron is not associated with a negative pion or a negative pion is not associated with a neutron:

$$ed \rightarrow epp\pi^- \quad (\text{no } n)$$
$$ed \rightarrow enn\pi^- \quad (\text{no } \pi^-)$$
$$ed \rightarrow enp\pi^- \quad (\text{no } \pi^-)$$

The singles rate from negative pions is negligible in comparison with that from

electrons, as can be seen from Fig. 37. Only a very few negative pions can pass the momentum threshold of this experiment, which is 799 MeV/c for Q^2 = 1.5 $(GeV/c)^2$ and E = 1.6 GeV. The remaining acceptances reduce the singles rate from negative prions to a negligible value.

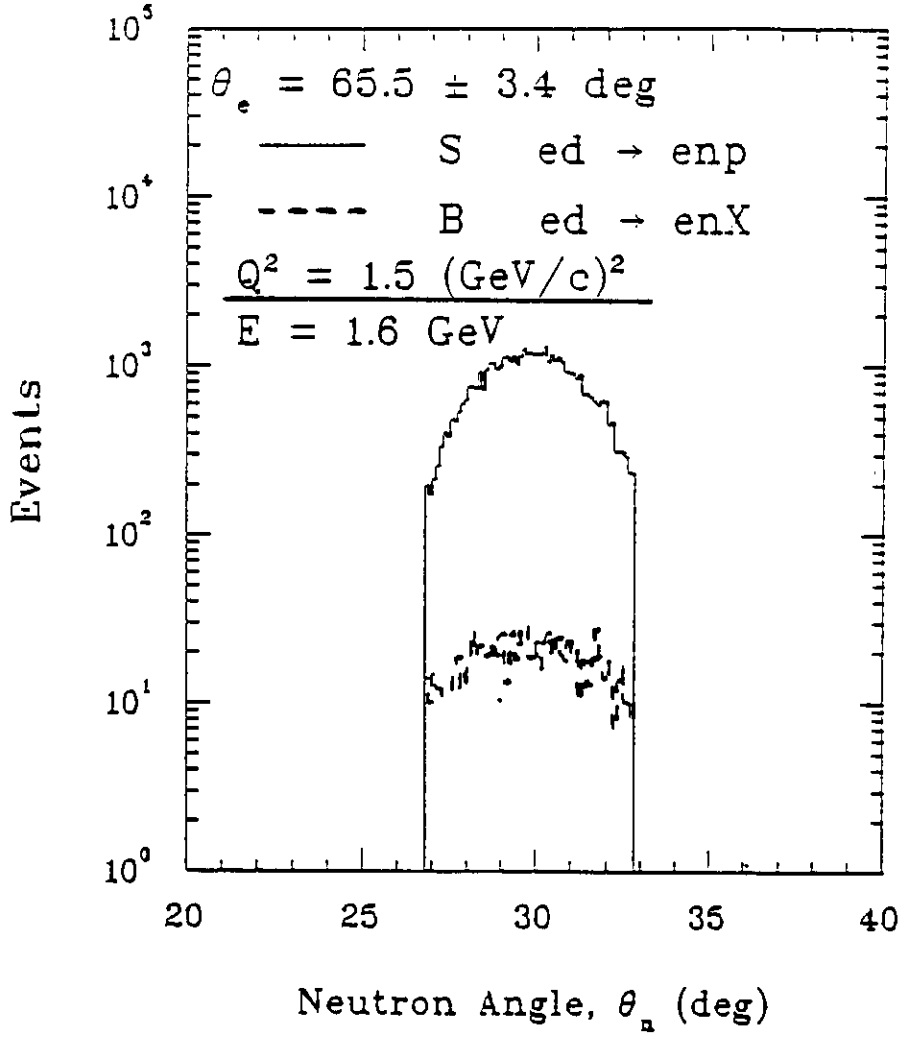

Fig. 32 Neutron Spectra from CELEG.

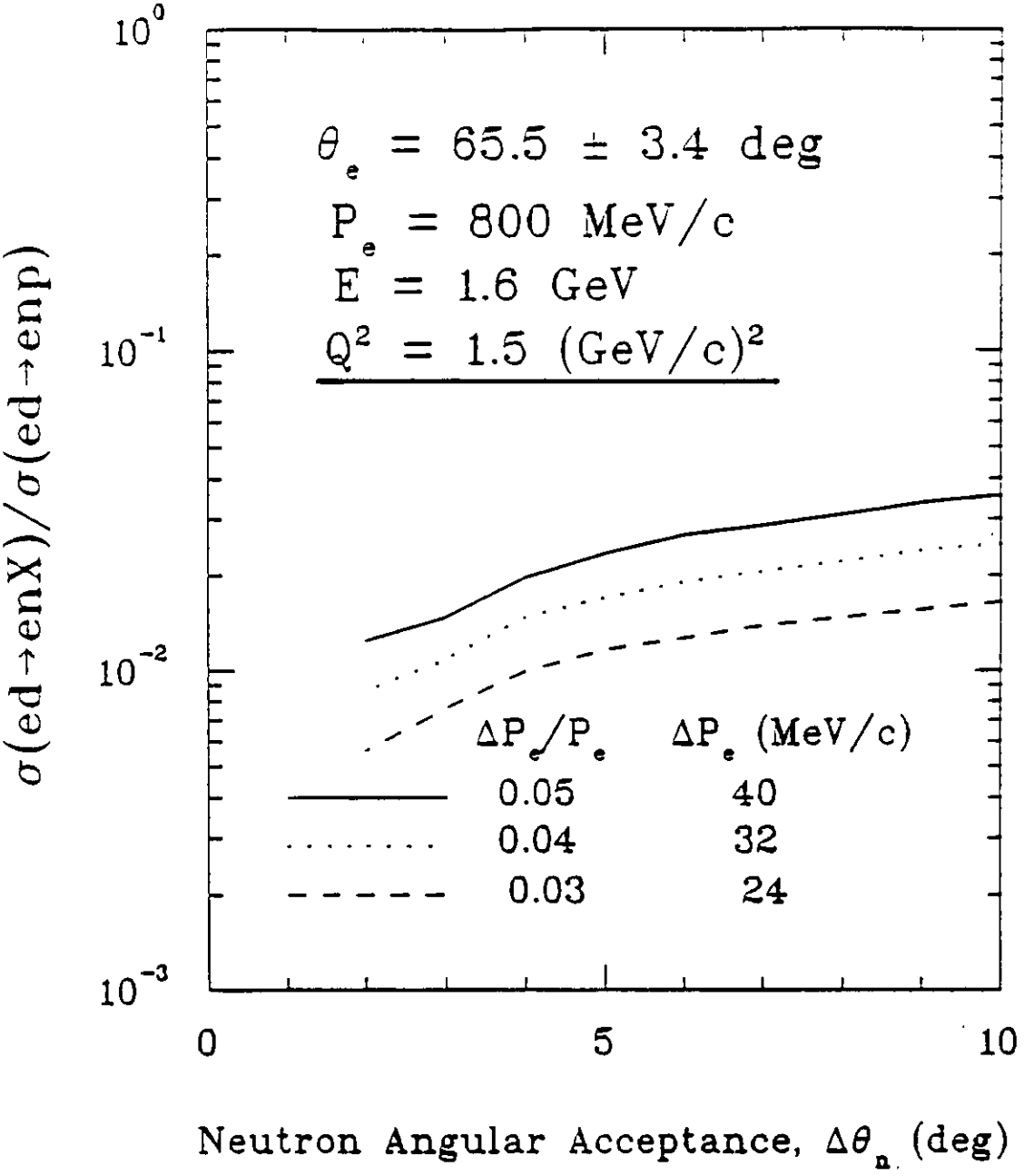

Fig. 33 The Background-to-Signal Ratio vs $\Delta\theta_n$ from CELEG.

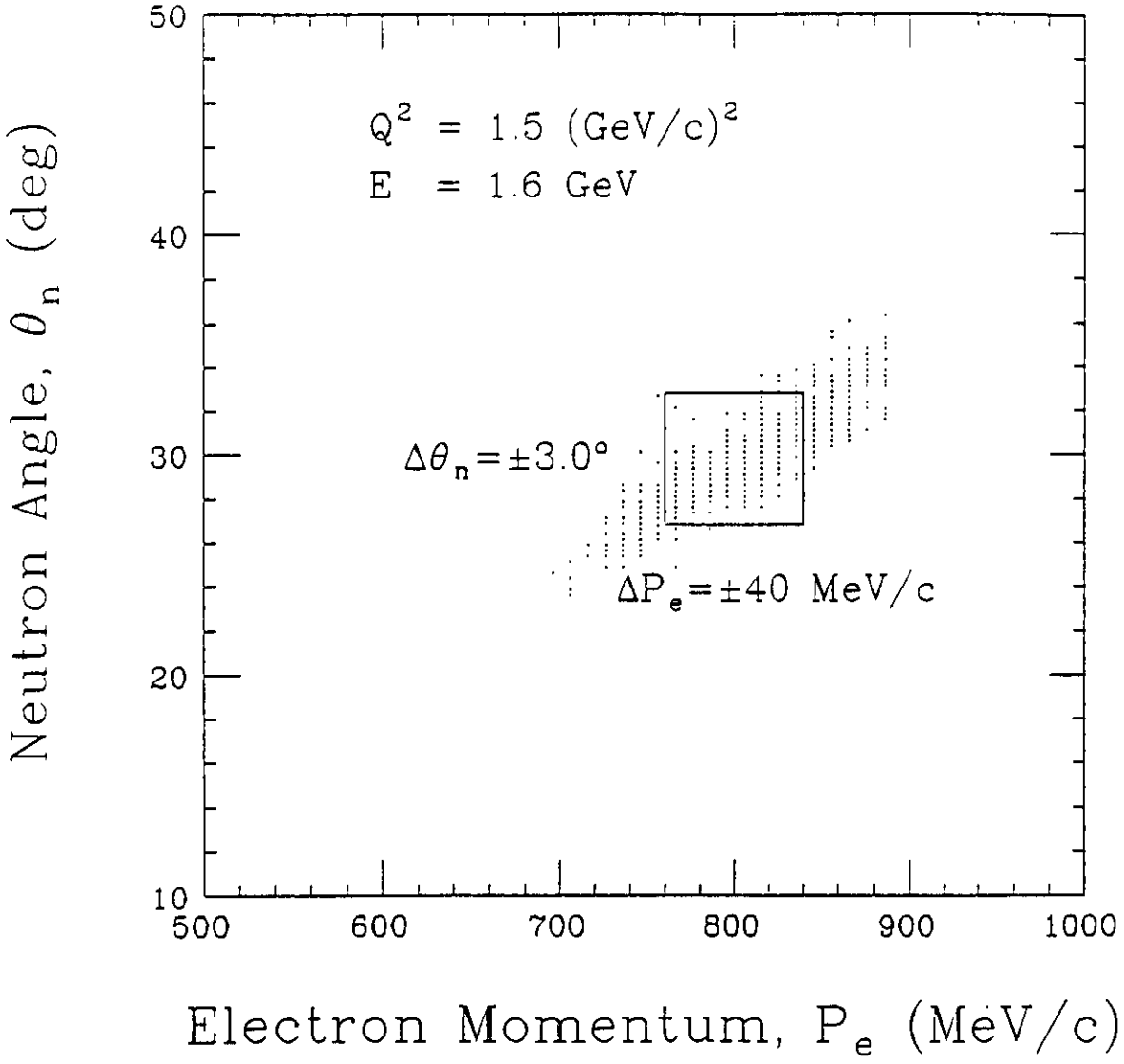

Fig. 34 Neutron Scattering Angle θ_n vs Electron momentum p_e from CELEG.

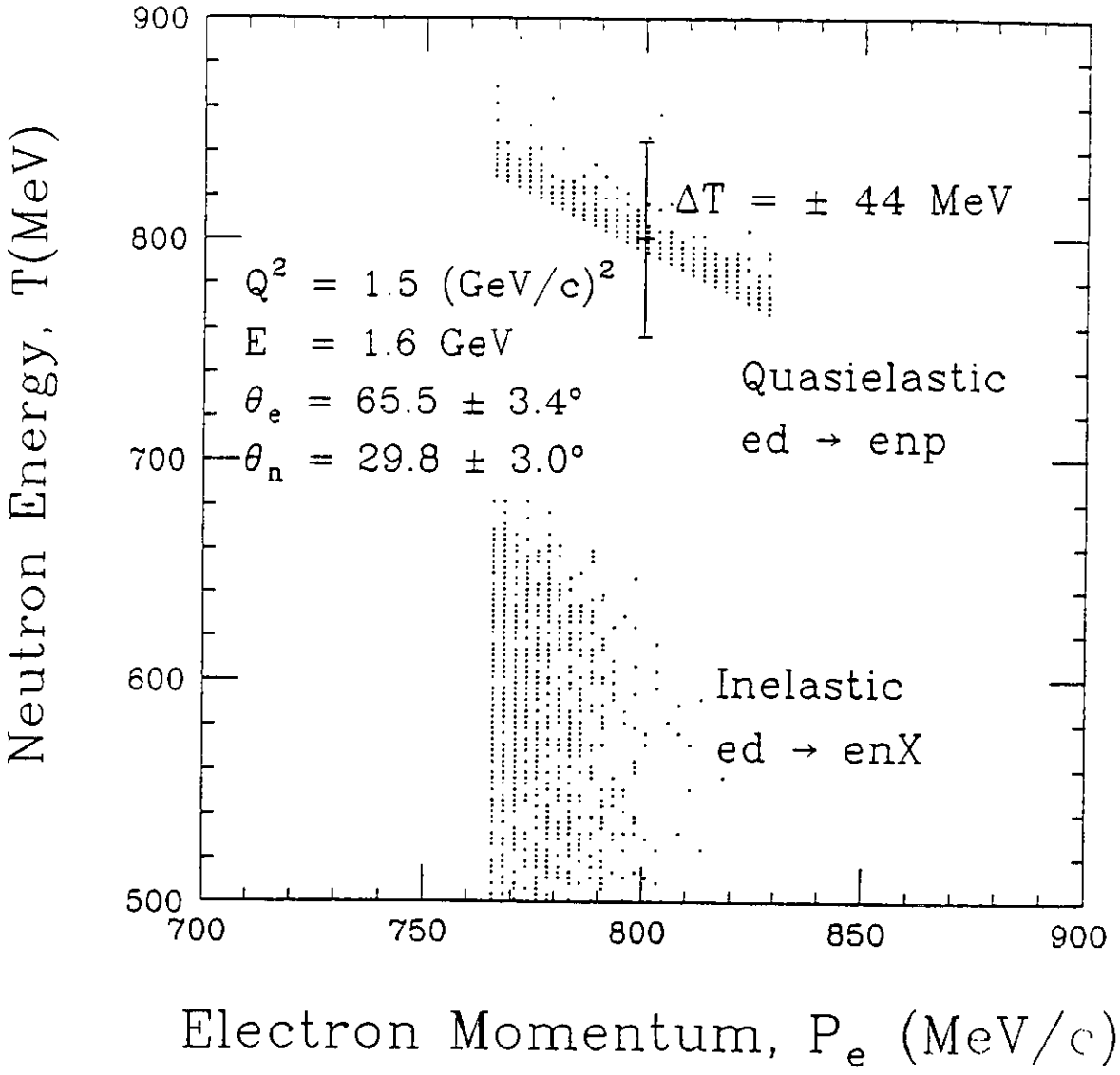

Fig. 35 Neutron Energy T vs Electron momentum p_e from CELEG.

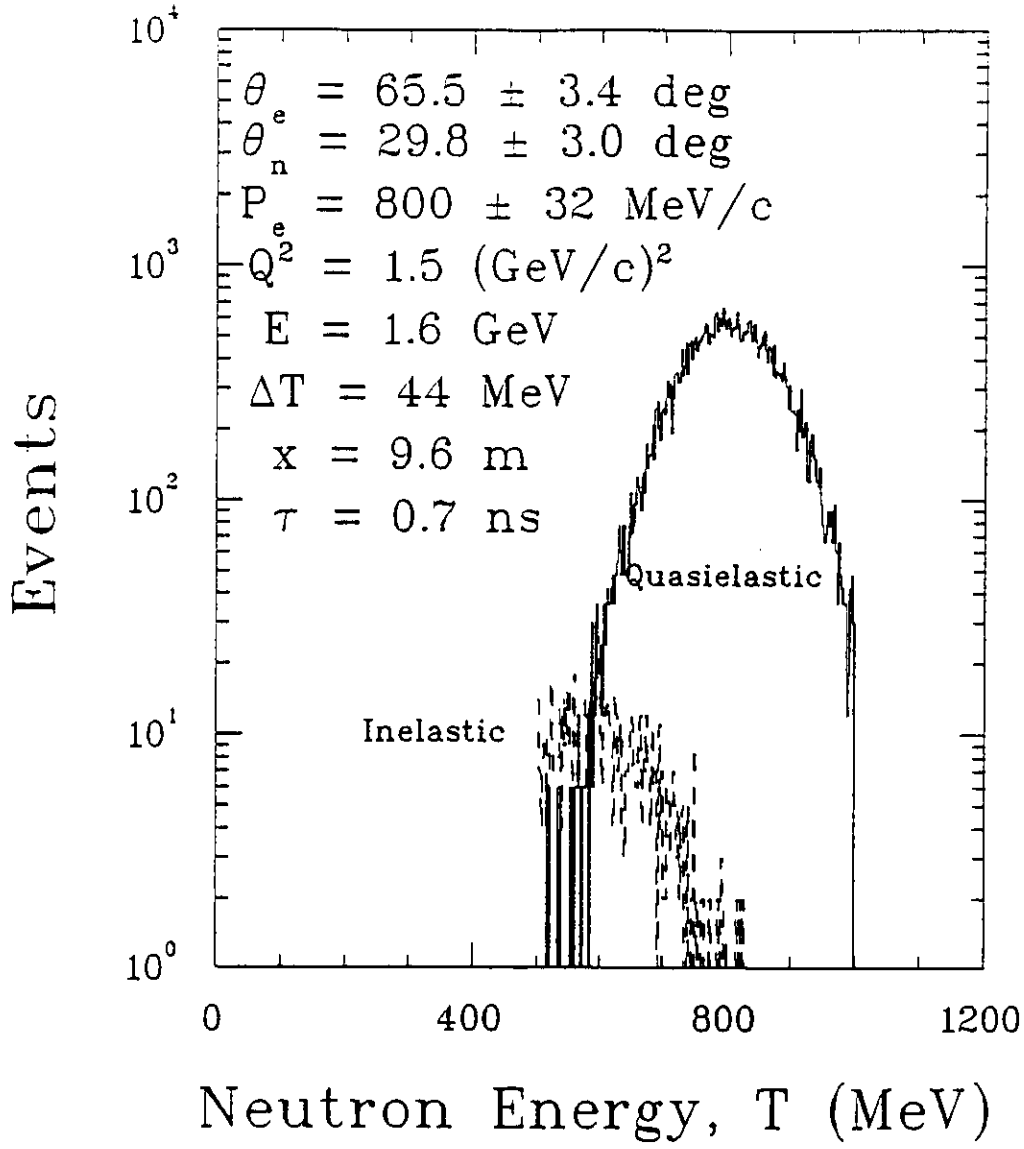

Fig. 36 Neutron Spectra with Selected Acceptances.

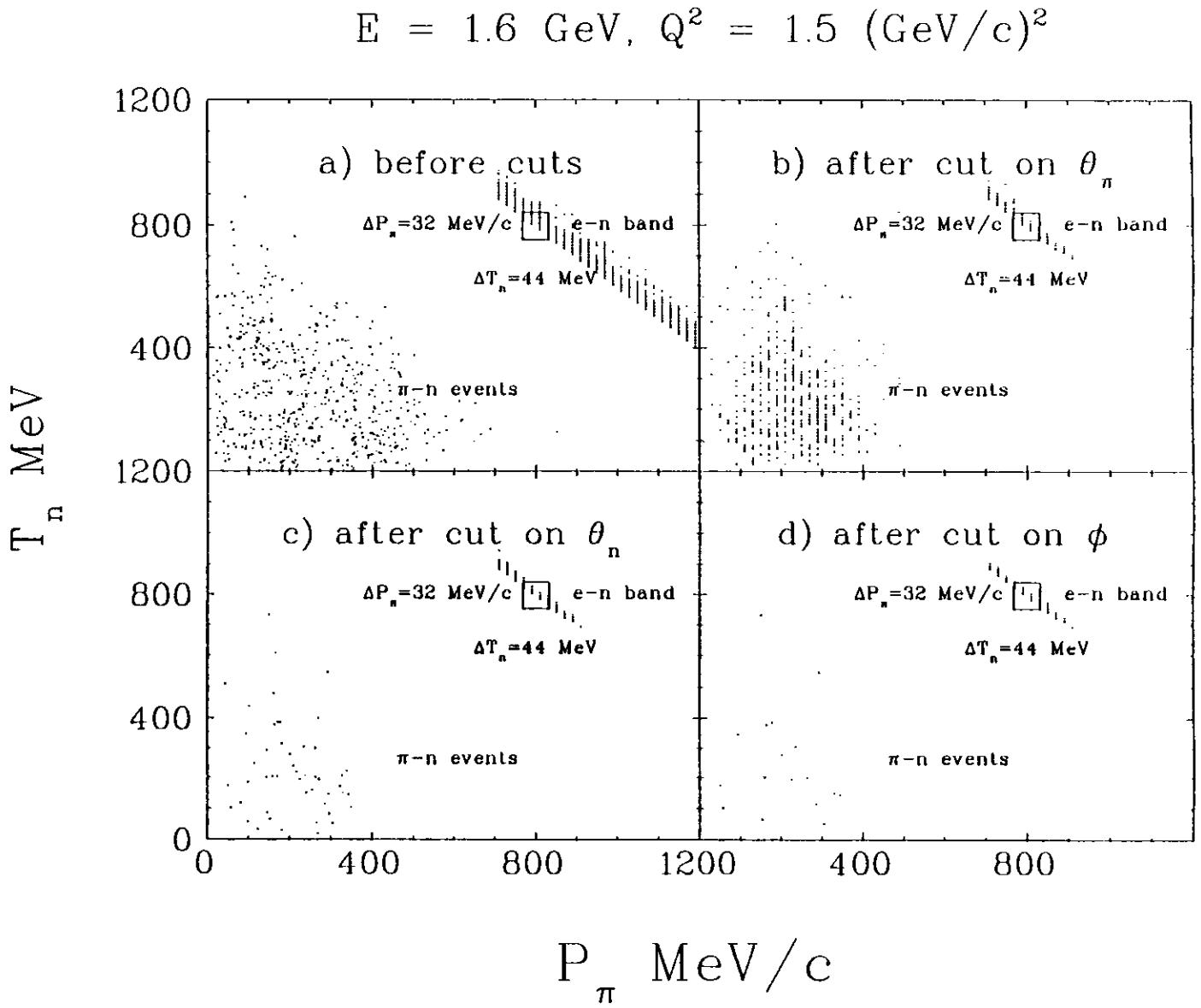

Fig. 37 Pion-neutron Coincidence Events from CELEG.

6. Beam Time Request

We propose initially to carry out a measurement at one value of Q^2. The beam-time request for a measurement of G_E^n at $Q^2 = 1.0$ (GeV/c)^2 with a luminosity of 3.2×10^{38} cm^{-2} s^{-1} is as follows:

Activity	Beam on Target(hr)
1. Tuneup and checkout	**60**
1.1 Electron spectrometer	24
1.2 Neutron polarimeter	24
1.3 Electron-neutron coincidences	12
2. Data acquisition	**544**
2.1 LD_2 target	500
2.2 Dummy target cell	48
2.3 Shadow shield(with LD_2 target)	48
2.4 LH_2 target	48
3. Electron beam polarization measurement [(3 hr/meas)(1 meas/day)(20 day)]	**60**
4. Overhead* ($\sim$ 10%)	**66**
5. Contingency ($\sim$ 10%)	**70**
TOTAL	**900**

*** Reversal of direction of beam polarization, checking liquid deuterium target, insertion and removal of targets, pulse-height calibrations of polarimeter detectors, stopping and restarting data acquisition system,...**

We propose to carry out a measurement at $Q^2 = 1.0$ (GeV/c)^2 initially, and then to make measurements at the other Q^2 points in separately scheduled runs. The data acquisition times with an LD_2 target (item 2.1 in the above listing) were shown in Table X to be 150, 250, 500, 500, and 800 hours at $Q^2 = 0.30$, 0.50, 1.0, 1.5, and 2.0 (GeV/c)^2 respectively; accordingly, the total beam time needed to carry out these five measurements at CEBAF in separately scheduled runs is as

follows:

Q^2 (GeV/c)^2	Time on LD_2 (hrs)	Total Time (hrs)
0.30	150	**550**
0.50	250	**650**
Subtotal A	400	**1200**
1.0	500	**900**
1.5	500	**900**
2.0	800	**1200**
Subtotal B	1800	**3000**
TOTAL	2200	**4200**

If the two points at $Q^2 = 0.30$ and 0.50 (GeV/c)^2 are carried out at Bates, then the beam time request from CEBAF is reduced from 4200 hours to 3000 hours.

In Figs. 38 through 42, we plot the projected relative statistical and total uncertainties in G_E^n for the five Q^2 points proposed. The proposed data acquisition time is indicated by a vertical line in each plot. The purpose of these plots is to show that increasing the data acquisition times beyond the proposed values will not reduce the total uncertainty substantially; in other words, above some critical value of the data acquisition time, the statistical uncertainty is no longer the dominating contribution to the total uncertainty. For the data acquisition times proposed here, this statement is especially true for the case of the dipole parameterization $g = -\tau$.

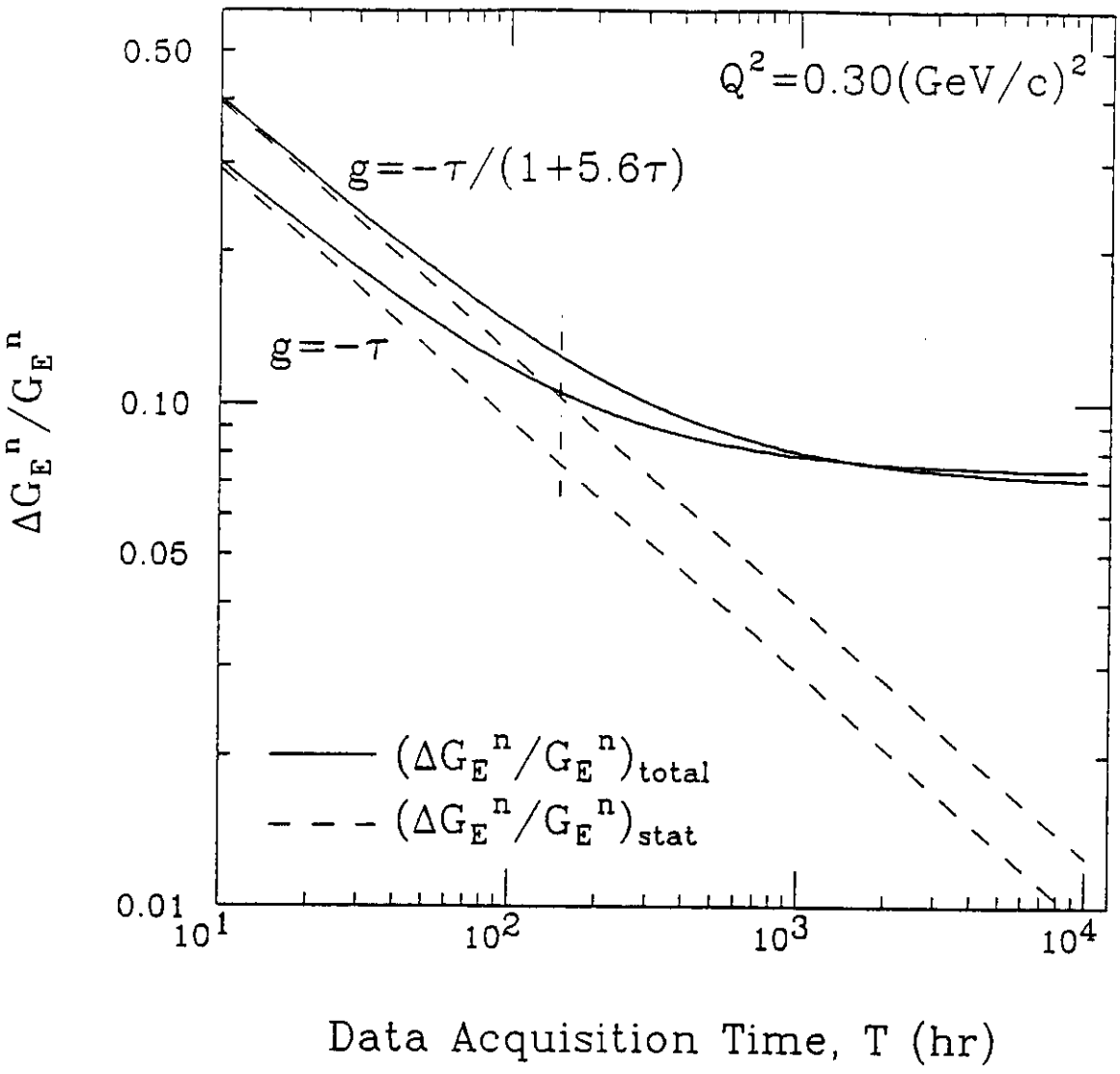

Fig. 38 Relative Uncertainty in G_E^n vs Data Acquisition Time for $Q^2 = 0.30$ $(\mathrm{GeV/c})^2$ and $E = 0.8$ GeV. The dash-dotted vertical line specifies the designed data acquisition time (150 hr).

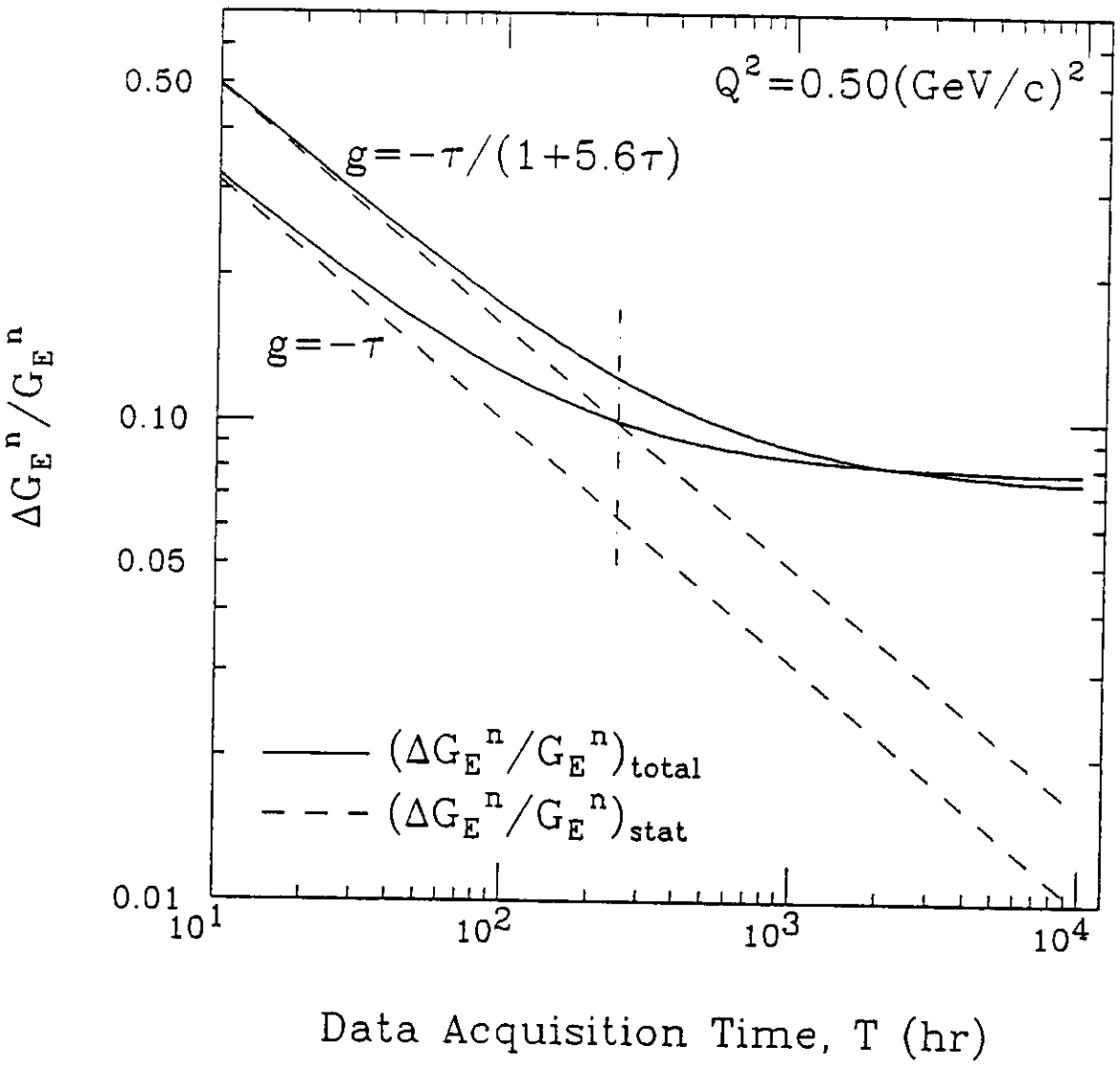

Fig. 39 Relative Uncertainty in G_E^n vs Data Acquisition Time for $Q^2 = 0.50$ $(\mathrm{GeV/c})^2$ and $E = 0.8$ GeV. The dash-dotted vertical line specifies the designed data acquisition time (250 hr).

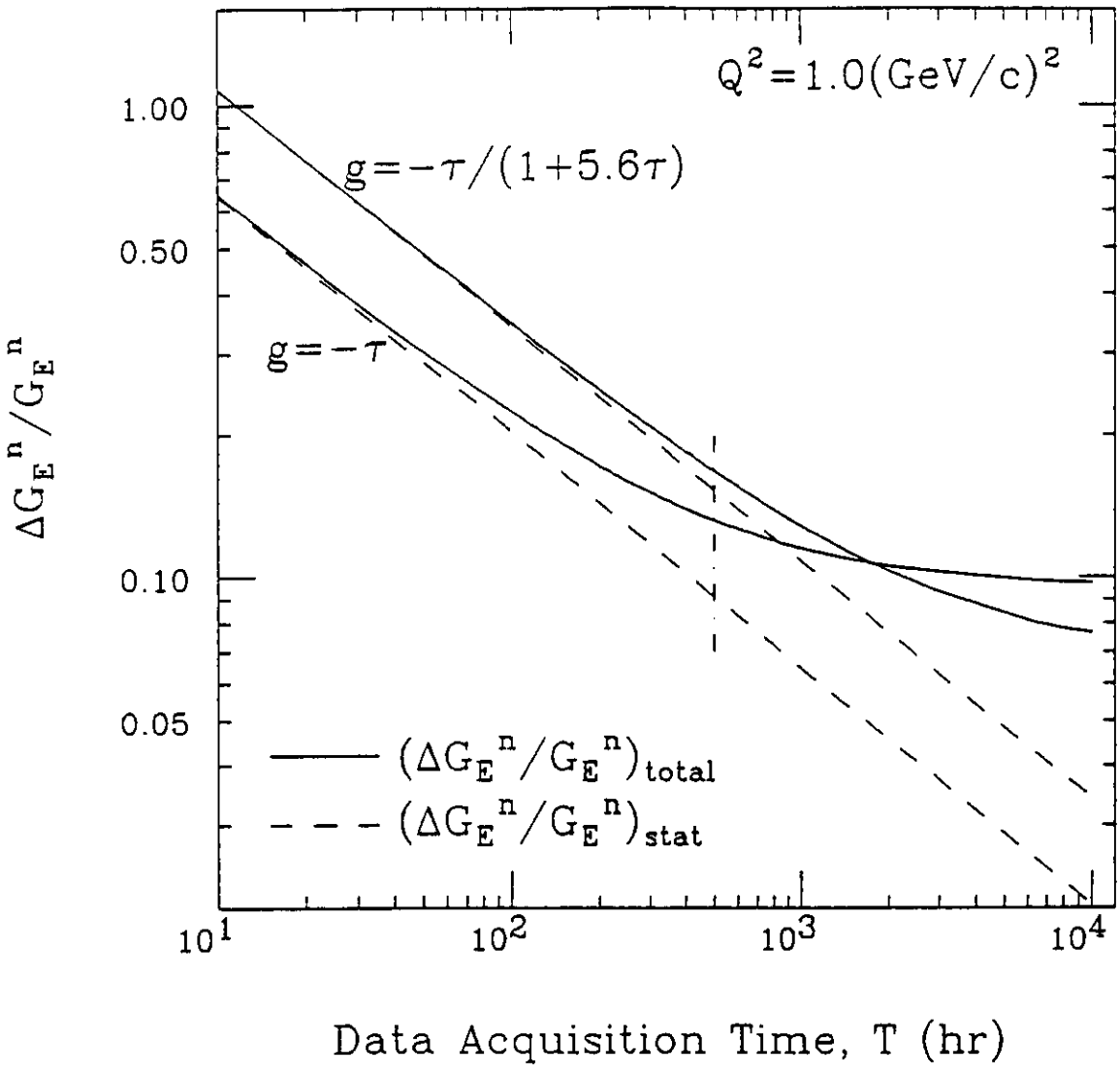

Fig. 40 Relative Uncertainty in G_E^n vs Data Acquisition Time for $Q^2 = 1.0$ $(GeV/c)^2$ and $E = 1.6$ GeV. The dash-dotted vertical line specifies the designed data acquisition time (500 hr).

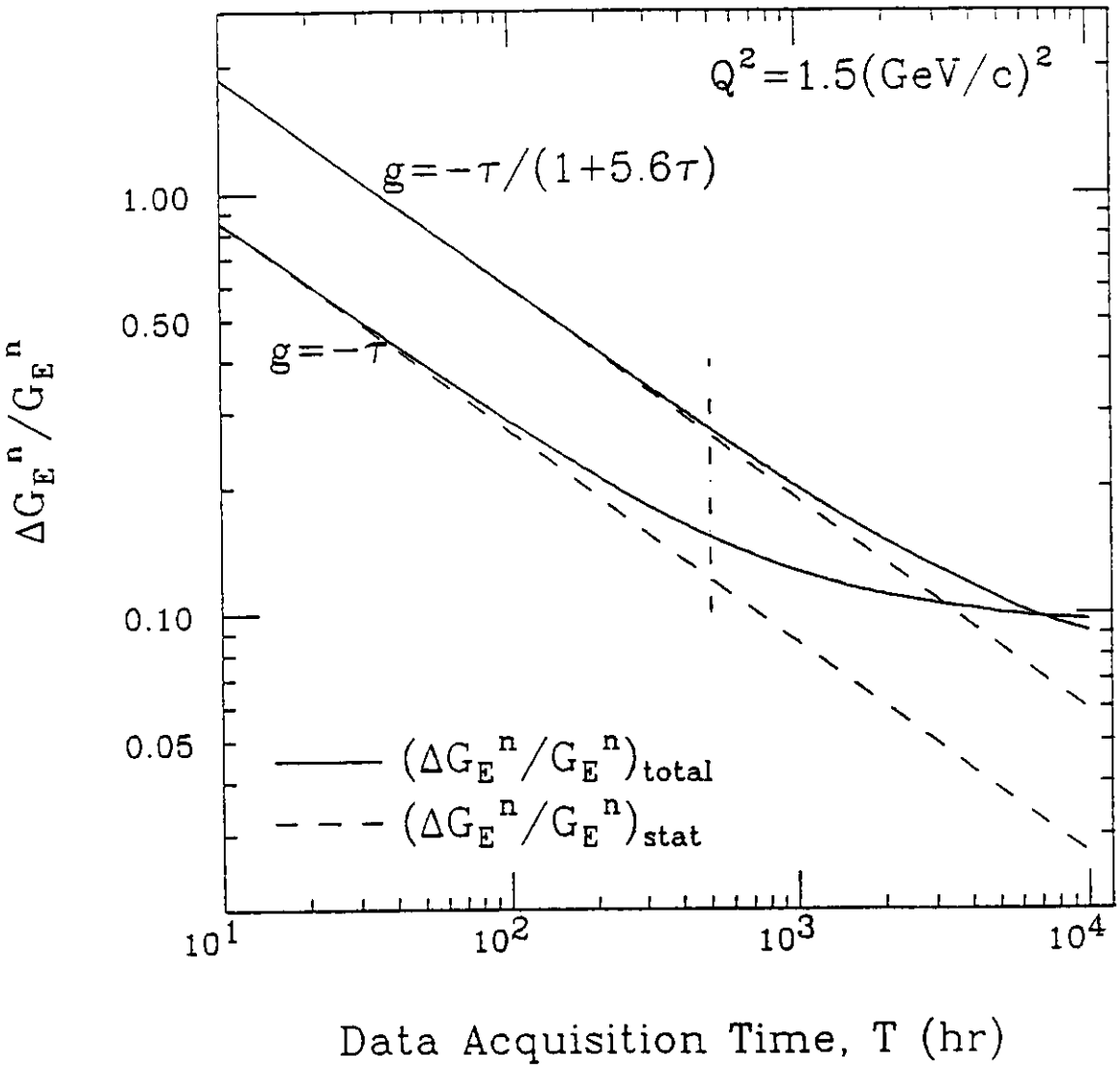

Fig. 41 Relative Uncertainty in G_E^n vs Data Acquisition Time for $Q^2 = 1.5$ $(GeV/c)^2$ and $E = 1.6$ GeV. The dash-dotted vertical line specifies the designed data acquisition time (500 hr).

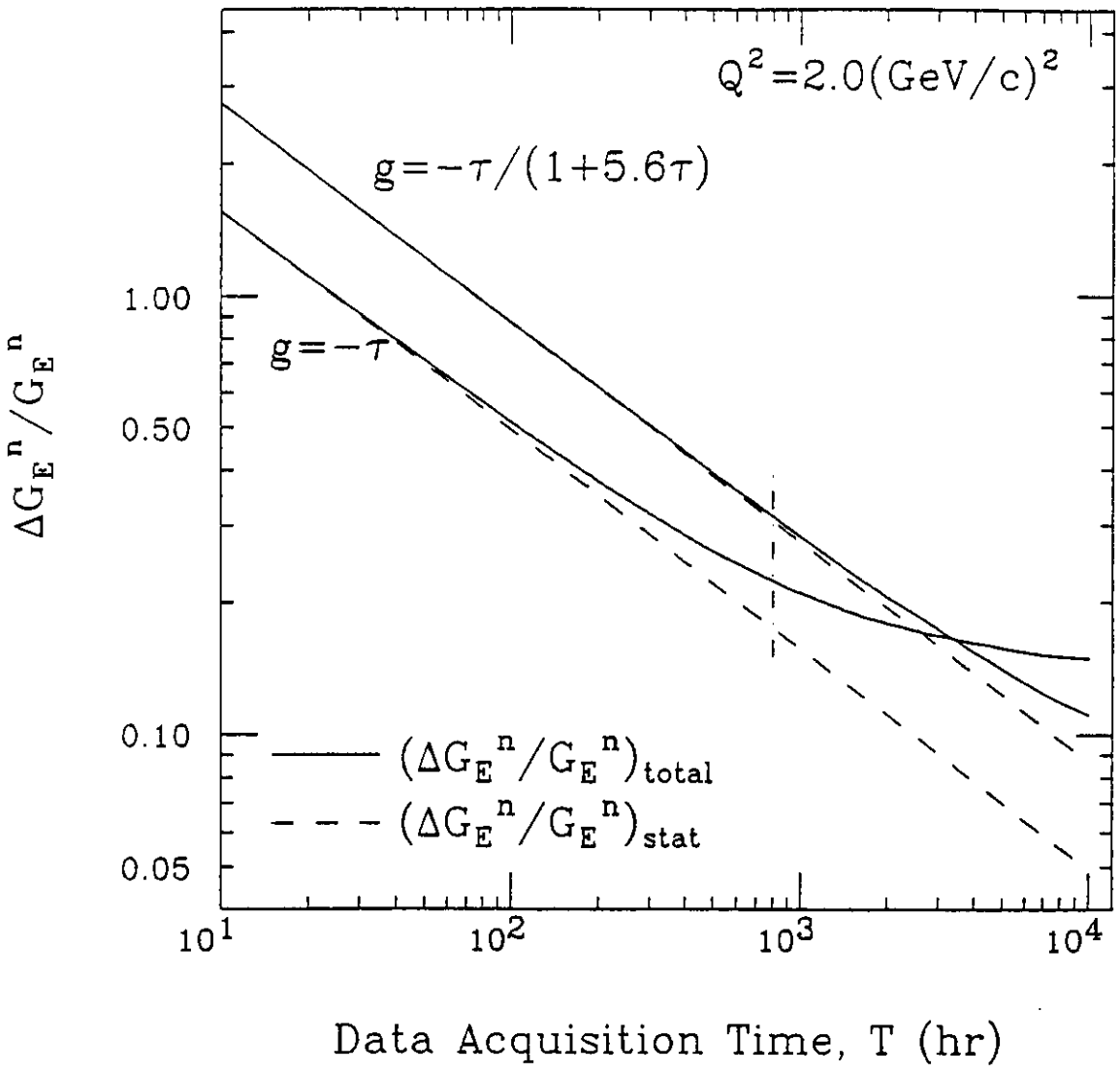

Fig. 42 Relative Uncertainty in G_E^n vs Data Acquisition Time for $Q^2 = 2.0$ (GeV/c)^2 and $E = 2.4$ GeV. The dash-dotted vertical line specifies the designed data acquisition time (800 hr).

References

1. V. E. Krohn and G. R. Ringo, Phys. Rev. 148, 1021 (1966); L. Koester *et al*, Phys. Rev. Lett. 36, 1021 (1976).

2. S. Platchkov, A. Amroun, S. Auffret, J. M. Cavedon, P. Dreus, J. Duclos, B. Frois, D. Goutte, H. Hachemi, J. Martino, X.-H. Phan and I. Sick, Nucl. Phys. 508A,343c (1990).

3. A. Lung *et al.*, SLAC-NE11 Collaboration Phys. Rev. Lett. 70, 718(1993).

4. T. Eden *et al.*, unpublished.

5. H. Arenhövel, Phys. Lett. B199, 13 (1987); W. Fabian and H. Arenhövel, Nucl. Phys. A314, 253 (1979).

6. S. Galster, H. Klein, J. Moritz, K. H. Schmidt, D. Wegener, and J. Blechwenn, Nucl. Phys. B32, 221 (1971).

7. H. Arenhövel, Private Communication, 1993.

8. G. Beck and H. Arenhövel, Few-Body Systems 13, 165(1992).

9. M. P. Rekalo, G. I. Gakh, and A. P. Rekalo, J. Phys. G15, 1223 (1989).

10. B. Mosconi, J. Pauchenwein, and P. Ricci, Proceedings of the XIII European Conference on Few-Body Problems in Physics, Marciana Marina (Elba), Italy (Septembet 1991).

11. J. M. Laget, Phys. Lett. B273, 367 (1990).

12. J. L. Friar, Phys. Rev. C42, 2310 (1990).

13. M. F. Gari and W. Krümpelmann, Phys. Lett. B274, 159 (1992).

14. R. G. Arnold, C. E. Carlson, F. Gross, Phys. Rev. C23, 363 (1981).

15. R. Madey, A. R. Baldwin, P. J. Pella, J Schambach, and R. M. Sellers, IEEE Trans. Nucl. Sci. 36, 231 (1989).

16. R. A. Arndt, R. H. Hackman, and L. D. Roper, Phys. Rev. C15, 1002 (1977); R. A. Arndt and L. D. Roper, Scattering Analysis Interactive Dialin (SAID) program, Virginia Polytechnic Institute and State University, unpublished.

17. P. E. Ulmer, MCEEP: Monte Carlo for Electron–Nuclear Coincidence Experiments, CEBAF-TN-91-101 (1991).

18. S. Dytmann, Private communication (1987).

19. E. Moniz, Phys. Rev. 184, 1154 (1969).

20. J. W. Lightbody and J.S. O'Connell, Computers in Physics May/June 1988, p.57.

21. D. Joyce, CELEG ≡ CEBAF Large Acceptance Acceptance Spectrometer Events Generator, CLAS Note 89–004 (1989).

APPENDIX A

THE RANGE OF p_r and θ_{nq}^{lab} FOR MODEL-INSENSITIVE $P_{S'}$

Because we are measuring the transverse polarization component $P_{S'}$ of the neutron in the $d(\vec{e}, e'\vec{n})p$ reaction, we would like to understand the range of recoil momentum p_r and the corresponding range of neutron scattering angle $\Delta\theta_n$ that permits $P_{S'}$ to be insensitive to final–state interactions (FSI), meson–exchange currents (MEC), and isobar configurations (IC). Based on principles of quasielastic scattering, the smaller the recoil momentum of the residual system (meaning the smaller the $\Delta\theta_n$), the less it will interact with the outgoing particle, which is the neutron in this particular reaction.

In his papers on deuteron electrodisintegration, Arenhövel[5] considers the proton as the ejected nucleon and the neutron as the recoiling nucleon. He defines $\Theta_{np}^{c.m.}$ as the angle between the proton and the three-momentum transfer $\vec{q}^{\,c.m.}$ in the center-of-mass system. In the $d(\vec{e}, e'\vec{n})p$ reaction, the neutron is the ejected nucleon and the proton is the recoiling nucleon; accordingly, we want to present in this appendix a relationship between the recoil momentum p_r of the proton in the lab frame as a function of $\Theta_{np}^{c.m.}$. Note that $\Theta_{np}^{c.m.} = \pi$ for neutron emission along $\vec{q}^{\,c.m.}$. From Arenhövel, we obtain the maximum value of $\Theta_{np}^{c.m.}$ that corresponds to the lack of sensitivity of the neutron polarization vector $P_{S'}$ to FSI, MEC, IC, and deuteron wavefunctions. From this information, we can determine the maximum value of the recoil momentum p_r that preserves this insensitivity to the model. Finally, we calculate the neutron angular spread $\Delta\theta_n$ with respect to the three-momentum vector in the lab frame that preserves this insensitivity to FSI, MEC, IC, and deuteron wavefunctions.

For the five independent variables that govern the coincidence cross section, Arenhövel[5] chooses the electron scattering angle θ_e^{lab}, the *c.m.* momentum transfer $q^{c.m.}$, the relative n–p energy in the *c.m.* $E_{np}^{c.m.}$, and the polar and azimuthal angles $\Theta_{np}^{c.m.}$ and $\phi_{np}^{c.m.}$ between the relative n–p motion and the direction of the momentum transfer $q^{c.m.}$. These variables have counterparts in the lab frame. Shown in Fig. A1

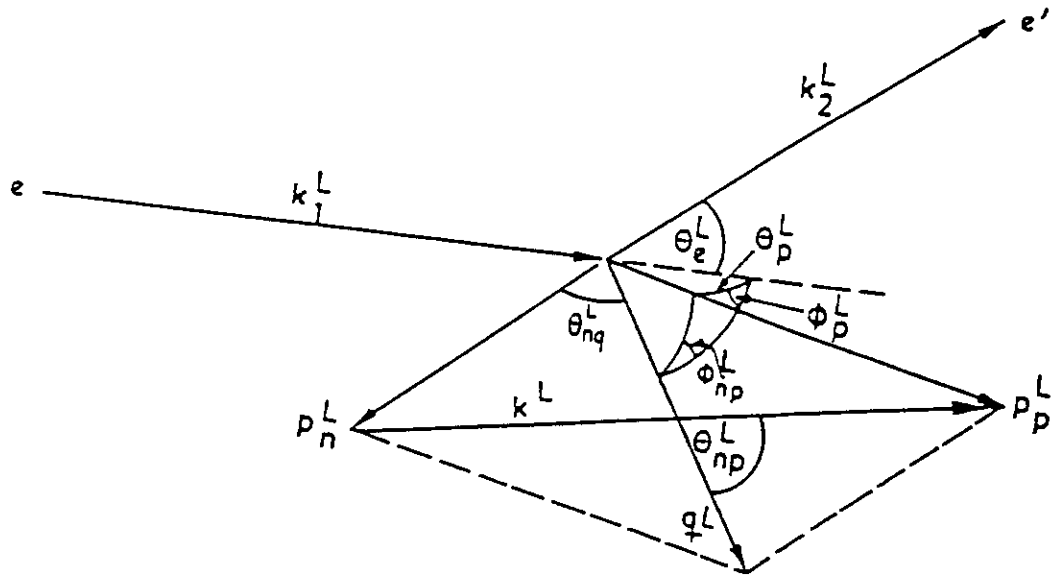

Fig. A1 A Schematic View of the Geometry for Electrodisintegration of the Deuteron in the Lab Frame.

is a schematic diagram of the geometry for the electrodisintegration of the deuteron in the lab frame. The lab angle θ_{np}^{lab} is defined as the angle between the vector $\mathbf{k}^{lab}$ ($\equiv \mathbf{P}_p^{lab} - \mathbf{P}_n^{lab}$) and the three–momentum transfer $\mathbf{q}^{lab}$. The azimuthal angle ϕ_{np}^{lab} is interpreted as the angle between the reaction plane (defined by the vectors $\mathbf{q}^{lab}$, $\mathbf{P}_n^{lab}$, and $\mathbf{P}_p^{lab}$) and the scattering plane (defined by the vectors $\mathbf{k}_1^{lab}$ and $\mathbf{k}_2^{lab}$). Note that when $\phi_{np}^{lab} = 0°$ or 180°, we have parallel kinematics; and when $\phi_{np}^{lab} = 180°$, $\mathbf{P}_n^{lab}$ and $\mathbf{P}_p^{lab}$ are transposed. For parallel kimematics and for neutron emission along $\vec{q}$ (*i.e.*, with $\theta_{np}^{lab} = \pi$), the value for the neutron polarization $P_{S'}$ in the scattering plane perpendicular to the neutron momentum vector $\vec{q}$ is the same at $\phi_{np}^{lab} = 0°$ and 180°. Shown in Fig. A2 is the transverse neutron polarization $P_{S'}$ versus $\Theta_{np}^{c.m.}$ for $\phi_{np} = 0°$ and 180°; at $\Theta_{np}^{c.m.} = 180°$, $P_{S'}$ has the same value for $\phi_{np} = 0°$ and 180°.

The mathematical relations relating the two reference frames, and leading to the dependence of p_r on $\Theta_{np}^{c.m.}$ will now be presented. First, we note that the input to Arenhövel's calculations for a particular set of kinematics is the incident electron energy E, scattered electron energy E', and scattered electron angle θ_e^{lab}; therefore, Q^2 is readily given by

$$Q^2 = 4EE' \sin^2\left(\theta_e^{lab}/2\right) \quad . \tag{A1}$$

Because the four–momentum transfer–squared is an invariant quantity, $Q^2 = (Q^{c.m.})^2$. The energy of the deuteron system in the *c.m.* is

$$E_d^{c.m.} = \sqrt{(Q^{c.m.})^2 + M_d^2} \quad . \tag{A2}$$

Here M_d is the deuteron mass. The energy transfer $\omega^{c.m.}$ in the *c.m.* system is given by the expression

$$\omega^{c.m.} = (E_d)^{-1}\left[\omega^{lab} M_d - (Q^{c.m.})^2\right] \quad . \tag{A3}$$

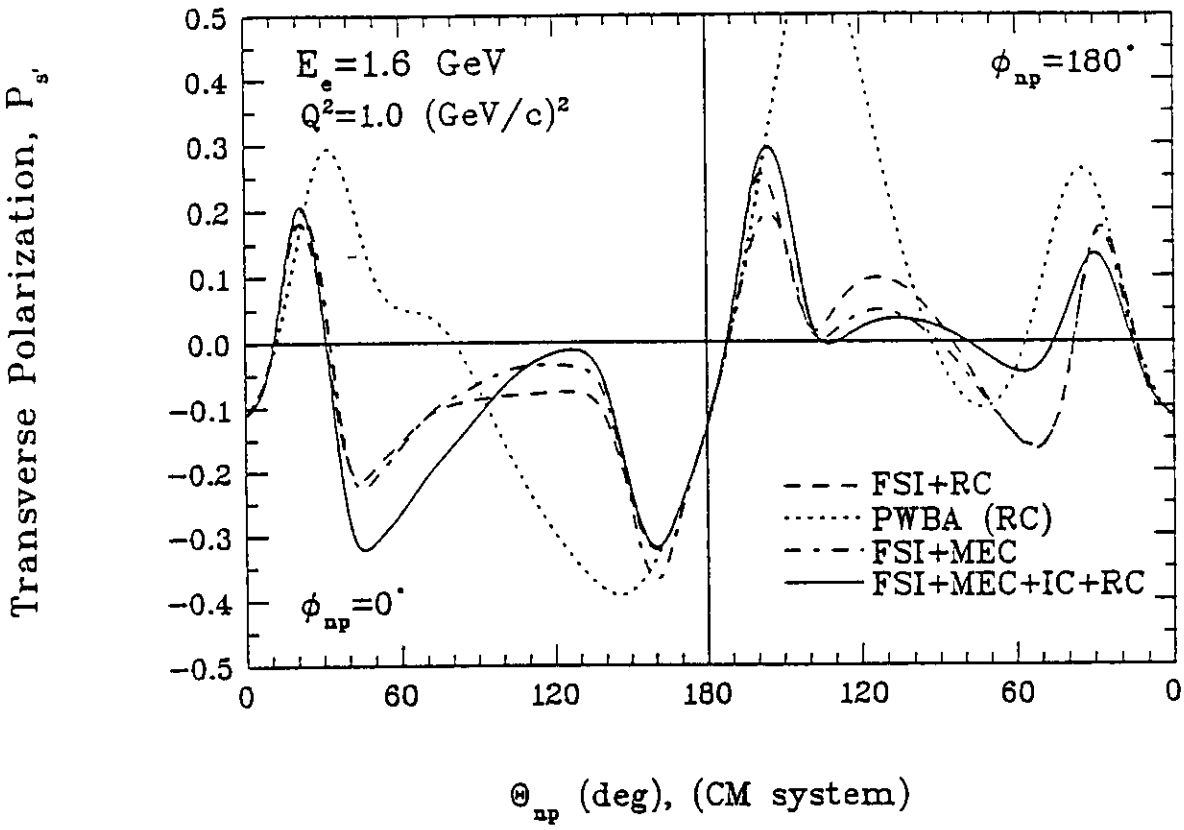

Fig. A2 Transverse neutron polarization $P_{S'}$ with dipole parameterization versus $\Theta_{np}^{c.m.}$ for $\phi_{np} = 0°$ and 180° at $Q^2 = 1.0$ (GeV/c)^2 with $E = 1.6$ GeV. Note that at $\Theta_{np}^{c.m.} = 180°$, $P_{S'}$ has the same value for $\phi_{np} = 0°$ and 180°.

The energy $E_{np}^{c.m.}$ is related to $\omega^{c.m.}$ by

$$E_{np}^{c.m.} = \omega^{c.m.} + E_d^{c.m.} - 2M = W - 2M \ , \qquad (A4)$$

where M is the nucleon rest mass, and W is the invariant mass of the hadronic final state; therefore,

$$M_{np} \equiv W = E_{np}^{c.m.} + 2M \ . \qquad (A5)$$

The three–momentum transfer $q^{c.m.}$ in the $c.m.$ system is given by

$$q^{c.m.} = \left(\frac{M_d}{M_{np}}\right) q^{lab} \ , \qquad (A6)$$

and the three-momentum $k^{c.m.}$ of the n–p system in the $c.m.$ frame is given by

$$k^{c.m.} = \sqrt{E_{np}^{c.m.}\left(E_{np}^{c.m.} + 4M\right)} \ . \qquad (A7)$$

The scattering angle θ_{np}^{lab} can then be written as

$$\theta_{np}^{lab} = \cos^{-1}\left\{\cos\Theta_{np}^{c.m.}\left[1 - \left(\frac{q^{c.m.}}{E_d^{c.m.}}\right)^2 \sin^2\Theta_{np}^{c.m.}\right]^{-1/2}\right\} \ . \qquad (A8)$$

From Fig. A1, we deduce that the recoil momentum of the proton is given by

$$p_r = \left[\left(\frac{k^{lab}}{2}\right)^2 + \left(\frac{q^{lab}}{2}\right)^2 + \left(\frac{k^{lab}q^{lab}}{2}\right)\cos\Theta_{np}^{lab}\right]^{1/2} \ , \qquad (A9)$$

and the neutron scattering angle with respect to the direction of three-momentum transfer $\vec{q}$ is

$$\theta_{nq}^{lab} = \cos^{-1}\left[\frac{(q^{lab}/2)^2 + P_n^2 - (k^{lab}/2)^2}{P_n\, q^{lab}}\right] . \qquad (A10)$$

Plotted in Figs. A3 through A7 as a function of $\Theta_{np}^{c.m.}$ is the transverse polarization component $P_{S'}$ of the neutron for the kinematics given in Table II

of the proposal for the dipole and the Galster parameterizations of G_E^n. These calculations made use of the Paris potential wavefunctions. In the region away from pure quasielastic scattering (*i.e.*, $\Theta_{np}^{c.m.} = 180°$ or neutron emission along $\vec{q}$), these calculations of Arenhövel indicate that $P_{S'}$ is insensitive to FSI, MEC, and IC even when $\Theta_{np}^{c.m.}$ is about ten to twenty degrees (depending on kinematics) away from 180° (the quasielastic peak). In Figs. A8 through A12, we show p_r and θ_{nq}^{lab} as a function of $\Theta_{np}^{c.m.}$ calculated by Eq.(A9) and A(10). From these plots, we know the value of the recoil momentum p_r and the associated θ_{qn}^{lab} corresponding to the $\Theta_{np}^{c.m.}$ that ensures $P_{S'}$ to be insensitive to FSI, MEC, and IC. Listed in Table A1 for the proposed kinematic conditions and for the dipole parameterization of G_E^n are values of $180.0 - \Theta_{np}^{c.m.}$, p_r and θ_{nq}^{lab} that preserve the insensitivity of $P_{S'}$ to FSI, MEC, and IC. Corresponding results for the Galster parameterization are listed in Table A2. From these tables, we see that a choice of $\Delta\theta_n = \pm 3.00°$, which is made after considering the horizontal matching and the background reduction, as described in detail in the proposal, will ensure that our measurement of $P_{S'}$ will be insensitive to FSI, MEC, and IC, and deuteron wavefunctions.

Table A1. $180° - \Theta_{np}^{c.m.}$, p_r, and θ_{nq}^{lab} for Model-Insensitive $P_{S'}$ in the Dipole Parameterization

Q^2 $(\mathrm{GeV/c})^2$	θ_e (deg)	θ_n (deg)	q (MeV/c)	$180° - \Theta_{np}^{c.m.}$ (deg)	p_r (MeV/c)	$\Delta\theta_n$ (deg)
0.30	45.1	52.3	572	$\sim \pm 15$	$\sim \pm 72$	$\sim \pm 7.2$
0.50	65.7	39.8	757	$\sim \pm 17$	$\sim \pm 105$	$\sim \pm 7.9$
1.0	45.0	41.2	1133	$\sim \pm 15$	$\sim \pm 131$	$\sim \pm 6.6$
1.5	65.6	29.8	1464	$\sim \pm 15$	$\sim \pm 160$	$\sim \pm 6.3$
2.0	46.6	33.1	1771	$\sim \pm 10$	$\sim \pm 124$	$\sim \pm 4.0$

Table A2. $180° - \Theta_{np}^{c.m.}$, p_r, and θ_{nq}^{lab} for Model-Insensitive $P_{S'}$ in the Galster Parameterization

Q^2 $(GeV/c)^2$	θ_e (deg)	θ_n (deg)	q (MeV/c)	$180° - \Theta_{np}^{c.m.}$ (deg)	p_r (MeV/c)	$\Delta\theta_n$ (deg)
0.30	45.1	52.3	572	$\sim \pm 10$	$\sim \pm 72$	$\sim \pm 4.8$
0.50	65.7	39.8	757	$\sim \pm 15$	$\sim \pm 105$	$\sim \pm 7.0$
1.0	45.0	41.2	1133	$\sim \pm 15$	$\sim \pm 131$	$\sim \pm 6.6$
1.5	65.6	29.8	1464	$\sim \pm 17$	$\sim \pm 160$	$\sim \pm 7.1$
2.0	46.6	33.1	1771	$\sim \pm 10$	$\sim \pm 124$	$\sim \pm 4.0$

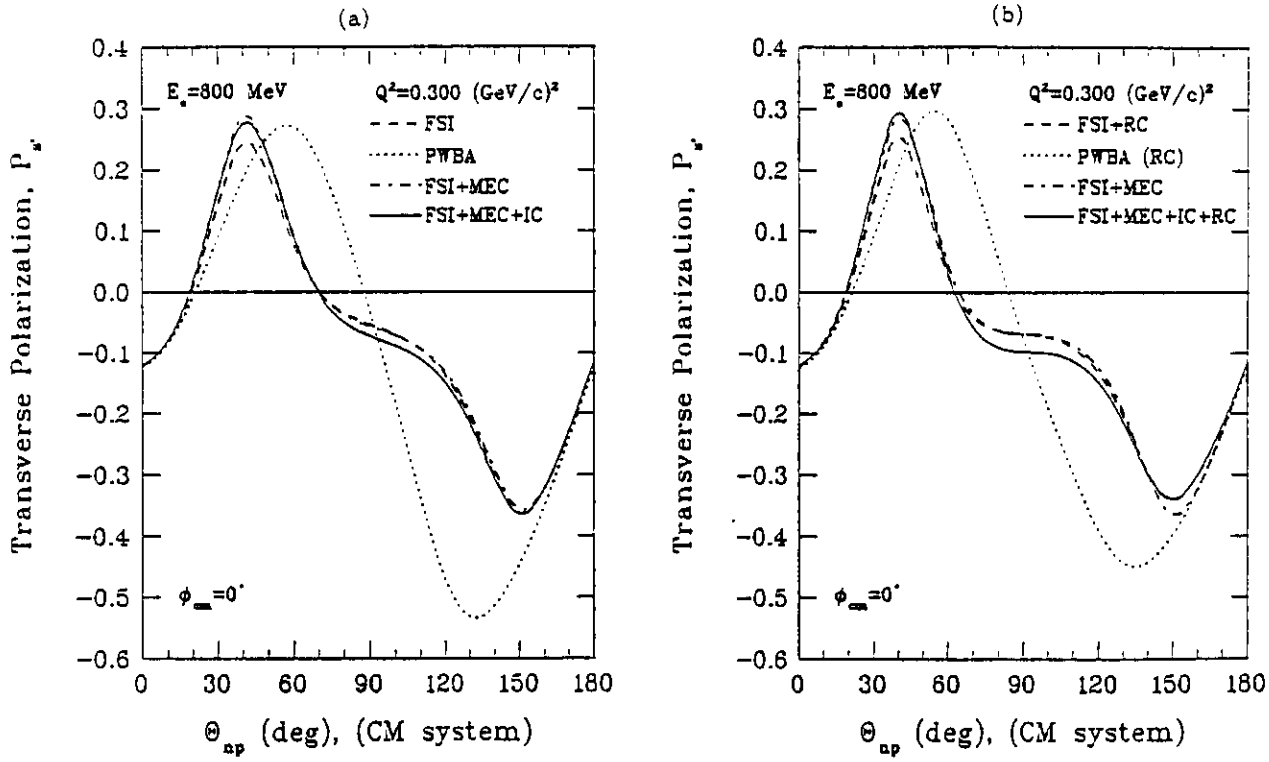

Fig. A3 Transverse Polarization $P_{S'}$ of the Neutron from $d(\vec{e}, e'\vec{n})p$ Reaction as a Function of $\Theta_{np}^{c.m.}$ for $Q^2 = 0.3$ $(GeV/c)^2$ with $E = 0.8$ GeV: (a) Result for Dipole Parameterization of G_E^n, and (b) Result for Galster Parameterization of G_E^n.

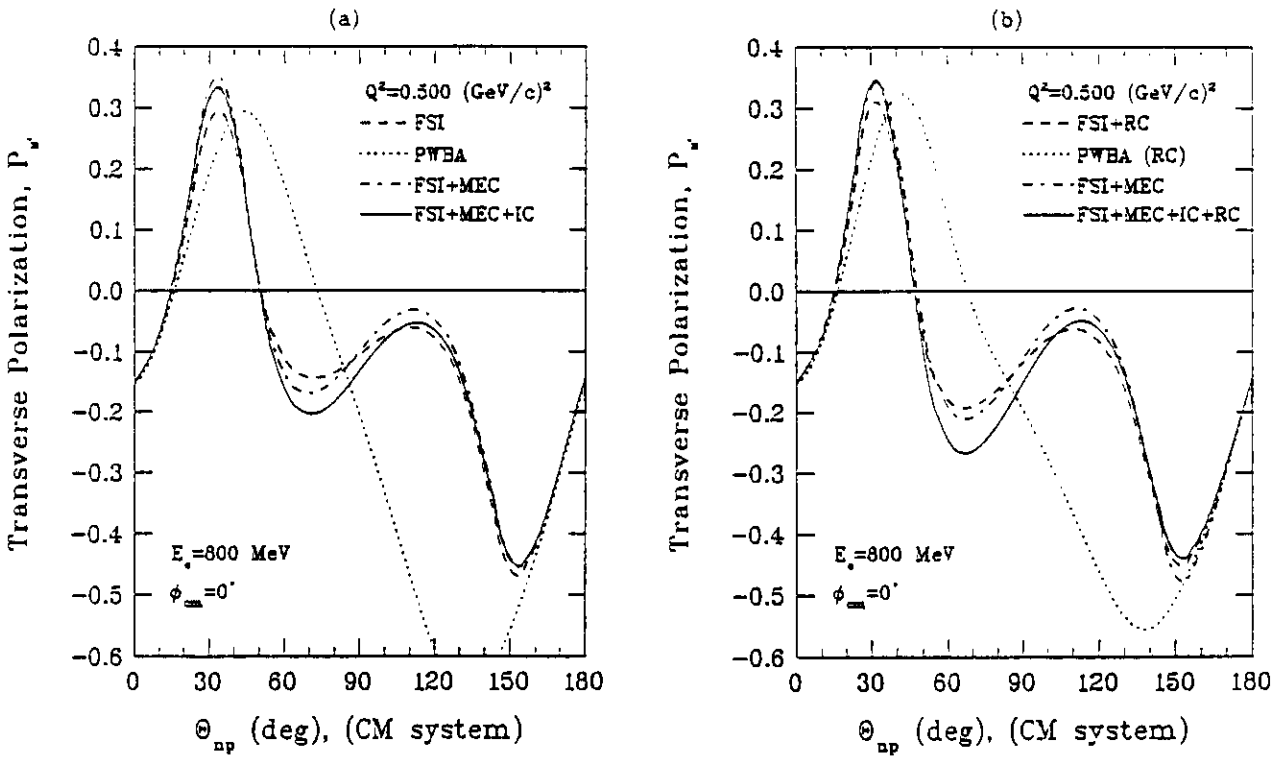

Fig. A4 Transverse Polarization $P_{S'}$ of the Neutron from $d(\vec{e}, e'\vec{n})p$ Reaction as a Function of $\Theta_{np}^{c.m.}$ for $Q^2 = 0.5$ (GeV/c)^2 with $E = 0.8$ GeV: (a) Result for Dipole Parameterization of G_E^n, and (b) Result for Galster Parameterization of G_E^n.

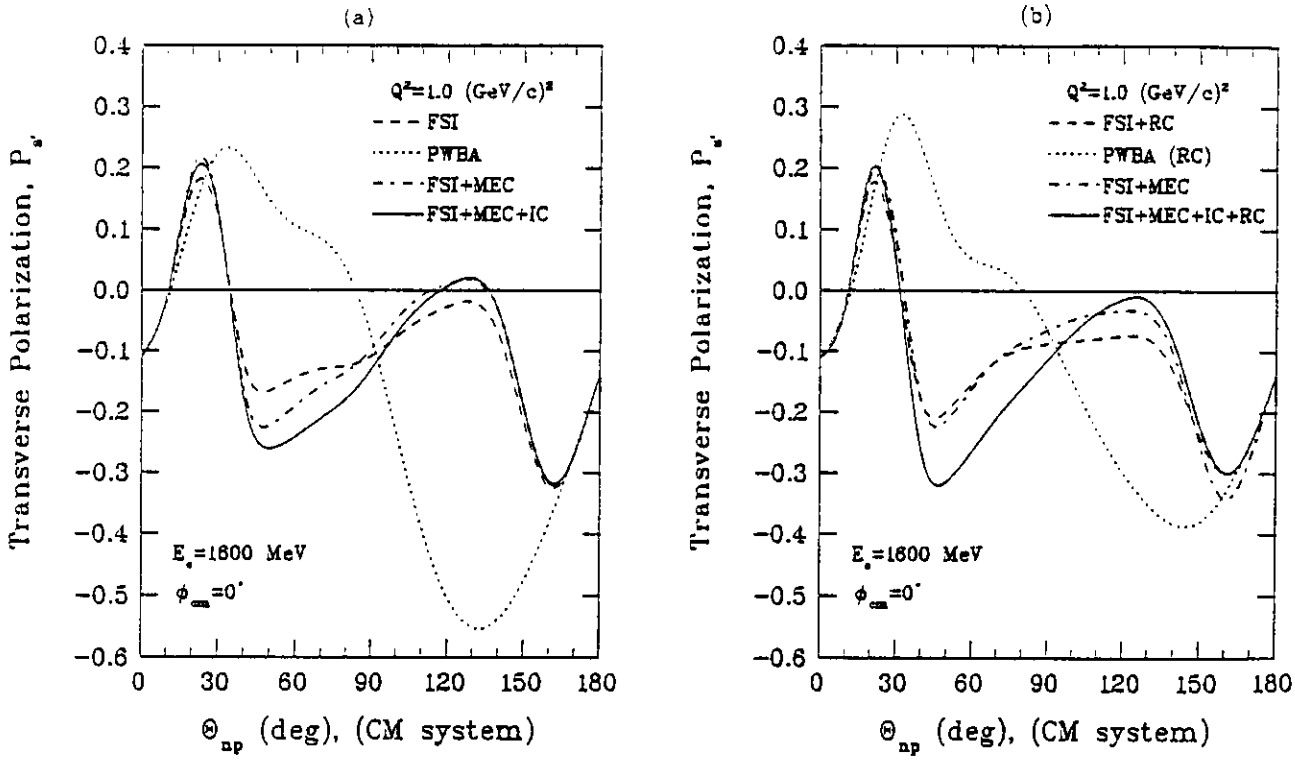

Fig. A5 Transverse Polarization $P_{S'}$ of the Neutron from $d(\vec{e}, e'\vec{n})p$ Reaction as a Function of $\Theta_{np}^{c.m.}$ for $Q^2 = 1.0$ (GeV/c)^2 with $E = 1.6$ GeV: (a) Result for Dipole Parameterization of G_E^n, and (b) Result for Galster Parameterization of G_E^n.

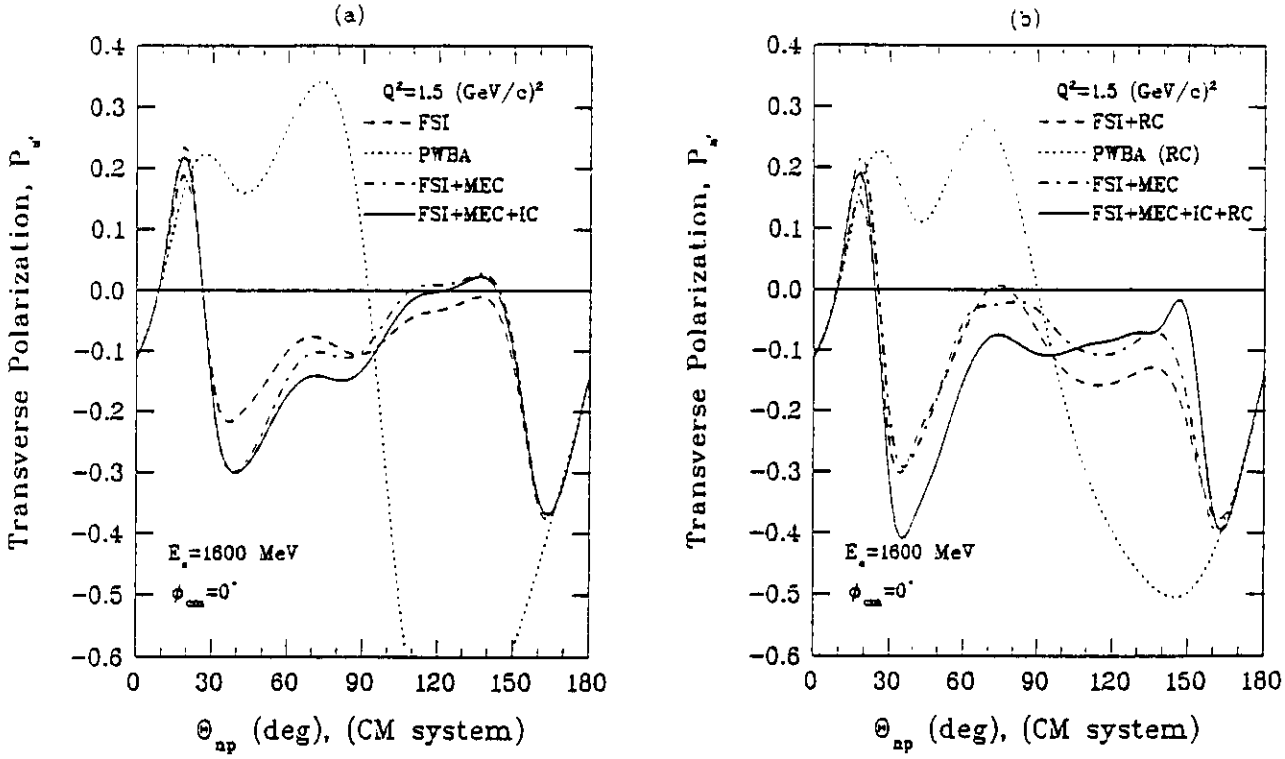

Fig. A6 Transverse Polarization $P_{S'}$ of the Neutron from $d(\vec{e}, e'\vec{n})p$ Reaction as a Function of $\Theta_{np}^{c.m.}$ for $Q^2 = 1.5$ (GeV/c)^2 with $E = 1.6$ GeV: (a) Result for Dipole Parameterization of G_E^n, and (b) Result for Galster Parameterization of G_E^n.

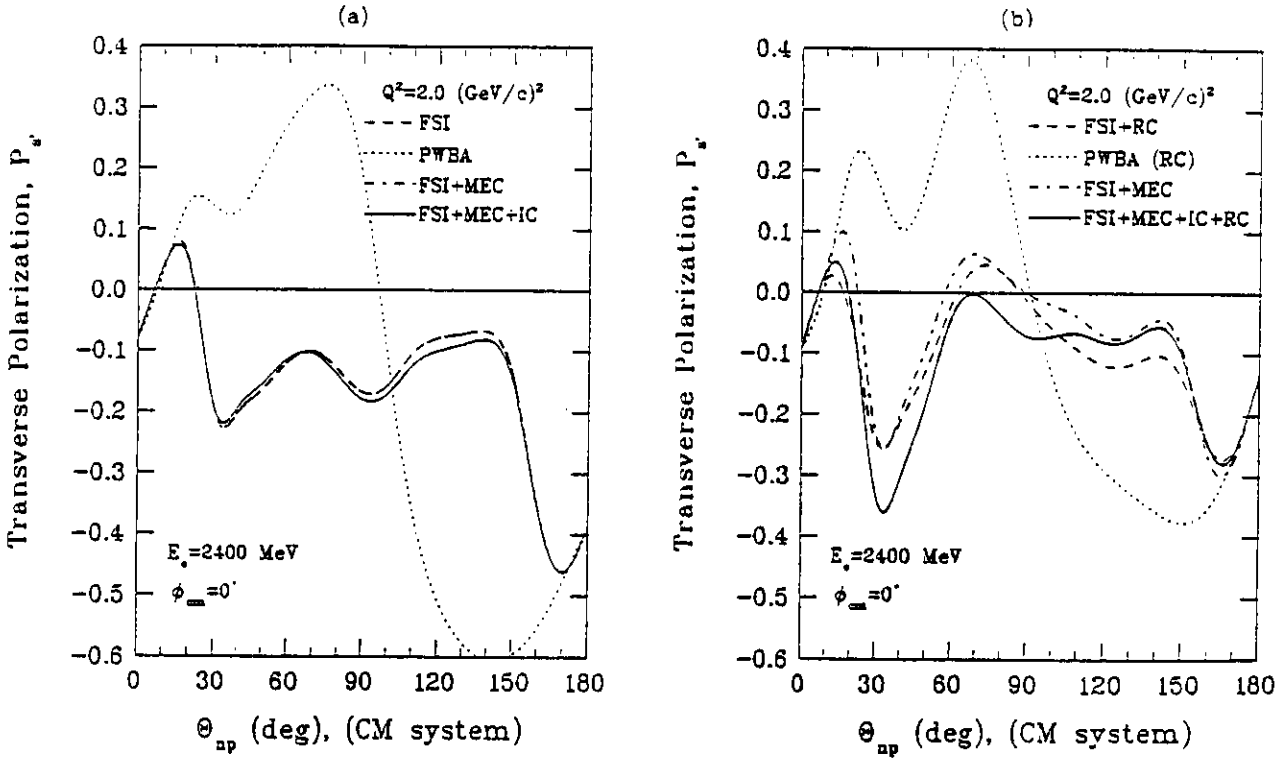

Fig. A7 Transverse Polarization $P_{S'}$ of the Neutron from $d(\vec{e}, e'\vec{n})p$ Reaction as a Function of $\Theta_{np}^{c.m.}$ for Q^2 = 2.0 (GeV/c)^2 with E = 2.4 GeV: (a) Result for Gari-Krümpelmann Parameterization of G_E^n, and (b) Result for Galster Parameterization of G_E^n.

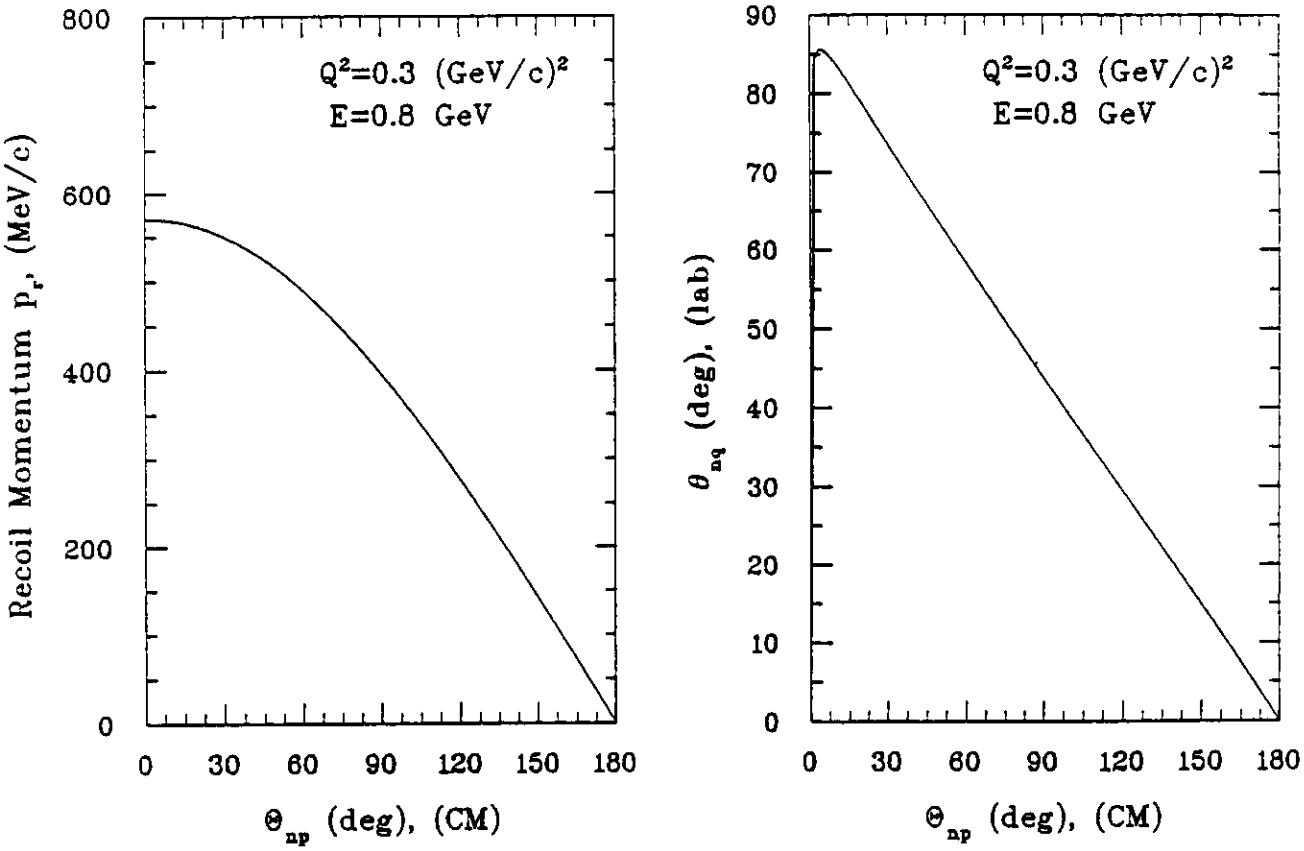

Fig. A8 The Recoil Momentum, p_r, and the Neutron Scattering Angle with Respect to $\vec{q}$, θ_{nq}^{lab}, as a Function of the Center-of-Mass Angle $\Theta_{np}^{c.m.}$ for $Q^2 = 0.3$ (GeV/c)^2 with $E = 0.8$ GeV.

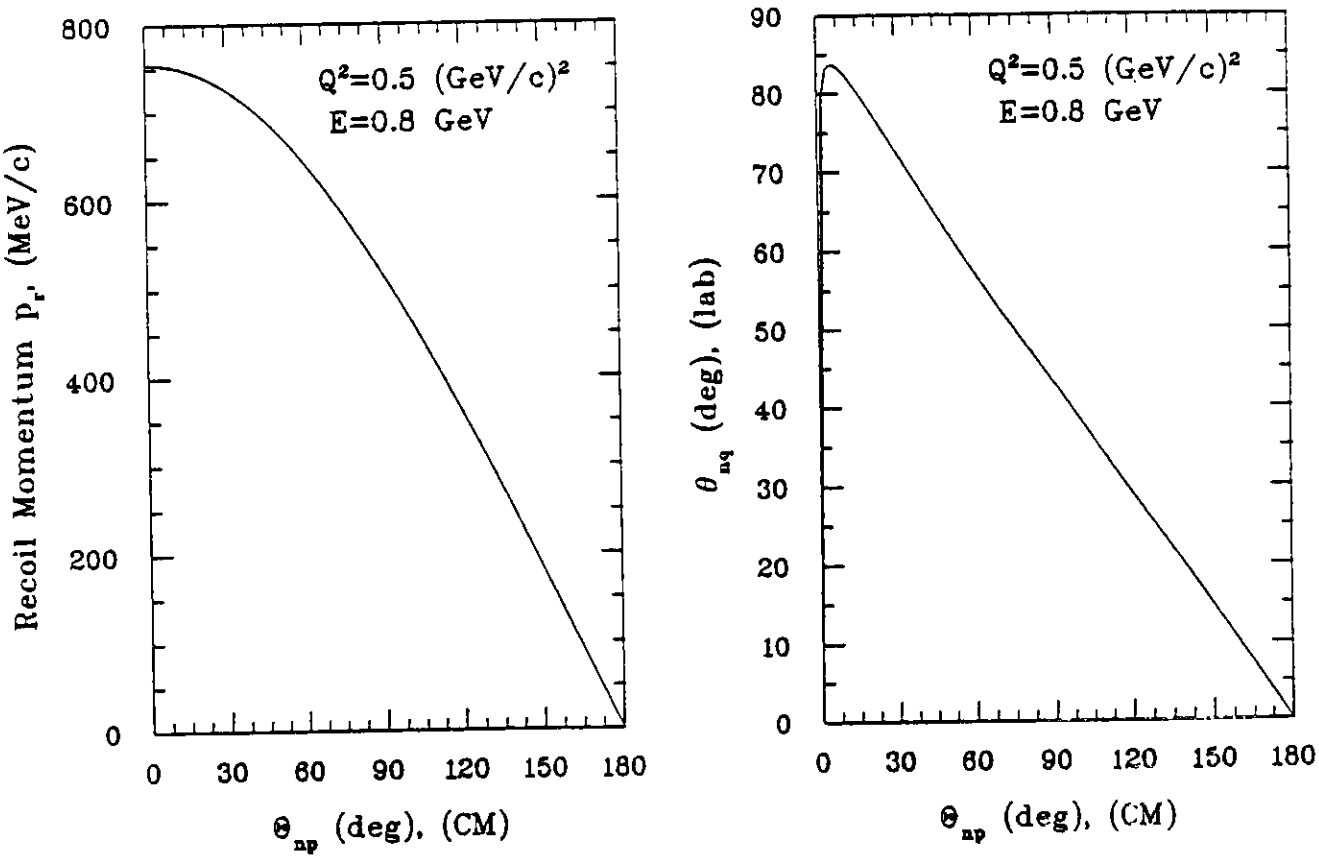

Fig. A9 The Recoil Momentum, p_r, and the Neutron Scattering Angle with Respect to $\vec{q}$, θ_{nq}^{lab}, as a Function of the Center-of-Mass Angle $\Theta_{np}^{c.m.}$ for $Q^2 = 0.5$ $(\mathrm{GeV/c})^2$ with $E = 0.8$ GeV.

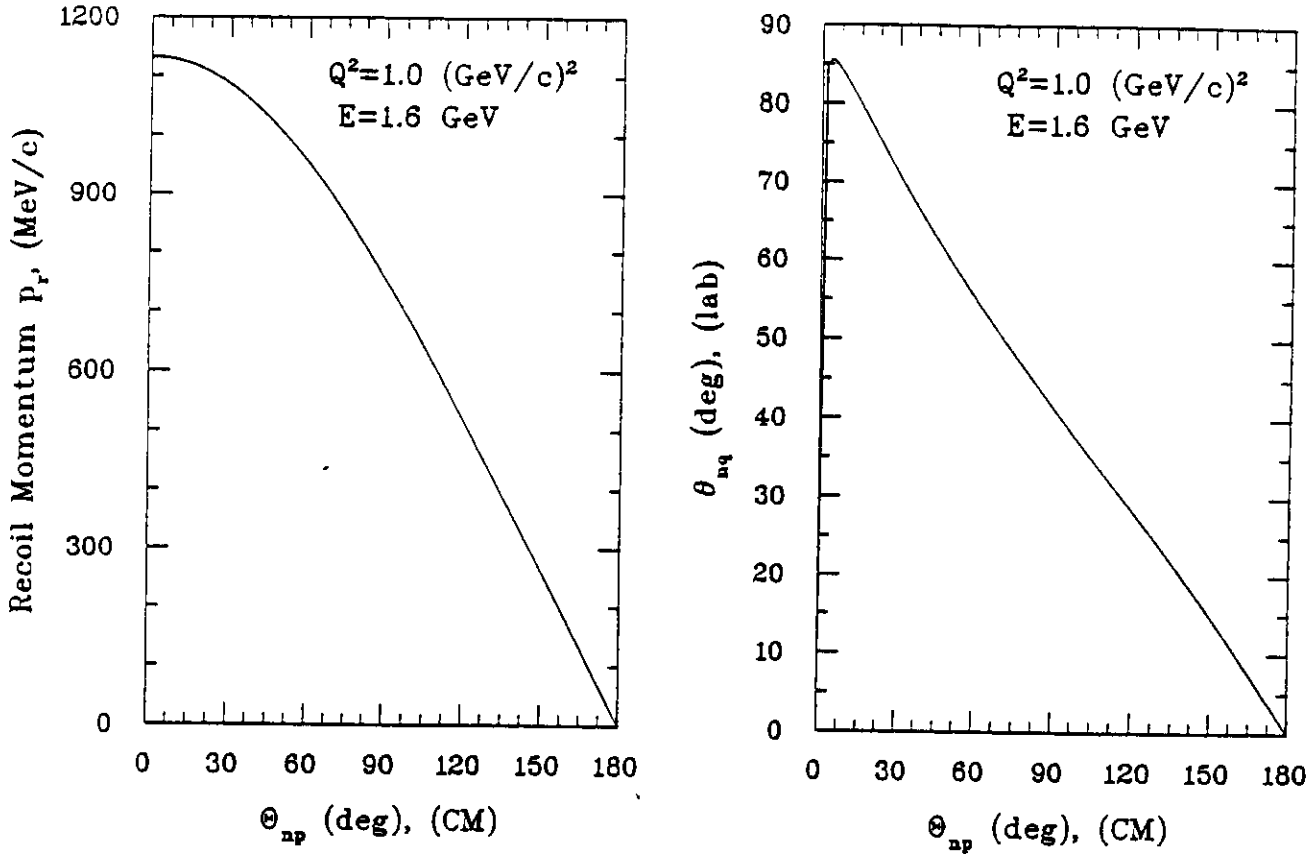

Fig. A10 The Recoil Momentum, p_r, and the Neutron Scattering Angle with Respect to $\vec{q}$, θ_{nq}^{lab}, as a Function of the Center-of-Mass Angle $\Theta_{np}^{c.m.}$ for $Q^2 = 1.0$ (GeV/c)^2 with $E = 1.6$ GeV.

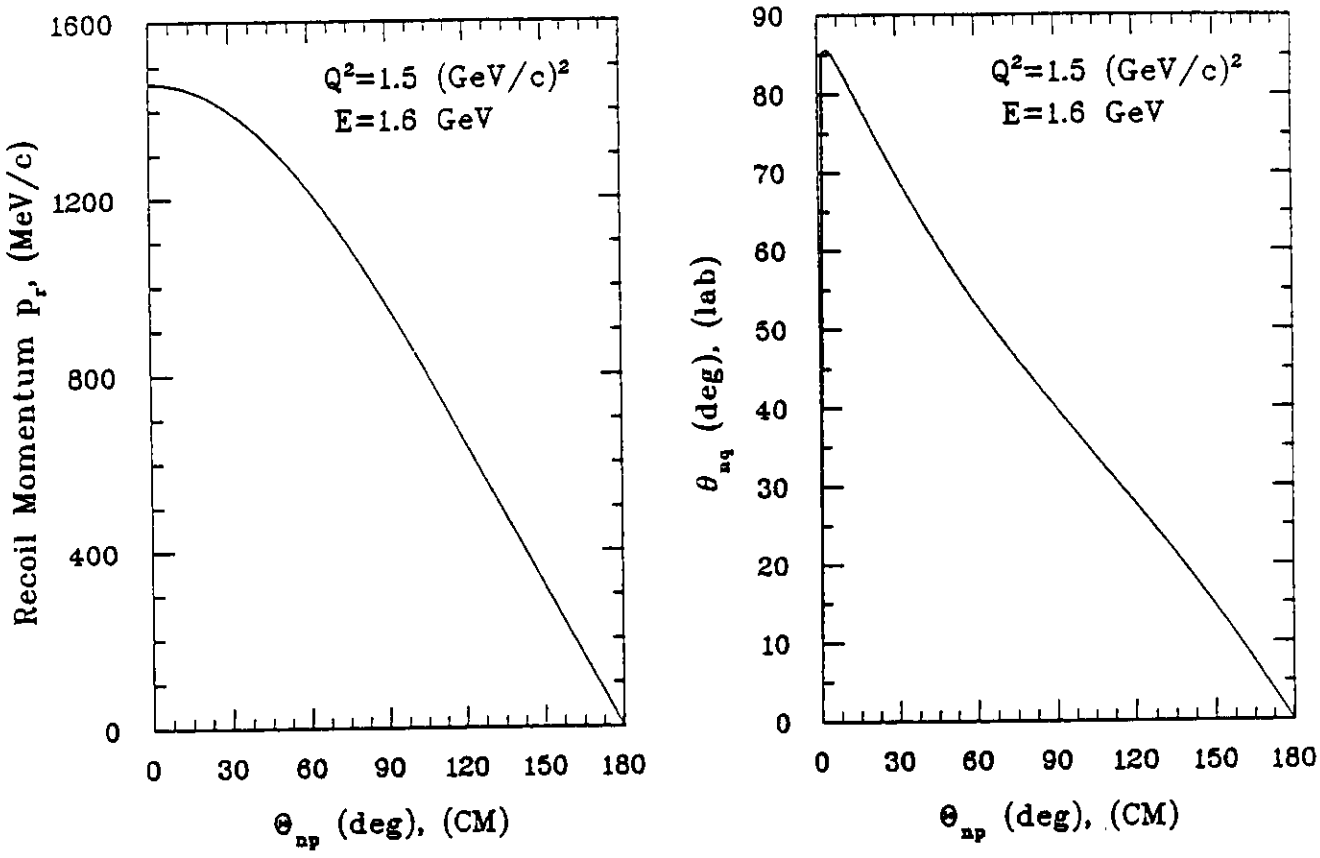

Fig. A11 The Recoil Momentum, p_r, and the Neutron Scattering Angle with Respect to $\vec{q}$, θ_{nq}^{lab}, as a Function of the Center-of-Mass Angle $\Theta_{np}^{c.m.}$ for $Q^2 = 1.5$ (GeV/c)^2 with $E = 1.6$ GeV.

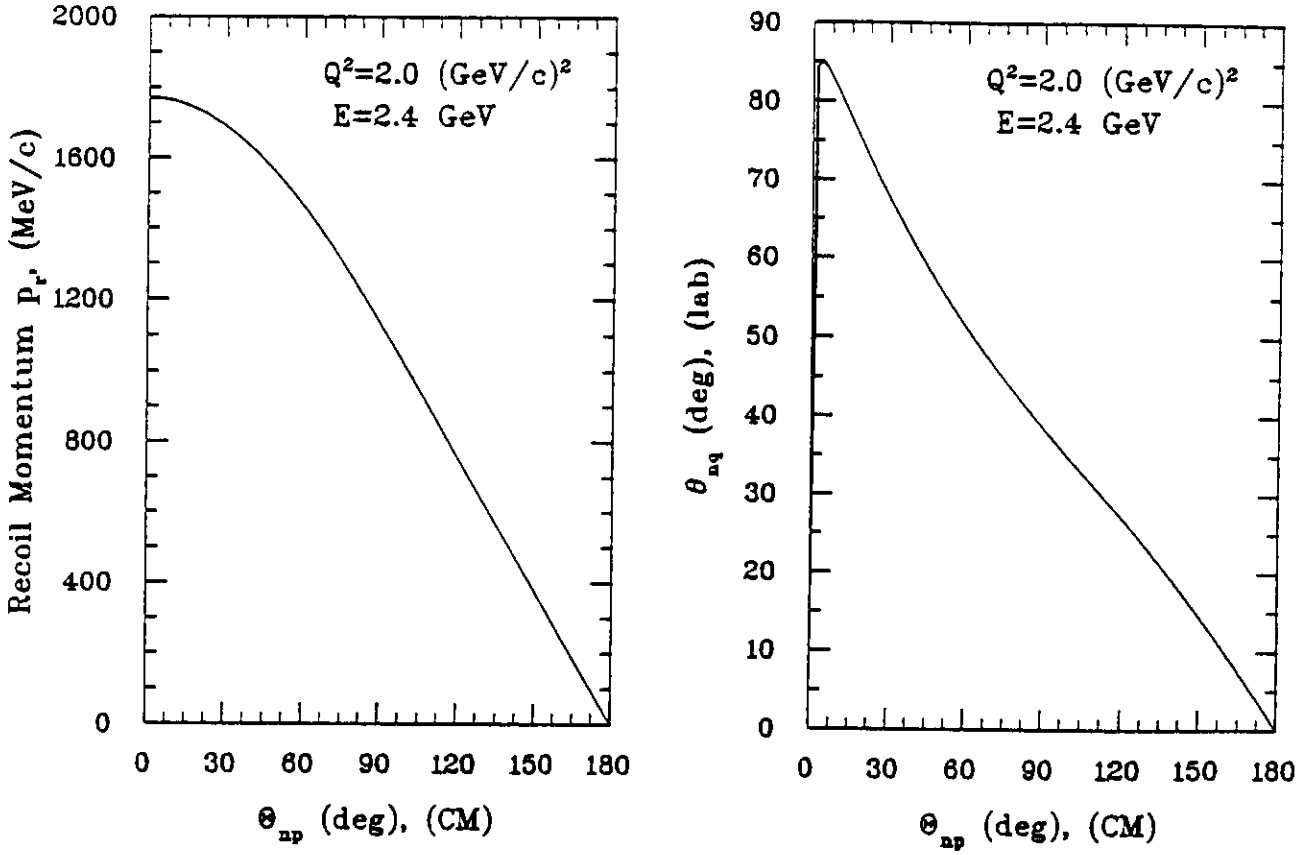

Fig. A12 The Recoil Momentum, p_r, and the Neutron Scattering Angle with Respect to $\vec{q}$, θ_{nq}^{lab}, as a Function of the Center-of-Mass Angle $\Theta_{np}^{c.m.}$ for $Q^2 = 2.0$ (GeV/c)^2 with $E = 2.4$ GeV.

APPENDIX B
CALIBRATION OF THE NEUTRON POLARIMETER

We measured the analyzing power and the efficiency of the neutron polarimeter that was used to measure the electric form factor of the neutron in Bates E85-05. The attached reprint is a report of these polarimeter calibration measurements with 138.4 MeV proton at the Indiana University Cyclotron Facility (IUCF). This report appeared in the IUCF Annual Report 1989-1990, pp. 73-78 (1990).

Performance of a Neutron Polarimeter to Measure the Electric Form Factor of the Neutron

T. Eden, R. Madey, W. M. Zhang, B. D. Anderson, A. R. Baldwin,
J. Schambach, E. Steinfelds and J. W. Watson
Center for Nuclear Research
Kent State University, Kent, Ohio 44242

S. Kowalski
Massachusetts Institute of Technology
Cambridge, Massachusetts 02139

J. J. Kelly
University of Maryland
College Park, Maryland 20742

J. M. Finn, P. Markowitz
College of William and Mary
Williamsburg, Virginia 23185

R. Lourie
University of Virginia
Charlottesville, Virginia 22904

P. J. Pella
Gettysburg College
Gettysburg, Pennsylvania 17325

J. Cameron, C. C. Foster, B. Ni, M. Spraker, E. J. Stephenson
Indiana University Cyclotron Facility
Bloomington, Indiana 47405

Abstract

We measured the analyzing power and the efficiency of a neutron polarimeter that was designed and constructed to measure the neutron electric form factor G_E^n. The measurement was carried out at the Indiana University Cyclotron Facility with the $^{14}C(\vec{p},\vec{n})^{14}N$ reaction at a proton beam energy of 138.4 MeV. The analyzing power, $\overline{A_y}$, averaged over the acceptances of the polarimeter is typically $0.44 \pm 0.02_0$ at a neutron energy of 135 MeV. With a lead–steel collimator, consisting of 4 inches of lead sandwiched between two $1\frac{3}{8}$ inch steel plates, ahead of the polarimeter, the average analyzing power is the same within statistics, namely, $\overline{A_y} = 0.43 \pm 0.02_1$. The quoted uncertainties are statistical. In each case, the efficiency of the polarimeter is about 0.26% for 135 MeV neutrons at a pulse–height threshold of 4 MeV equivalent electron energy (MeVee) on the front detectors and 10 MeVee on the rear detectors.

I. INTRODUCTION

In proposals to the Bates electron accelerator facility and to the Continuous Electron Beam Accelerator Facility (CEBAF), we proposed to determine the electric form factor G_E^n of the neutron by scattering longitudinally–polarized electrons quasielastically from deuterium and measuring the transverse polarization component $p_{s'}$ of the recoil neutron. In the impulse approximation, this transverse neutron polarization component $p_{s'}$, which lies in the scattering plane but normal to the neutron momentum, is directly proportional to G_E^n.[1] The electric form factor G_E^n of the neutron is a fundamental quantity needed for the understanding of both nucleon and nuclear structure. For the kinematic conditions of the experiment at Bates, the kinetic energy of the neutron is centered at 136 MeV. The kinetic energies of the neutrons in the CEBAF experiment range from 160 MeV to 1063 MeV.

The principle of the measurement of the neutron polarization component $p_{s'}$ is based on the fact that there is an asymmetry $\xi(\theta,\phi)$ in the scattering of polarized neutrons at an angle θ from unpolarized hydrogen nuclei. The asymmetry $\xi(\theta,\phi)$ is

$$\xi(\theta,\phi) = \vec{p}_{s'} \cdot \vec{A}_y(\theta) = p_{s'} A_y(\theta) \cos\phi \ , \tag{1}$$

where $\vec{A}_y(\theta)$ is the analyzing power of n–p scattering at the polar angle θ (the angle between the z–axis and the momentum vector of the scattered neutron), and the azimuthal angle ϕ (the angle between the vertical y–z plane of the polarimeter and the secondary scattering plane). The asymmetry averaged over the angular acceptances of the polarimeter is

$$\overline{\xi} = \langle p_{s'} A_y(\theta) \cos\phi \rangle = \overline{p_{s'}}\,\overline{A_y} \ . \tag{2}$$

Here

$$\langle p_{s'} A_y(\theta) \cos\phi \rangle \equiv \frac{\int p_{s'}(\theta,\phi)\, A_y(\theta) \cos\phi\, \sigma_{np}(\theta) \sin\theta\, d\theta\, d\phi}{\int \sigma_{np}(\theta) \sin\theta\, d\theta\, d\phi} \tag{3}$$

$$\equiv \frac{\overline{p_{s'}} \int A_y(\theta) \cos\phi \, \sigma_{np}(\theta) \sin\theta \, d\theta \, d\phi}{\int \sigma_{np}(\theta) \sin\theta \, d\theta \, d\phi} \tag{4}$$

$$\equiv \overline{p_{s'}}\,\overline{A_y} \ , \tag{5}$$

where the average neutron polarization is

$$\overline{p_{s'}} \equiv \frac{\int p_{s'}(\theta,\phi) \, A_y(\theta) \cos\phi \, \sigma_{np}(\theta) \sin\theta \, d\theta \, d\phi}{\int A_y(\theta) \cos\phi \, \sigma_{np}(\theta) \sin\theta \, d\theta \, d\phi} \ , \tag{6}$$

and the analyzing power averaged over the θ and ϕ acceptances of the polarimeter is

$$\overline{A_y} \equiv \langle A_y(\theta) \cos\phi \rangle \equiv \frac{\int A_y(\theta) \cos\phi \, \sigma_{np}(\theta) \sin\theta \, d\theta \, d\phi}{\int \sigma_{np}(\theta) \sin\theta \, d\theta \, d\phi} \ , \tag{7}$$

Here $\sigma_{np}(\theta)$ is the differential cross section for n–p scattering. According to Eq. (2), the average neutron polarization $\overline{p_{s'}}$ can be measured with a polarimeter of known average analyzing power $\overline{A_y}$ by measuring the average scattering asymmetry $\overline{\xi}$.

II. THE NEUTRON POLARIMETER

A. Configuration and Design

Shown in Fig. 1 is the configuration of the polarimeter. It consists of 12 scintillation counters—four mineral oil (BC517L) primary scatterers (1 through 4) and two sets of four rear plastic (NE–102) analyzer detectors. The rear detectors are located at a polar angle θ with respect to the direction of the incident neutrons. Rear detectors 5 through 8 are at an azimuthal angle $\phi = 0°$; and rear detectors 9 through 12 are at an azimuthal angle $\phi = \pi$. The positive and negative directions of the angle θ refer here to the positive and negative y directions, respectively, in accordance with the Madison convention.[2] The mean flight path from the point midway between primary scatterers #2 and #3 to the midpoint of each rear detector array is 2.0 m. All 12 scintillation detectors are mounted with the long dimension normal to the plane of the paper. The rear scintillators are 1.02 m long; the front scintillators are 0.508 m long. In front of each set of four detectors is a thin ($\frac{3}{8}$ in) plastic scintillation counter to veto charged particles. The lucite plastic container for the front scintillators has a wall thickness of $\frac{3}{8}$ inch. On each end, a cell end cap is used to adapt a light pipe to the larger dimension of the scintillator housing. An expansion chamber is mounted on top of each primary detector to allow thermodynamic expansion(contraction) of the mineral oil into(out of) the chamber.

The design of the polarimeter is based on the properties of n–p scattering as a polarization analyzer. The principles of design were described previously.[3,4] The conventional figure of merit $A_y^2\sigma_{np}$, which determines the useful range of scattering

angles for the polarimeter at a particular energy, is calculated from nucleon–nucleon (N–N) phase shifts with the computer code SAID.[5] A Monte Carlo code by Pella[6] is then used to look at $\overline{A_y^2 \sigma_{np}}$. For neutron energies of 130 to 140 MeV,[4] the optimum laboratory scattering angle $\theta = 21°$.

B. Lead-Steel Collimator

Based on measurements of neutrons in test runs at Bates,[7] the neutron polarimeter must be contained in a shielding enclosure with a front wall of several radiation lengths of lead in order to attenuate the energy of high energy photons and the flux of charged particles from the target. To simulate the experimental conditions at Bates, a lead–steel collimator was constructed. The lead–steel collimator consisted of 4 inches of lead sandwiched between two layers of $1\frac{3}{8}$ inches of steel. This sandwiched wall was located ahead of the polarimeter just outside of the hut. The back face of the lead–steel wall was $14\frac{7}{16}$ inches away from the front face of the first primary scattering scintillator. Ahead of this lead–steel wall was connected a rectangular steel collimator with a cross–sectional opening that measured 20 in x 30 in and 48 in long. The steel that made up this rectangular collimator was $1\frac{3}{8}$ inches thick. On each of the four sides of the collimator were pallets of concrete block that were as long as the collimator (48 inches). The concrete block covered the front face of the detector station in order to simulate the shielding for the G_E^n experiment at Bates.

C. Calibration of the Average Analyzing Power

From Eq. (2), we see that the average analyzing power $\overline{A_y}$ of the polarimeter can be obtained by measuring the scattering asymmetry $\bar{\xi}$ for neutrons of a known polarization $p_{n'}$. To obtain a neutron flux of known polarization, we used the $0^+ \rightarrow 0^+$ transition to the isobaric analog state (IAS) in the $^{14}\mathrm{C}(\vec{p},\vec{n})^{14}\mathrm{N}$ (2.31 MeV) reaction at zero degrees. The Q–value is -0.63 MeV to the ground state and -2.94 MeV to the 2.31 MeV state. If the incident protons are polarized normal to the reaction plane, and if the interaction conserves angular momentum and parity, the general relationship[8,9] between the neutron polarization p_n and the proton polarization p_p is

$$p_n[1 + p_p A_y(\theta)] = P(\theta) + p_p D_{NN'} \,, \tag{8}$$

where $A_y(\theta)$ is the analyzing power of the reaction, $P(\theta)$ is the polarization function of the reaction, and $D_{NN'}$ is the polarization transfer coefficient. A $(\vec{p},\vec{n})$ reaction on a $J^\pi = 0^+$ target to a $J^\pi = 0^+$ state in the residual nucleus is a pure nonspin–flip transition. Because the proton transfers its spin to the neutron without flipping the spin, the polarization transfer coefficient $D_{NN'} \equiv 1$ for a $0^+ \rightarrow 0^+$ transition. At 0°,

the analyzing power $A_y(0°)$ and the polarization function $P(0°)$ vanish identically; hence, for a $0^+ \rightarrow 0^+$ transition at 0°, Eq. (8) simplifies to $p_n = p_p$. Of the many known $0^+ \rightarrow 0^+$ transitions, the $^{14}C(\vec{p},\vec{n})^{14}N$ (2.31 MeV) is desirable because the cross section at 0° is large and the 2.31 MeV state can be separated easily from neighboring states.

D. Efficiency

The efficiency ϵ of the neutron polarimeter is the probability that a neutron entering the polarimeter will produce an event that satisfies all thresholds and cuts. The determination of the double–scattering efficiency of the polarimeter makes use of the 0° cross–sections of Anderson *et al.*[10] for the $^{12}C(p,n)^{12}N$ ($g.s.$) (which has a Q– value of -18.1 MeV) and those of Taddeucci *et al.*[11] for the $^{14}C(p,n)^{14}N$ (3.95 MeV, 1^+) (which has a Q–value of -4.58 MeV) reaction. For the incident proton beam of 138.4 MeV, the energy of the neutrons is $\simeq$ 119.7 MeV for the $^{12}C(p,n)^{12}N$ ($g.s.$) reaction; and $\simeq$ 133.8 MeV for the $^{14}C(p,n)^{14}N$ (3.95 MeV, 1^+) reaction. As reported by Watson *et al.*,[3] the efficiency of a nine–detector polarimeter was found to be constant within a few percent for neutron energies from about 80 to 140 MeV.

III. EXPERIMENTAL PROCEDURE

The experiment was performed with polarized protons at the Indiana University Cyclotron Facility (IUCF). The detector station that housed the polarimeter was located outside of the beam swinger facility on the 0° line at a flight path of 65.33 m from the target to the midpoint of the four front analyzing detectors in the polarimeter. A polarimeter located in the beam line (BL–2) between the two cyclotrons is used to determine the beam polarization by scattering the protons from a ^{4}He target. Scattered protons are detected by a pair of detectors mounted symmetrically to the left and right of the beam. The difference in the left and right yields are compared with the known analyzing power of the $\vec{p}$–^{4}He elastic scattering reaction at a given energy. The beam polarization was measured periodically with data acquisition and analysis software supplied by the IUCF. During a beam polarization run, the extracted scattering yields were used to determine the beam polarization and its associated uncertainty. The proton beam polarization averaged over the duration of these measurements was $0.725 \pm 0.001 \pm 0.015$. The uncertainty of ± 0.001 is statistical only. Other errors in the system arise from the calibration of the BL–2 polarimeter, the quality of the background subtraction in the BL–2 polarimeter, and the transport of the proton beam through the cyclotron. The uncertainty in the analyzing power of the BL–2 polarimeter is typically 0.5%. Background subtraction

introduces an uncertainty at a level of 1 to 2%. The uncertainty in the proton beam polarization from these factors is estimated to be about ± 0.015, about an order of magnitude larger than the statistical uncertainty.

Because the inside dimensions of the detector stations at the IUCF are not large enough to accomodate vertical mounting of the rear detectors, the neutron polarimeter detectors were mounted horizontally, which is the same orientation required for measurements of G_E^n. The horizontal orientation of the neutron polarimeter requires a sideways polarized beam for calibration. A superconducting solenoid upstream of the target was used to provide sideways polarized protons at the target, which is located just upstream of the dump magnet in the beam swinger facility. Because the polarization of the neutrons is perpendicular to the magnetic field in the dump magnet, the neutron precesses as the neutron traverses the dump magnet. The precession $\Delta\theta_s$ of the neutron spin can be determined from the following expression:

$$\Delta\theta_s = \gamma \frac{g_n}{2} \Delta\theta_p \ . \tag{9}$$

Here g_n is the intrinsic spin g–factor for the neutron, γ is the Lorentz factor for the neutron, and $\Delta\theta_p$ is the proton bend angle in the dump magnet, which is 12.5°. Equation (9) is a reliable measure of $\Delta\theta_s$ provided that the following integrations are equal for the neutrons and the protons; that is,

$$\int B\, dl_p = \int B\, dl_n \ , \tag{10}$$

where dl_p and dl_n are the differential path lengths for the proton and the neutron, respectively, and B is the magnetic field strength that depends on the position of the particle as it traverses the magnet. Because of the relatively small bend angle $\Delta\theta_p$ and because the beam dump is at a relatively large distance of about 22 feet from the entrance to the dump magnet, the difference in these two integrals is expected to be small. With $|g_n/2| = -1.91$ and $\Delta\theta_p = 12.5°$, we find $\Delta\theta_s = 27.3°$ for $T_p = 140$ MeV ($\gamma = 1.14$) in the counterclockwise direction; however, because the protons follow a curved path and pass through more of the fringe field of the dump magnet than the neutrons, $\int B\, dl_n$ is slightly smaller than $\int B\, dl_p$. We estimate $\Delta\theta_s = 25° \pm 2°$; accordingly, the sideways component of the neutron polarization is reduced by about 10%:

$$p_n = p_p \cos(25° \pm 2°) = (0.906 \pm 0.015)\, p_p \ . \tag{11}$$

For $p_p = 0.725 \pm 0.015$, $p_n = 0.657 \pm 0.017$.

IV. DATA REDUCTION

A spectrum of the time–of–flight (TOF) of neutrons from the target to the front scatterer is shown in Fig. 2 for neutrons with a sideways polarization to the right. The overall energy resolution was determined from the full width at half maximum (fwhm) values for the 1^+ and the 0^+ peaks. The energy resolution, ΔT, obtained from this experiment was $\sim$ 0.50 MeV (fwhm). This value for ΔT was consistent with the value obtained from the intrinsic time dispersion measurements with cosmic–rays on the front mineral oil scatterers. A neutron energy spectrum at 0° from the $^{14}C(\vec{p},\vec{n})^{14}N$ reaction is shown in Fig. 3 for 138.4 MeV incident protons. This energy spectrum combines TOF spectra for both spin states of the neutron to all four front scatterers. These data were obtained with a target to polarimeter flight path of 65.33 m. The peak labelled ^{12}N is the ground state of the $^{12}C(p,n)^{12}N$ reaction from the ^{12}C content of the ^{14}C target. The peaks in these spectra lie on top of a background that consists of the cosmic rays that leak through the anticoincidence detectors, the so–called "wraparound" or overlap neutrons from earlier beam bursts, and continuum neutrons from processes such as quasifree neutron knockout.

A. Instrumental Calibrations

Calibration constants are required for the six parameters needed to describe each recorded event in order to extract physical information from a recorded event. Madey *et al.*[12] describe the technique to obtain the position calibration, the pulse–height calibration, and the intrinsic time dispersion for large–volume mean–timed organic–scintillator detectors for neutrons. Two types of calibrations are needed: one for the time–of–flight (TOF) between the target and one of the front scatterers and the other for the time–of–flight (ΔTOF) between a neutron scattering event from one of the front scatterers and one of the rear detectors. For each TOF spectrum, we determine two calibration parameters: (1) the time–per–channel and, (2) the channel number for $t = 0$. Calibration of the time–per–channel is accomplished with a precision time calibrator. The results are typically 24 ps/channel. By identifying a peak of known velocity in the TOF spectrum, the channel number for $t = 0$ is determined for the flight time over a known flight path.

B. Data-Sorting Procedure

The data–sorting follows the procedure of Watson et al.[3] For each event, six parameters are recorded on magnetic tape, along with "tag" information identifying the spin state of the beam and those detectors in the polarimeter that were involved in a particular event. The six parameters are

(1) the time–of–flight from the target to one of the scatterers,

(2) the time–of–flight between the scatterer and a rear detector,

(3) the pulse–height in the scatterer,

(4) the pulse–height in the rear detector,

(5) the position (along the X–axis) of the interaction in the scatterer,

(6) the position of the interaction in the rear detector.

The position signals (5) and (6) are the time differences between the signals obtained from the photomultiplier tubes at the left and right of each detector. Hardware thresholds were set to be ~ 0.5 MeVee for the front scatterers and ~ 2 MeVee for the rear detectors. Note that MeVee represents "MeV electron equivalent" energy.

Off–line, events are sorted with the following sets of "*cuts*":

(1) Events falling below software pulse–height thresholds (4 MeVee for the front scatterers and 10 MeVee for the rear detectors) are rejected.

(2) The velocity of the incoming neutron v_{inc} and its kinetic energy T_{inc} are calculated from the known flight path and parameter (1). Events with T_{inc} falling outside the desired range of energies (e.g., $110 \leq T_{inc}(\mathrm{MeV}) \leq 140$) are rejected.

(3) From tag information and position information (parameters 5 and 6), we construct the coordinates (x_1, y_1, z_1) for the point of interaction in the front scatterer and (x_2, y_2, z_2) for the point of interaction in the rear detector. From $\Delta x = (x_2 - x_1)$, $\Delta y = (y_2 - y_1)$, and $\Delta z = (z_2 - z_1)$, we determine r (the distance between an interaction in a front scatterer and an interaction in a rear detector), θ, and ϕ. The scattering angle θ is restricted by the physical layout of the polarimeter. Events falling outside a specified cut on ϕ will be rejected. The ϕ–cut imposed was $|\phi| \leq 40°$. (See Fig. 4)

(4) The velocity of the scattered neutron v_{sc} is determined from the calculated flight path r and the time–of–flight between the scatterer and a rear detector (*i.e.*, parameter (2)). This scattered velocity v_{sc} is compared with the velocity v_{np} calculated for n–p scattering. The kinetic energy of the scattered neutron T_{np} is given by:

$$T_{np} = \frac{2\,T_{inc}\cos^2\theta}{(\gamma+1)-(\gamma-1)\cos^2\theta}\,. \tag{12}$$

For low incident neutron energies (*i.e.*, 110–140 MeV) and for relatively small scattering angles, notice that the factor

$$\frac{2}{(\gamma+1)-(\gamma-1)\cos^2\theta} \approx 1\,; \tag{13}$$

Hence,

$$T_{np} \approx T_{inc}\cos^2\theta\,. \tag{14}$$

For calibrating the KSU polarimeter, Eq. (14) is a good approximation (within 1%) for the kinetic energy of the scattered neutron. After obtaining T_{np}, v_{np} is calculated relativistically. Events are rejected when v_{sc} is not sufficiently close to v_{np}. This velocity ratio v_{sc}/v_{np} has an important influence on η^*, the instrumental figure of merit, which will be discussed later. The cut on the velocity ratio R_v is needed to discriminate against background events from the $^{12}C(n,np)$ reaction on ^{12}C nuclei in the scatterers.

(5) Neutron excitation energy spectra (T_{inc} spectra) are generated for neutrons scattering to the top and bottom rear detectors in the polarimeter for both spin–right and spin–left states of the proton beam. These spectra are the output of the sorting program (see Fig. 5 & Fig. 6).

Listed in Table I is a compilation of the events accepted after each cut in an off–line analysis for runs without the collimator:

TABLE I. Fraction of events accepted after each cut.

Cut	Limits	Events	Acceptance (%)
Good events	Hardware threshold	2,424,516	100.0
Pulse–height	4 and 10 MeVee	1,080,632	44.6
Time of flight	$110 \leq T_n(\text{MeV}) \leq 140$	938,372	38.7
Azimuthal angle, ϕ	$\lvert\phi\rvert \leq 40°$	861,951	35.6
Velocity ratio	$R_v \leq 0.90$	322,461	13.3

The number of events extracted in the 0^+ peak after all of the above cuts have been imposed is only about 0.8% of the good events.

C. Peak-Fitting and Statistical Analysis

From the output of the data–sorting routine, namely Figs. 5 and 6, we obtain the up–down scattering asymmetry $\bar{\xi}$:

$$\bar{\xi} = \frac{N_U - N_D}{N_U + N_D} \ , \tag{15}$$

with

$$N_U \equiv N_U^R + N_U^L \ , \tag{16}$$

and

$$N_D \equiv N_D^R + N_D^L \ . \tag{17}$$

Here the superscript $R(L)$ denotes the case when the sideways polarization of the neutron flux is to the right(left). Four spectra result from the data–sorting procedure. These four excitation energy spectra are fitted with the minimization program MINUIT.[13] Briefly, we use this program to fit both the 0^+ and the 1^+ peaks with Gaussians and to fit a broad Lorenztian function to the background on both sides of the peaks. Input parameters consist of calculated (kinematic) values for the kinetic energy of both peaks and the width of the peaks at fwhm. Lastly, we look at the quantity χ^2 which determines the goodness of fit of the curve–fitting to the spectrum. A minimal χ^2 will yield the best fit possible for the given spectrum.

From Eq. (15), we can express the relative uncertainty in the average asymmetry as:

$$\left(\frac{\Delta\bar{\xi}}{\bar{\xi}}\right)^2 = \left[\frac{\Delta(N_U - N_D)}{N_U - N_D}\right]^2 + \left[\frac{\Delta(N_U + N_D)}{N_U + N_D}\right]^2 = \frac{N_U + N_D}{(N_U - N_D)^2}(1 + \bar{\xi}^2) \ , \qquad (18)$$

or

$$\frac{\Delta\bar{\xi}}{\bar{\xi}} \approx \frac{(N_U + N_D)^{1/2}}{N_U - N_D} = \frac{1}{\bar{\xi}N^{1/2}} \ . \qquad (19)$$

The first equality in Eq. (19) is a good approximation because $\bar{\xi}^2 \ll 1$; from Eq. (15), the second equality in Eq. (19) follows by substituting $N_U - N_D = \bar{\xi}(N_U + N_D) \equiv \bar{\xi}N$. From Eq. (2), the relative error in the average analyzing power of the polarimeter can be written:

$$\left(\frac{\Delta\overline{A_y}}{\overline{A_y}}\right)^2 = \left(\frac{\Delta\bar{\xi}}{\bar{\xi}}\right)^2 + \left(\frac{\Delta\overline{p_{s'}}}{\overline{p_{s'}}}\right)^2 \equiv \left(\frac{\Delta\overline{A_y}}{\overline{A_y}}\right)^2_{\text{stat}} + \left(\frac{\Delta\overline{A_y}}{\overline{A_y}}\right)^2_{\text{scale}} \ , \qquad (20)$$

where the relative scale uncertainty is

$$\left(\frac{\Delta\overline{A_y}}{\overline{A_y}}\right)_{\text{scale}} \equiv \frac{\Delta\overline{p_{s'}}}{\overline{p_{s'}}} \ , \qquad (21)$$

and the relative statistical uncertainty in the average analyzing power of the polarimeter is

$$\left(\frac{\Delta\overline{A_y}}{\overline{A_y}}\right)_{\text{stat}} \equiv \frac{\Delta\bar{\xi}}{\bar{\xi}} \ . \qquad (22)$$

In view of Eqs. (19) and (15), we rewrite Eq. (22):

$$(\Delta\overline{A_y})_{\text{stat}} = \frac{1}{\overline{p_{s'}}N^{1/2}} \ . \qquad (23)$$

Uncertainties in the exact locations of the γ–peaks in the ΔTOF spectra, the TAC calibrations for both parameters (1) and (2), and the pulse–height thresholds in the detectors all contribute to an overall systematic uncertainty for the measurement.

V. PERFORMANCE OF THE POLARIMETER

Neutron excitation energy spectra from the $^{14}C(\vec{p},\vec{n})^{14}N$ reaction are shown in Figs. 5 and 6. The fact that the 0^+ state at 2.31 MeV of excitation energy is separated clearly from the 1^+ state at 3.95 MeV of excitation energy allows the yield under the 0^+ calibration peak to be extracted with a small uncertainty. At $T_p = 138.4$ MeV, this good separation results from a flight path of 65.33 m.

The first objective for evaluating the performance of the polarimeter was the desire for a large "instrumental figure of merit", given by the relationship:

$$\eta^* = (\overline{A_y})^2 \epsilon \,, \tag{24}$$

The value of η^* depends on the R_v cut; accordingly, we examine η^* as a function of the R_v software cut. A second objective is the desire to make $\overline{A_y}$ as large as possible in order to minimize sensitivity to instrumental asymmetries in the polarimeter; therefore, maximizing η^* while keeping $\overline{A_y}$ as large as possible with as small of an uncertainty as possible was our overall goal.

In Fig. 7, we present a spectrum of the velocity ratio R_v for $T_n = 133.8$ MeV; these data are from the strong $^{14}N(3.95$ MeV) state excited in the $^{14}C(\vec{p},\vec{n})^{14}N$ reaction. The spectrum for the runs with and without a collimator are similar. The R_v spectrum has a distinct, nearly Gaussian, peak centered at $R_v = 1$ from n-p elastic scattering events and a continuum of events from reactions on carbon with a peak at $R_v = 0.87$. The results of five R_v cuts that were analyzed for the run without the collimator are shown in Table II:

TABLE II. Performance of the polarimeter as a function of the R_v cut.

R_v cut	% retained	$\overline{\xi} \pm \Delta\overline{\xi}$	$\overline{A_y} \pm \Delta\overline{A_y}$	ϵ (%)	η^* (%)
0.88	41.9	0.278 ± 0.009	$0.42 \pm 0.01_9$	0.27	0.048
0.89	40.5	0.285 ± 0.010	$0.43 \pm 0.01_9$	0.27	0.050
0.90	38.4	0.288 ± 0.010	$0.44 \pm 0.02_0$	0.26	0.050
0.91	36.8	0.290 ± 0.011	$0.44 \pm 0.02_0$	0.25	0.048
0.92	35.2	0.292 ± 0.011	$0.44 \pm 0.02_0$	0.24	0.046
0.93	33.9	0.299 ± 0.011	$0.45 \pm 0.02_1$	0.23	0.047
0.94	32.3	0.297 ± 0.012	$0.45 \pm 0.02_1$	0.22	0.045
0.95	31.1	0.301 ± 0.012	$0.46 \pm 0.02_1$	0.21	0.045

With a mean flight path of 2.0 m between the midpoint of the front scatterers and the midpoint of each rear detector array, the carbon events are separated clearly from the hydrogen peak. A cut on the velocity–ratio spectrum, $R_v = 0.90$, eliminates most of the events from ^{12}C. The value for η^* was 0.050 with $\epsilon = 0.26$. The R_v cut at 0.90 yields $\overline{A_y} = 0.44 \pm 0.02_0$. Because the time–of–flight resolution of the 12–detector polarimeter with a 2.0 m flight path is better than that of a nine–detector

polarimeter[3] with a 1.0 m mean flight path, a cut at a specified velocity ratio (*e.g.*, $R_v = 0.90$) will eliminate a larger fraction of events from ^{12}C.

VI. DEPOLARIZATION OF NEUTRONS BY THE LEAD-STEEL WALL

Nuclear elastic scattering within the (lead–steel) shielding wall ahead of the polarimeter can depolarize the neutron flux before it reaches the polarimeter. The proton densities in lead and iron were taken from electron scattering data; and the neutron density is taken to be proportional to the proton density. We assume that all elastically–scattered neutrons reach the front scatterers. (Note that more than 90% of elastic scattering falls within a cone of opening angle $\Delta\theta < 12°$). Also we assume that inelastic scatterings are cut by off–line software analysis so that the beam intensity is attenuated as

$$I(x) = I_o e^{-x/\lambda} . \tag{25}$$

Here λ is the absorption mean free path; *i.e.*, $\lambda = 1/\rho_n \sigma_{abs}$, where σ_{abs} is the absorption cross section. Furthermore, we assume that the fraction of the transmitted beam that has suffered one or more elastic scatterings is

$$f_{el} = \sigma_{el} \frac{N_{av} t \rho}{A} , \tag{26}$$

where t is the thickness of the wall and σ_{el} is the total elastic cross section. Finally, if the elastically–scattered neutrons have a polarization $\overline{p_{el}}$ averaged over the given solid angle, the transmitted flux has a net polarization

$$\frac{p}{p_b} = 1 - f_{el}\,(1 - \overline{p_{el}}) = (1 - f_{el}) + f_{el}\,\overline{p_{el}} , \tag{27}$$

where p_b is the beam polarization. Hence, the problem reduces to a determination of $\overline{p_{el}}$.

We define a laboratory coordinate system $(\hat{x},\hat{y},\hat{z}) = (\hat{H},\hat{V},\hat{L})$, where $\hat{H}$ is horizontal, $\hat{V}$ is vertically upwards, and $\hat{L}$ is along the incident beam. When the reaction plane within the wall is horizontal and the scattering is to the left, this system coincides with the conventional $(\hat{S},\hat{N},\hat{L})$ system; however, we must consider reaction planes rotated through an azimuthal angle ϕ. We seek to relate polarization transfer coefficients $(D_{HH}, D_{VV}, ...)$ to the standard coefficients $(D_{SS}, D_{NN}, ...)$; for this purpose we use the transformation

$$\begin{pmatrix} D_{HH}\, D_{HV} \\ D_{VH}\, D_{VV} \end{pmatrix} = \begin{pmatrix} \cos\phi & -\sin\phi \\ \sin\phi & \cos\phi \end{pmatrix} \begin{pmatrix} D_{SS} & 0 \\ 0 & D_{NN} \end{pmatrix} \begin{pmatrix} \cos\phi & \sin\phi \\ -\sin\phi & \cos\phi \end{pmatrix} , \tag{28}$$

where D_{NS}=D_{SN}=0. Thus, we find

$$D_{HH} = D_{SS}\cos^2\phi + D_{NN}\sin^2\phi\ ,$$

$$D_{VV} = D_{SS}\sin^2\phi + D_{NN}\cos^2\phi\ , \tag{29}$$

$$D_{HV} = (D_{SS} - D_{NN})\cos\phi\sin\phi = D_{VH}\ .$$

Finally, averaging over the azimuthal angle ϕ, we obtain

$$\frac{1}{2\pi}\int d\phi\, D_{HH} = \frac{1}{2\pi}\int d\phi\, D_{VV} = \frac{1}{2}(D_{NN} + D_{SS})\ , \tag{30}$$

$$\frac{1}{2\pi}\int d\phi\, D_{HV} = \frac{1}{2\pi}\int d\phi\, D_{VH} = 0\ , \tag{31}$$

These relationships conform with expected symmetries; in particular, orthogonal components are not coupled by azimuthal averaging and the two polarizations orthogonal to the beam direction remain equal, but may be changed by $D_{NN} + D_{SS}$. For elastic scattering, D_{NN}=1; thus,

$$< D_{HH}(\theta) >_{\phi} = \frac{1}{2}(1 + D_{SS}(\theta))\ . \tag{32}$$

The following are some results of elastic scattering calculations ^{208}Pb and ^{54}Fe using the Paris–Hamburg G–matrix, ρ_n, and ρ_p to generate optical potentials appropriate to T_n = 140 MeV. The average transfer coefficient was obtained by numerical integration over θ using

$$\overline{D}_{HH} = \frac{\frac{1}{2}\int(1 + D_{SS}(\theta))\,\sigma(\theta)\,d\Omega}{\int\sigma(\theta)\,d\Omega}\ . \tag{33}$$

The average polarization $\overline{p_{el}}$ in Eq. (19) is equal to $\overline{D}_{HH}$ because here the incident neutron polarization is unity. The assumption of single scattering and the assumption that the acceptance of the front scatterer is independent of the scattering angle and the interaction point in the lead–steel wall are justified by the fact that both the numerator and the denominator of Eq. (33) attain more than 90% of their final value inside of 12°. To achieve convergence of the depolarization in this model, the integration must be carried out to about 40°. Integration over 40° yields the results listed in Table III:

TABLE III. Depolarization of neutrons by the lead–steel wall

Parameters	^{208}Pb	^{54}Fe
σ_{el} (barns)	2.11	0.754
σ_{abs} (barns)	2.13	0.904
Absorption mfp, λ (cm)	14.4	12.6
Wall thickness, t (cm)	10.2	7.0
Transmission	0.492	0.574
Elastic scattering fraction, f_{el}	0.704	0.463
Average transfer coefficient, $\overline{D}_{HH}$	0.965	0.948
p/p_b	0.975	0.976

The product of the p/p_b values in the table gives a net $p/p_b = 0.952$, or a neutron depolarization of 4.8%.

The results from the test run with the lead–steel collimator confirm, within statistics, that the overall performance of the polarimeter is unchanged; hence, using lead and steel for the shielding in the front wall will not hinder the measurement of G_E^n. The result that $\overline{A_y} = 0.43 \pm 0.02_1$ at a R_v cut of 0.90 is the same, within statistics, as the average analyzing power obtained without the collimator. Also, the comparison of the neutron polarizations for the runs with and without the collimator also is consistent, within statistics, with the prediction that the depolarization is only about 5%. The efficiency is the same for both cases, as expected, because the efficiency as defined depends only on neutrons incident on the first detector of the polarimeter; of course, the *real* efficiency for neutrons from the $d(\vec{e}, e'\vec{n})$ reaction will be lowered by the transmission of neutrons through the the lead–steel wall.

VII. CONCLUSION

We obtained calibration data for a new neutron polarimeter designed and built for the G_E^n experiment at the Bates linear accelerator. Our results are consistent with expectations from design. The design of the polarimeter discriminates against background events from the ^{12}C(n, np) reaction. This discrimination yields a relative maximum of the instrumental figure of merit. Depolarization of the incoming neutron flux by the lead–steel collimator is negligible (or small) so the benefits of the shielding qualities from this lead–steel wall can be enjoyed without decreasing $\overline{A_y}$.

VIII. ACKNOWLEDGEMENTS

This research was supported by the National Science Foundation Grant PHY #88–02392. One of us (P.J.P.) acknowledges support from the Research Corporation.

[1]R. G. Arnold, C. E. Carlson, and F. Gross, Phys. Rev. **C23**, 363 (1981).

[2]The Madison Convention, in: Polarization Phenomena in Nuclear Reactions, eds. H. H. Barschall and W. Haeberli (University of Wisconsin Press, Madison, WI, USA, 1970)

[3]J. W. Watson *et al.*, Nucl. Instr. & Meth., **A272** 750 (1988).

[4]R. Madey *et al.*, IEEE Transactions on Nuclear Science **36**, No. 1, 231, (1989).

[5]R. A. Arndt and L. D. Roper, computer program SAID, unpublished.

[6]P. J. Pella, Monte Carlo computer program, unpublished.

[7]R. Madey, J. Schambach, B. D. Anderson, A. R. Baldwin, A. Bernstein, G. Dodson, M. Farkhondeh, R. Lourie, J. M. Finn, P. Ulmer, R. Whitney, and J. J. Kelly, pp 140–156 in 1987–1988 Annual Scientific and Technical Report, Bates Linear Accelerator Center.

[8]L. Wolfenstein, Ann. Rev. Nucl. Sci. **6**, 43 (1956).

[9]G. C. Olsen, Rep. Prog. Phys. **35**, 717 (1972).

[10]B. D. Anderson *et al.*, Phys. Rev. **C26**, 8 (1982).

[11]T. N. Taddeucci *et al.*, Nucl. Phys. **A469**, 125 (1987).

[12]R. Madey *et al.*, Nucl. Instr. & Meth., **A214** 401 (1983).

[13]F. James and M. Roos, Computer Physics Communication, **10** 343 (1975).

FIG. 1. The neutron polarimeter.

FIG. 2. Time–of–flight spectrum of neutrons with a sideways polarization to the right from the $^{14}C(\vec{p},\vec{n})^{14}N$ reaction at a proton beam energy of 138.4 MeV.

FIG. 3. Energy spectrum of neutrons with both spin states from the $^{14}C(\vec{p},\vec{n})^{14}N$ reaction at a proton beam energy of 138.4 MeV.

FIG. 4. Number of events vs. the azimuthal scattering angle, ϕ. Panel (a) is a spectrum after imposing pulse–height cuts only; and in panel (b) is the spectrum after imposing all cuts.

FIG. 5. Spectrum of scattered neutrons with sideways polarization of the incident neutrons to the right. In panel (a) the neutrons are scattered to the top detectors; and in panel (b) the neutrons are scattered to the bottom detectors.

FIG. 6. Spectrum of scattered neutrons with sideways polarization of the incident neutrons to the left. In panel (a) the neutrons are scattered to the bottom detectors; and in panel (b) the neutrons are scattered to the top detectors.

FIG. 7. Spectrum of the velocity ratio $R_v = v_{sc}/v_{np}$ for a neutron kinetic energy of 133.8 MeV. The dashed line at $R_v = 0.92$ represents a cut that removes most of the events from the inelastic $^{12}C(p,pn)$ reaction.

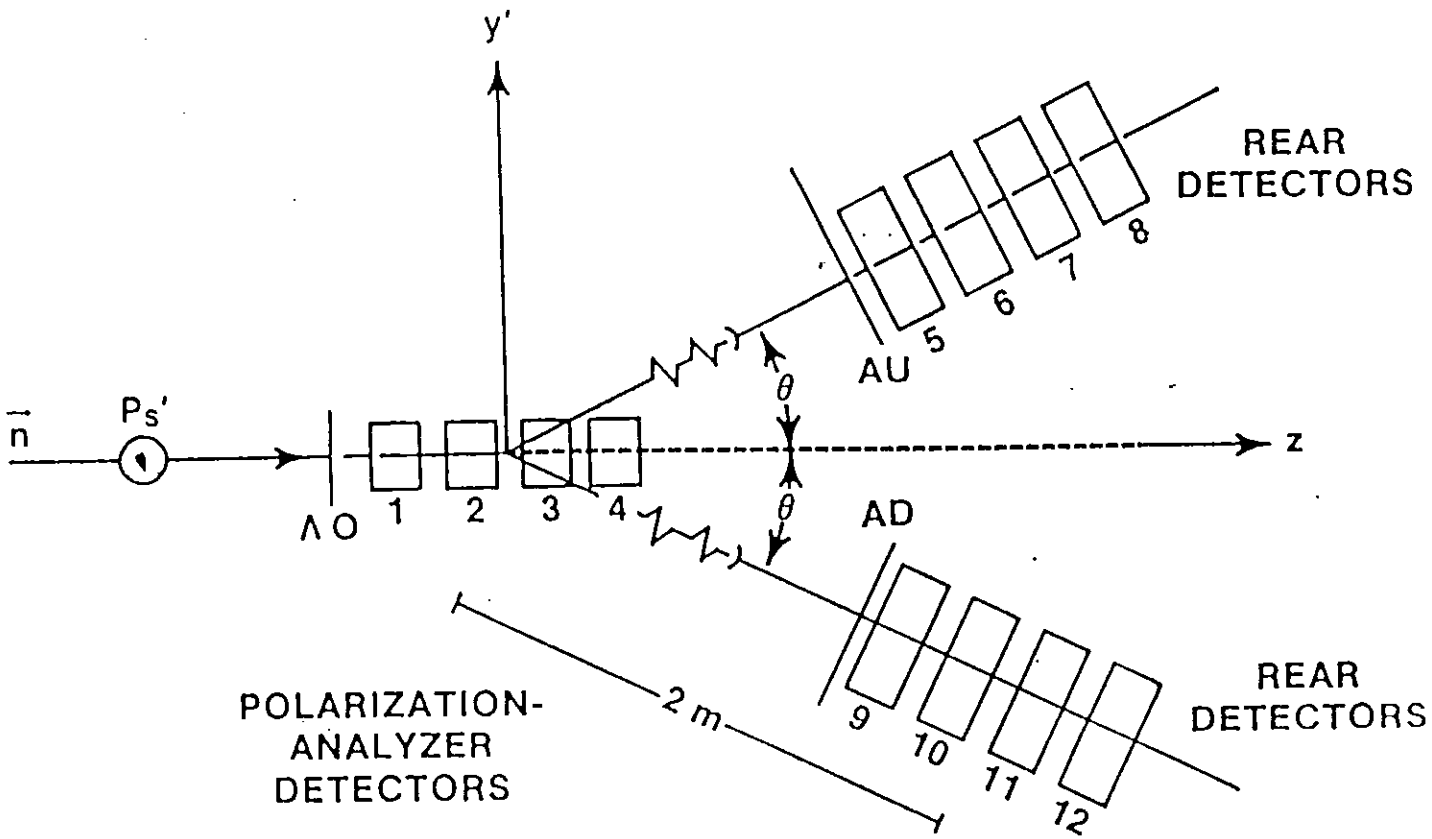
y'
REAR
DETECTORS
8
7
6
5
AU
θ
n
Ps'
z
ΛO
1
2
3
4
θ
AD
POLARIZATION-
ANALYZER
DETECTORS
2 m
9
10
11
12
REAR
DETECTORS

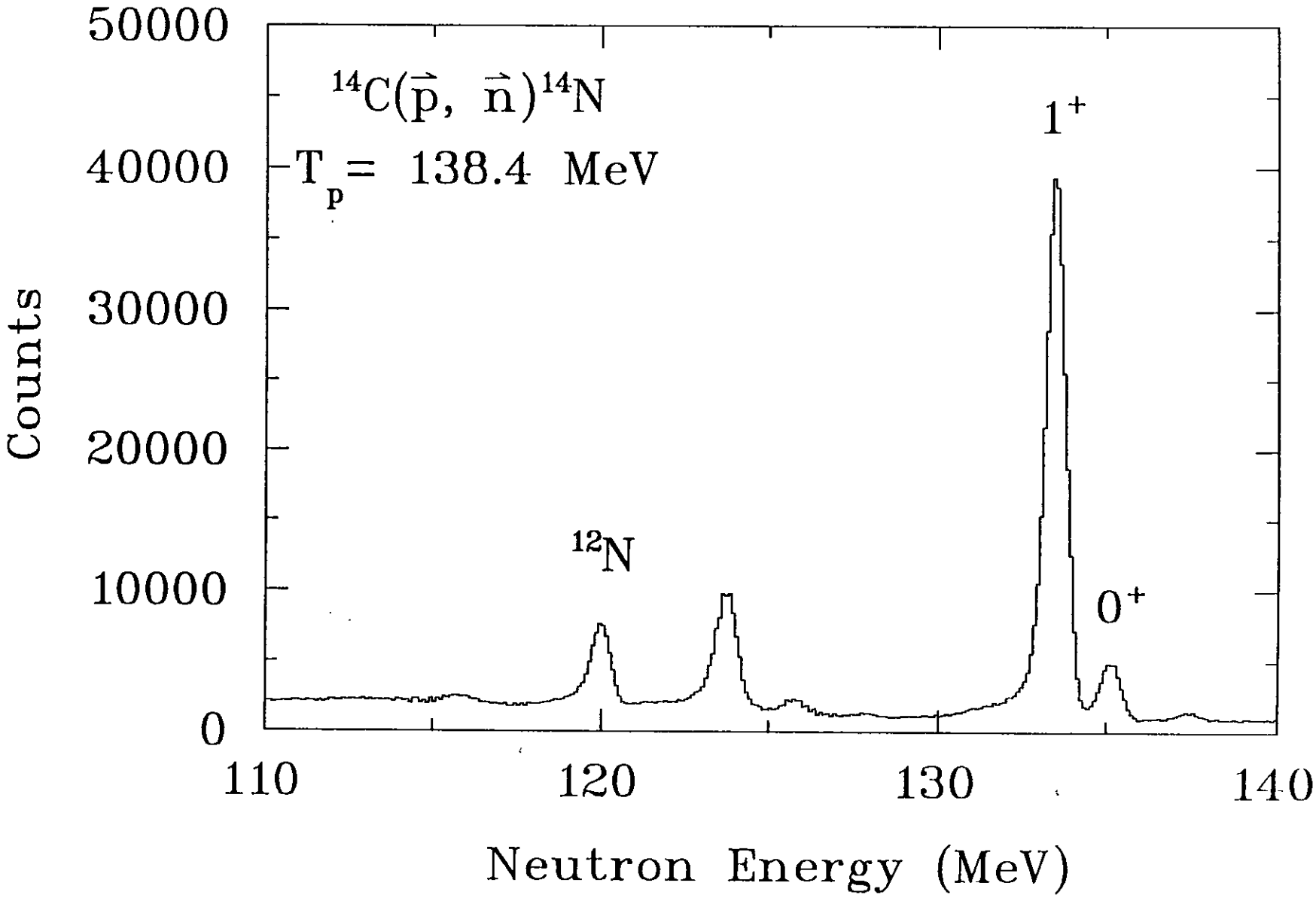
50000
40000
30000
20000
10000
0
Counts
$^{14}C(\vec{p}, \vec{n})^{14}N$
T_p = 138.4 MeV
1^+
^{12}N
0^+
110
120
130
140
Neutron Energy (MeV)

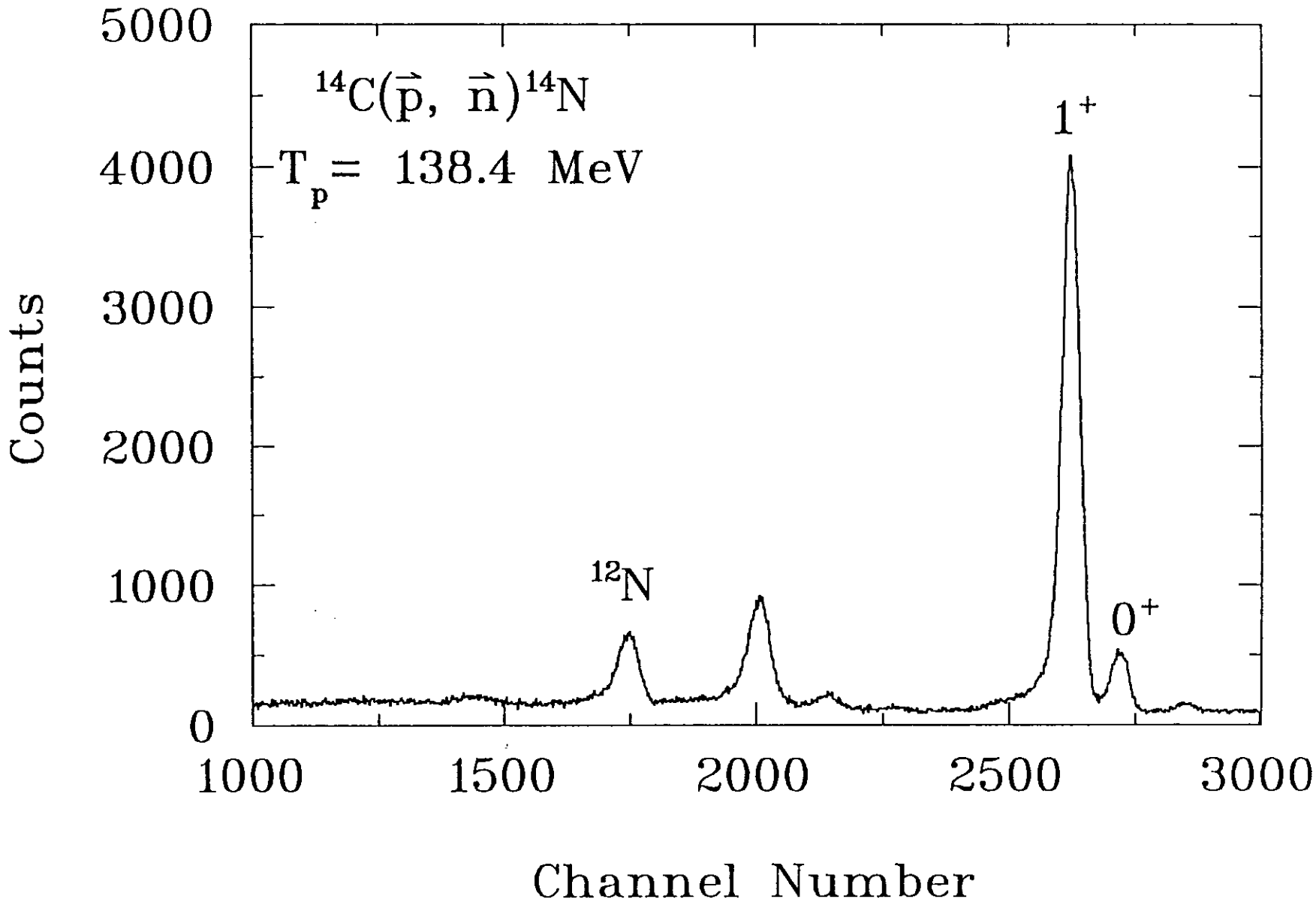
$^{14}C(\vec{p}, \vec{n})^{14}N$
$T_p = 138.4$ MeV
1^+
0^+
^{12}N
Counts
Channel Number
5000
4000
3000
2000
1000
0
1000
1500
2000
2500
3000

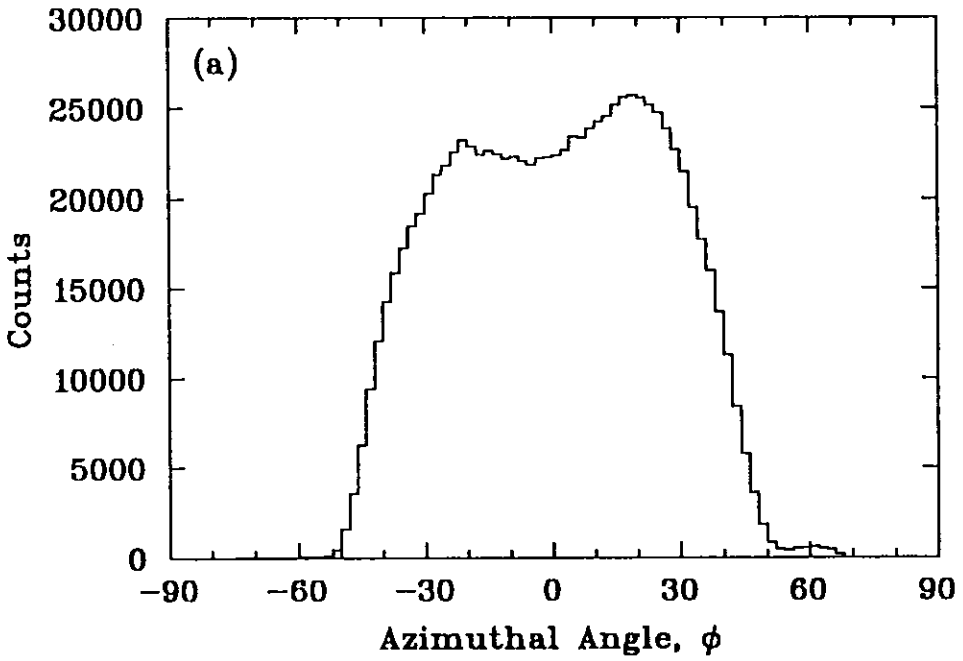
(a)
30000
25000
20000
15000
10000
5000
0
Counts
−90
−60
−30
0
30
60
90
Azimuthal Angle, ϕ

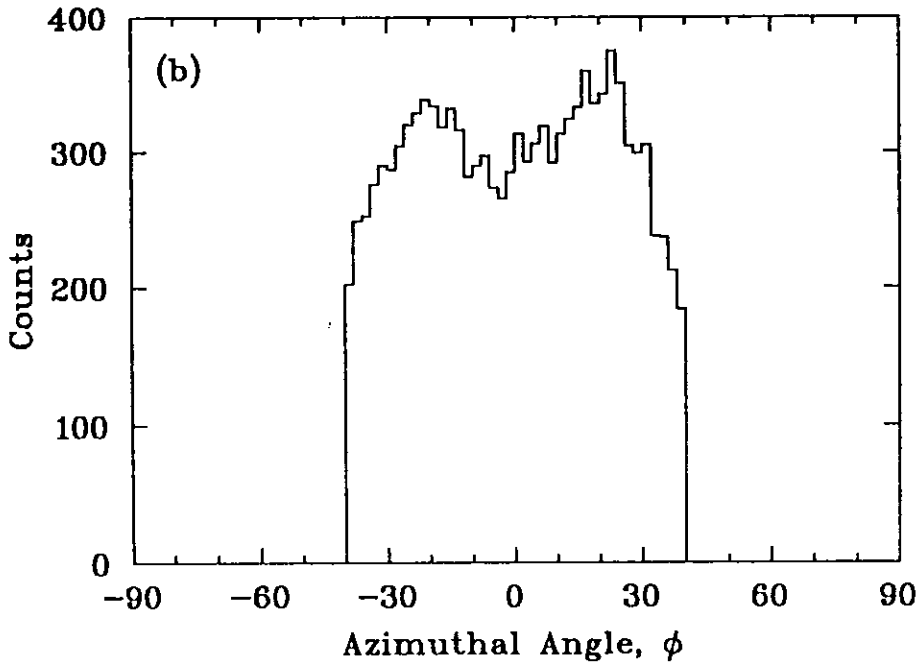
(b)
400
300
200
100
0
Counts
−90
−60
−30
0
30
60
90
Azimuthal Angle, ϕ

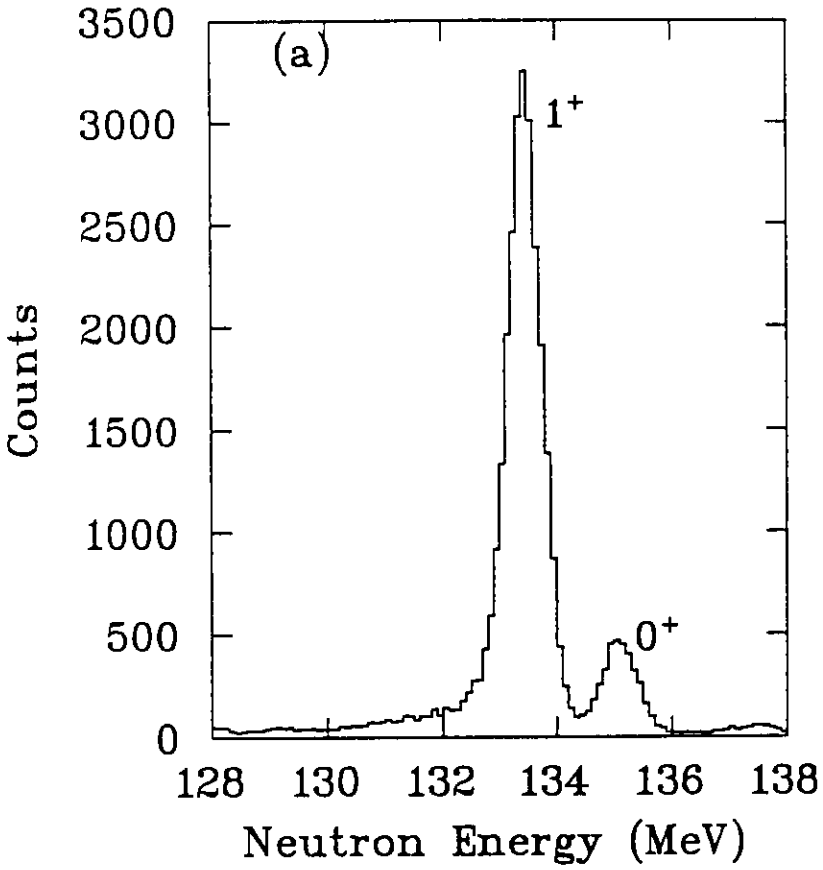
(a)
1+
0+
3500
3000
2500
2000
1500
1000
500
0
Counts
128
130
132
134
136
138
Neutron Energy (MeV)

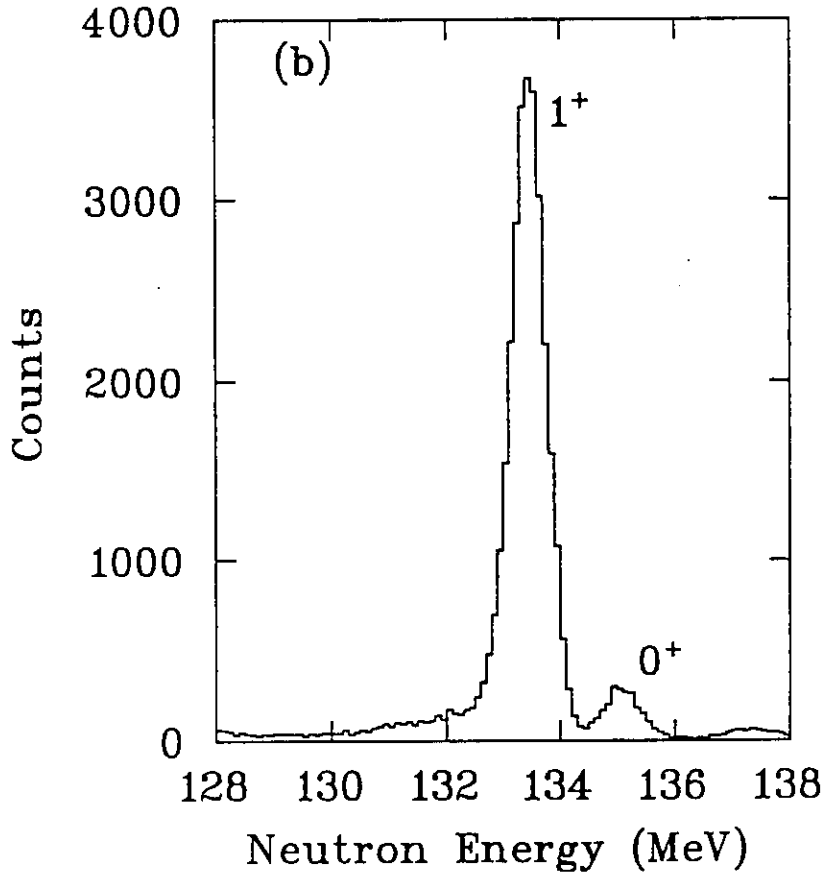
(b)
1+
0+
4000
3000
2000
1000
0
Counts
128
130
132
134
136
138
Neutron Energy (MeV)

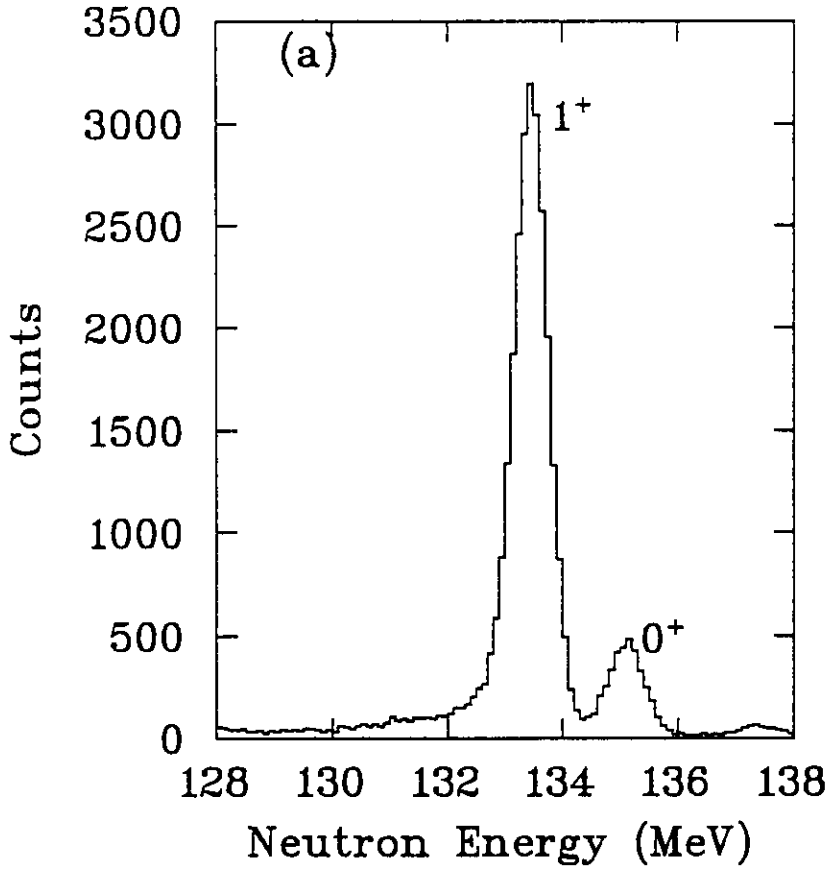
(a)
1+
0+
3500
3000
2500
2000
1500
1000
500
0
Counts
128
130
132
134
136
138
Neutron Energy (MeV)

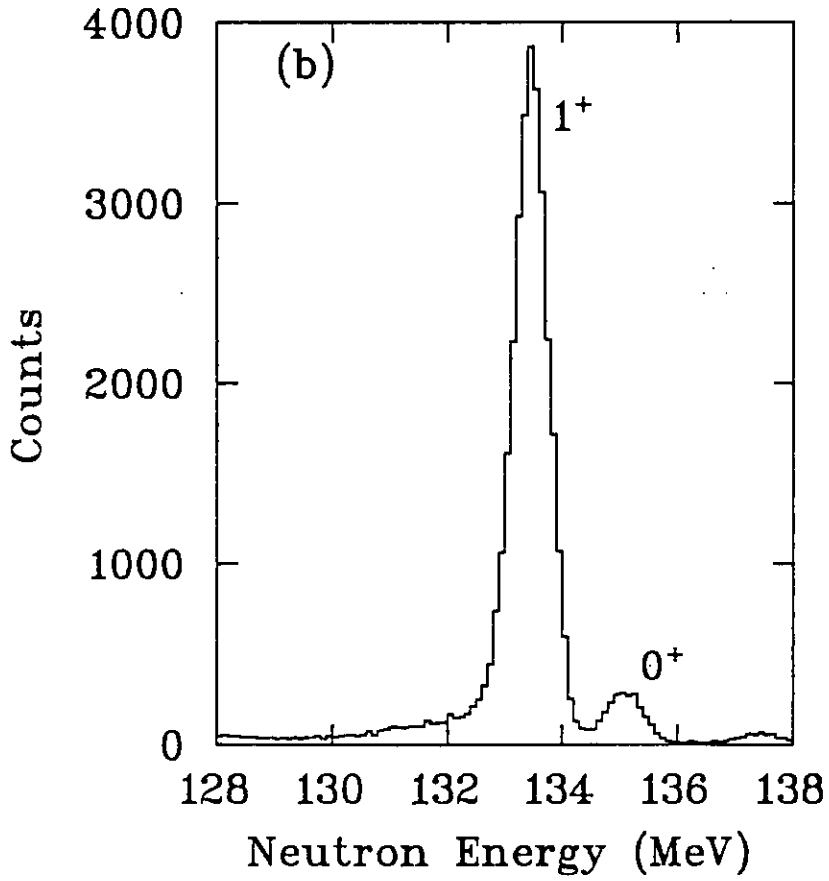
(b)
1+
0+
4000
3000
2000
1000
0
Counts
128
130
132
134
136
138
Neutron Energy (MeV)

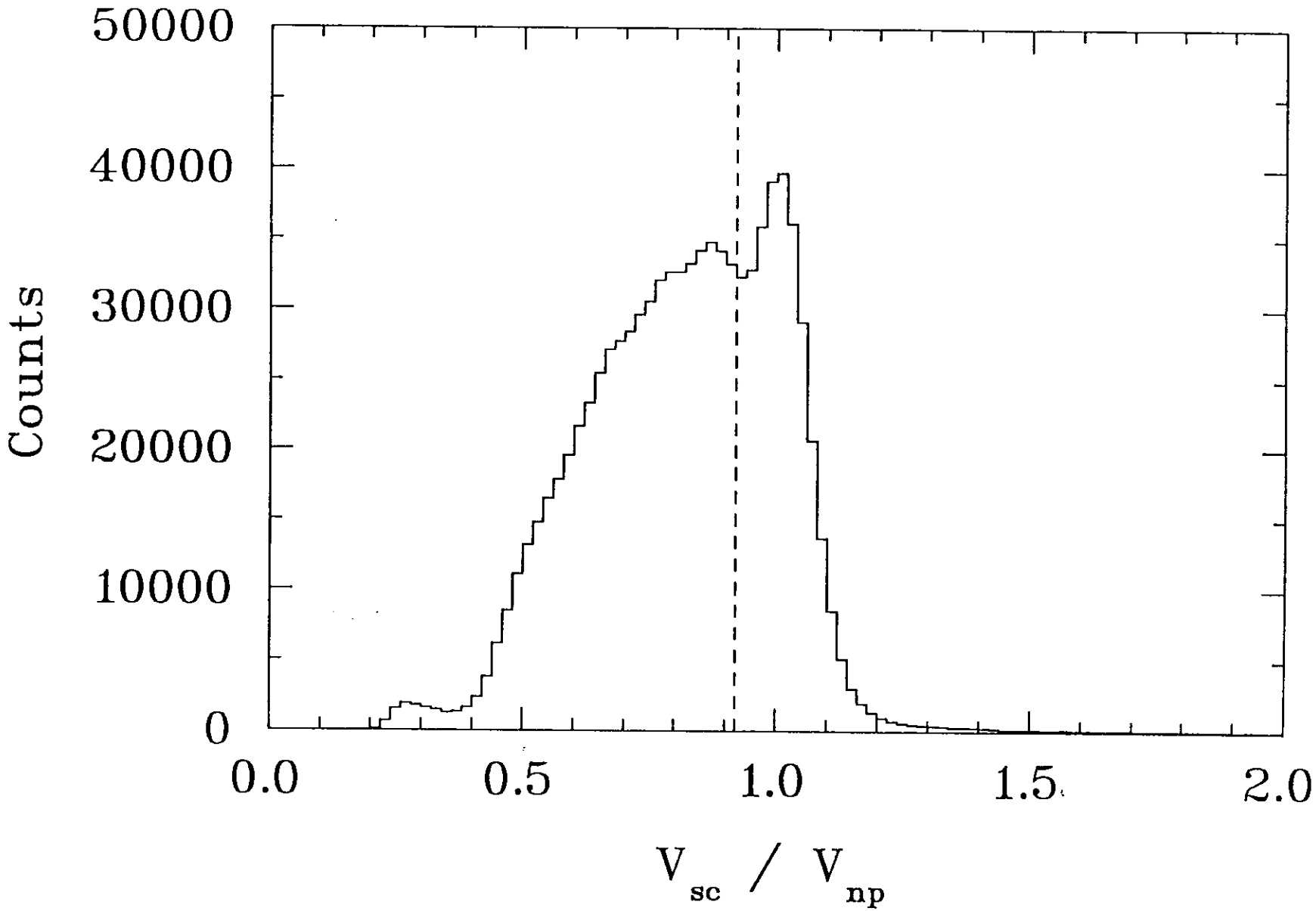
50000
40000
30000
20000
10000
0
Counts
0.0
0.5
1.0
1.5
2.0
V sc / V np